

A BAND STRUCTURE CALCULATION OF ELECTRON MOMENTUM DISTRIBUTIONS IN SOME TRANSITION METALS

**A Thesis Submitted
In partial Fulfilment of the Requirements
for the Degree of
DOCTOR OF PHILOSOPHY**

**By
DILIP GOVIND KANHERE**

to the

**DEPARTMENT OF PHYSICS
INDIAN INSTITUTE OF TECHNOLOGY KANPUR**

MAY, 1976

PHY-1976-D-KAN-BAN

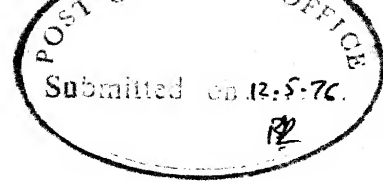
L.I.T. KANTUR
CENTRAL LIBRARY

51196
Acc. No. A

23 SEP 1977

This is for you -
who dance and pipe on pipes,
sell yourselves openly,
sin in secret,
and picture your future as academicians
with outsized rations
I ADMONISH YOU,
I - - - -

VLADIMIR MAYAKOVSKY



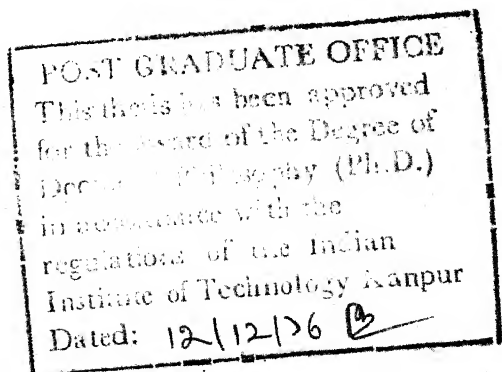
CERTIFICATE

This is to certify that the work presented in this thesis entitled "Band Structure Calculation of Electron Momentum Distributions in Some Transition Metals" by Dilip Govind Kanhere has been done under my supervision and it has not been submitted elsewhere for a degree.

R.M. Singru

R.M. Singru
Department of Physics
Indian Institute of Technology
Kanpur, India

May, 1976



ACKNOWLEDGEMENTS

This work, like any other scientific work, is an outcome of a collective effort. I express my deep sense of gratitude to all those who have contributed to it directly or indirectly.

I am highly indebted to Professor R.M. Singru for suggesting this problem and for his continued guidance and constant encouragement. I am thankful to him for the patience he has shown towards all my activities, academic or otherwise.

I am grateful to Dr. T.V. Ramakrishnan for many stimulating discussions and helpful suggestions. This association has helped me to gain clarity in many concepts especially in the band structure of transition metal.

I am also grateful to Dr. P.E. Mijnders for providing the Computer programmes without which this work would not have been possible. I have gained much knowledge from his close cooperation with our group throughout the period of this work.

I could complete the computational work at the Computer Centre at IIT Kanpur only because of the helpful Computer operators. I express my sincere thanks for their very friendly cooperation.

It was indeed a pleasure to work in 'Nuclear Lab', although my work was unconnected with it. My sincere thanks to all my colleagues in the lab. for their friendly association.

I cherish my friendship with all those who shared with me these long years. I have gained much from my interaction with them in all spheres of life.

I earnestly appreciate the patience and understanding of my parents during the period of this work.

It is a pleasure to thank Mr. J.K. Misra for an efficient and neat typing. I am thankful to him for his cooperation during the typing.

Thanks are due to Mr. Lalloo Singh Rathore for cyclostyling these pages.

Part of this work was supported by the Council of Scientific and Industrial Research, Government of India and the U.S. National Science Foundation, Washington, D.C., USA and I am thankful to these agencies for the support received.

Dilip Govind Kanhere

TABLE OF CONTENTS

<u>Chapter</u>		<u>Page</u>
	LIST OF TABLES	vii
	LIST OF FIGURES	viii
	SYNOPSIS	xi
1	INTRODUCTION	1
	1.1 Introduction	1
	1.2 The Compton Effect	3
	1.3 The Validity of the Impulse Approximation	8
	1.4 Experimental Determination of CP	9
	1.5 Positron Angular Correlation Studies	11
	1.6 Calculation of Momentum Density	14
	1.7 Comparison of CP and ACPAR Techniques	21
	1.8 Motivation Behind Our Present work	23
	References	
2	ELECTRON MOMENTUM DISTRIBUTION IN NICKEL AND COPPER EMPLOYING RENORMALIZED - FREE-ATOM MODEL	29
	2.1 Introduction	29
	2.2 RFA Model	30
	2.3 Compton Profiles	31
	2.4 Positron Wavefunctions	32
	2.5 Positron Angular Correlation	33
	2.6 Results and Discussion	34
	2.7 Conclusions	43
	References	

<u>Chapter</u>		<u>Page</u>
3	BAND STRUCTURE METHOD FOR CALCULATION OF MOMENTUM DENSITIES	46
	3.1 Introduction	46
	3.2 The Hubbard-Mijnarends Method	47
	3.3 Computational Details	53
	References	
4	ELECTRON MOMENTUM DENSITY IN Pd AND Ag	64
	4.1 Introduction	64
	4.2 Energy Bands and Fermi Surface of Pd and Ag	64
	4.3 Electron Momentum Distribution for Pd and Ag	72
	4.4 Comparison of EMD: Ni <u>vs</u> Pd and Cu <u>vs</u> Ag	99
	4.5 Limitations of Our Calculations	100
	References	
5	SYSTEMATICS OF THE ELECTRON MOMENTUM DENSITY IN TRANSITION METALS	103
	5.1 Introduction	103
	5.2 The Band Structure of 3d Metals	104
	5.3 Results for the EMD of 3d Metals and Discussion	106
	References	
6	DIRECTIONAL COMPTON PROFILES AND ANISOTROPIES OF Pd AND Ag	119
	6.1 Introduction	119
	6.2 Spherical Harmonic Expansion of EMD	121
	6.3 Application to Ni and Cu	123
	6.4 Results for Pd and Ag and Discussion	131
	References	
	VITAE	

LIST OF TABLES

<u>Table</u>		<u>Page</u>
1.1	Comparison between positron annihilation and Compton profile methods	22
2.1	Table of Fourier Components for nickel	39
2.2	Table of Fourier Components for copper	39
3.1	Effect of the number preferred vectors on the energy values of Pd	56
3.2	Effect of the number of preferred vectors on the momentum density $\rho(\vec{p})$ for Pd	57
3.3	Comparison of the calculated energy values for Pd with the results of Mueller et. al. and Wong	58
3.4	Effect of the number of preferred vectors on energy values and $\rho(\vec{p})$ of Ag	59
3.5	Some parameters used in the calculation	60
3.6	The preferred vectors used in the calculations	61
4.1	Comparison of some important bandwidths for Pd	66
4.2	Comparison of some important bandwidths for Ag	67
5.1	Some parameters and bandwidths for the 3d transition metals	105

LIST OF FIGURES

<u>Figures</u>		<u>Page</u>
1.1	Basic process of Compton scattering.	4
1.2	Schematic diagram of the Compton profile.	4
1.3	The momentum distributions for various cases.	17
	(a) Non-interacting electron gas.	
	(b) Interacting electron gas.	
	(c) First band Fermi surface	
	(d) No Fermi surface.	
	(e) Second band Fermi surface.	
	(f) One dimensional momentum distribution.	
1.4	Momentum density for atomic wavefunctions.	18
2.1	Calculated and experimental Compton profiles of polycrystalline nickel.	35
2.2	Calculated and experimental Compton profiles of polycrystalline copper.	36
2.3	Calculated and experimental band Compton profiles of polycrystalline nickel in the low momentum region.	37
2.4	Calculated and experimental ACPAR curves for nickel.	41
2.5	Calculated and experimental ACPAR curves for copper.	42
3.1	Flow diagram of the computational procedure.	54
4.1	Energy bands of Pd along some symmetry directions.	68
4.2	Energy bands of Ag along some symmetry directions.	69

<u>Figures</u>	<u>Page</u>
4.3 Sections of the Fermi surface of Pd by (100) and (110) planes.	70
4.4 Sections of the Fermi surface of Ag by (100) and (110) planes.	71
4.5 $\rho(\vec{p})$ and band structure along [100] direction for Pd.	73
4.6 $\rho(\vec{p})$ and band structure along [110] direction for Pd.	74
4.7 $\rho(\vec{p})$ and band structure along [111] direction for Pd.	75
4.8 $\rho(\vec{p})$ and band structure along [100] direction for Ag.	78
4.9 $\rho(\vec{p})$ and band structure along [110] direction for Ag.	79
4.10 $\rho(\vec{p})$ and band structure along [111] direction for Ag.	80
4.11 EMD isodensities for Pd: Total	82
4.12 EMD isodensities for Pd: Band 1	83
4.13 EMD isodensities for Pd: Band 2	84
4.14 EMD isodensities for Pd: Band 3	85
4.15 EMD isodensities for Pd: Band 4	86
4.16 EMD isodensities for Pd: Band 5	87
4.17 EMD isodensities for Pd: Band 6	88
4.18 EMD isodensities for Ag: Total	91
4.19 EMD isodensities for Ag: Band 1	92
4.20 EMD isodensities for Ag: Band 2	93
4.21 EMD isodensities for Ag: Band 3	94
4.22 EMD isodensities for Ag: Band 4	95

<u>Figures</u>		<u>Page</u>
4.23	EMD isodenses for Ag: Band 5	96
4.24	EMD isodenses for Ag: Band 6	97
5.1	Energy bands and $\rho(\vec{p})$ for V, Cr, Fe along [100] direction.	107
5.2	Energy bands and $\rho(\vec{p})$ for Ni and Cu along [100] direction. The vertical scale of energy in the case of Ni is different.	108
5.3	Energy bands and $\rho(\vec{p})$ for V, Cr, Fe along [110] direction.	111
5.4	Energy bands and $\rho(\vec{p})$ for Ni and Cu along [110] direction. The vertical scale of energy in the case of Ni is different.	112
5.5	Energy bands and $\rho(\vec{p})$ for V, Cr, Fe along [111] direction.	113
5.6	Energy bands and $\rho(\vec{p})$ for Ni and Cu along [111] direction. The vertical scale of energy in the case of Ni is different.	114
5.7	$\rho(\vec{p})$ for V along [110] direction for two locations of E_F as discussed in the text.	115
6.1	Theoretical and experimental CP anisotropies for Ni. Note the difference in momentum scale.	125
6.2	Theoretical and experimental ACPAR anisotropies for Ni. Note the difference in momentum scale.	126
6.3	Theoretical and experimental CP anisotropies for Cu. Note the difference in momentum scale.	127
6.4	Theoretical ACPAR anisotropies for Cu.	128
6.5	Experimental ACPAR anisotropies for Cu.	129
6.6	Theoretical CP anisotropies for Ag.	132

FiguresPage

6.7	Theoretical CP anisotropies for Ag.	133
6.8	Theoretical CP anisotropies for Pd.	134
6.9	Theoretical CP anisotropies for Pd.	135
6.10	Angular dependence of first seven Kubic harmonics.	139
6.11	ρ_z functions for Pd and Ag.	140
6.12	g_z functions for Pd and Ag.	141
6.13	a) Spherically averaged Compton profile, $g_0(p)$, for Pd and Ag.	142
	b) Spherically averaged EMD profile, $\rho_0(p)$, for Pd and Ag.	

SYNOPSIS

BAND STRUCTURE CALCULATION OF ELECTRON MOMENTUM
DISTRIBUTIONS IN SOME TRANSITION METALS

By
DILIP GOVIND KANHERE

Department of Physics
Indian Institute of Technology, Kanpur, India
May 1976

In recent years many detailed studies of the electron momentum distribution (EMD) in solids have been made by experimental techniques employing gamma-ray Compton scattering and positron angular correlation measurements. A proper comparison between theory and experiment is best made through single crystal profiles and their anisotropies. Simple theoretical models are not useful for calculating EMD in crystalline solids and, therefore, energy band calculations become necessary. Such studies are of particular interest for transition metals in view of their interesting electronic structure. The present thesis describes a band structure calculation of the EMD (for Compton scattering) in Pd and Ag employing Hubbard-Mijnarend's method. The emphasis in the present work is to examine the role played by band structure in determining EMD. A systematic study of the EMD in the 3d- and 4d- transition metals is also made. In the end a computational procedure to calculate directional anisotropies from theoretical EMD is developed.

In Chapter I the techniques of Compton profile (CP) and angular correlation of positron annihilation radiation (ACPAR) are introduced and an outline of relevant theory and experimental methodology is given. Various problems connected with the determination of EMD in metals are discussed. This is followed by the comparison of these two techniques.

A renormalized free atom (RFA) model for the calculation of CP and ACPAR is discussed in Chapter II. A calculation of CP and ACPAR for Ni and Cu is presented and the results are discussed. It is found that the RFA model gives a good overall description of the CP data for Ni and Cu and for Ni it supports an electronic configuration closer to $(3d)^9(4s)^1$. As far as the ACPAR data are concerned the RFA model does not give an equally satisfactory description. The need for a band structure calculation of EMD is emphasized.

Chapter III presents the formalism of Hubbard-Mijnarends band structure method of calculating EMD in transition metals. Necessary formulas and computational details are given and the limitations of this method are pointed out.

A calculation of the band structure and EMD (for Compton scattering) for Pd and Ag obtained by employing above method is presented in Chapter IV. The results for the energy bands are shown to be in satisfactory agreement with other reported calculations. Band-by-band contribution of the EMD is shown

along the three (Δ , Σ and Λ) symmetry directions and discussed in the light of respective band structure. In order to gain more insight, constant EMD contours (isodenses) in the (100) and (110) planes for total EMD as well as for separate bands are plotted. These contours are analyzed and compared, bringing out the role of d bands, Fermi surface etc. in the EMD. Results for the isoelectronic pairs Ni and Pd, and Cu and Ag are compared.

In Chapter V, a systematic study of EMD as one goes along the 3d- and 4d- transition series is made. The effects on EMD of the different properties of the d-band, e.g. bandwidth, s-d hybridization etc. are discussed. A comparative study of EMD in 3d- and 4d- transition series is also made.

In Chapter VI, a method of calculating single crystal CP (or ACPAR) profiles from theoretical EMD employing an expansion in terms of Kubic harmonics is developed. For Cu, the method is shown to give qualitative agreement with CP and ACPAR results. The anisotropies of Pd and Ag are predicted and discussed. Various aspects of this method and its limitations are discussed.

These studies have enabled the author to gain valuable insight into the band structure effects in the EMD of transition metals. It is hoped that these studies have contributed to our understanding of the role played by band structure in determining EMD, particularly in the transition metals.

Chapter 1

INTRODUCTION.

1.1 Introduction:

During the last few years the electron momentum distributions in atoms, molecules and solids have been a subject of considerable theoretical and experimental interest. The first direct experimental evidence for the dynamical nature of atomic electrons came in 1928 from the observed broadening of the inelastically scattered X-rays from atoms. DuMond [1] pointed out the importance of such experiments for studying the electron momentum distributions (EMD) and ascribed the broadening of the Compton-scattered radiation lineshape (the Doppler broadening) to the linear momentum of the electrons.

The next three decades saw no significant development of this experimental technique, the main reason being the non-availability of highly intense X-ray sources. It was in 1965 that Cooper, Leake and Weiss [2] demonstrated the feasibility of such experiments for studying EMD of metals like Li. Studies of other systems followed in the next few years. However, the most significant development occurred in 1971 when gamma-ray Compton scattering was introduced [3]. During the last few

years the growth of this technique has been rapid, and today it is emerging as a powerful tool for investigating EMD in a wide variety of materials [4-7]. The interesting history of these developments is outlined in a comprehensive review by Cooper[5].

During the period the technique of Compton profile lay dormant, another technique to study EMD was established and widely applied using a different microprobe, viz. positron [8-10]. The feasibility of measuring angular correlation of positron annihilation radiation (ACPAR) was demonstrated [11] in 1950's. In the last decade many accurate measurements on several substances employing ACPAR technique have been reported indicating the potential of this technique for investigating EMD in solids, in particular for studying the Fermi surface (FS) in metals [10].

In both these experiments the momentum of the electron, rather than its energy, plays a more fundamental role. The momentum of the electron is directly related to the ground state wavefunction of the system and therefore the knowledge and analysis of the EMD should give us interesting information about the ground state properties of the electrons, thus providing a test of the accuracy of the electronic wavefunctions. Particularly for metals one expects to obtain valuable information about the Fermi surface. One must, however, note that it is

not the EMD itself which is measured in the above experiments but a line or surface integral of the EMD in the momentum space. The positron and the photon interact with the electrons in different ways and therefore the Compton scattering and the positron annihilation techniques differ in terms of the experimental accuracy offered, theoretical understanding gained and to some extent the type of information obtained [9]. However, we believe that these techniques are complementary to each other and a greater understanding about the electronic states can be gained by studying a particular system employing both these techniques. We shall now discuss both these techniques in some detail, restricting our discussion mainly to those aspects which are directly related to EMD.

1.2 The Compton Profile:

1.2.1 The Basic Process:

The inelastic scattering of a photon by electrons is known as Compton scattering. It is well-known that for a stationary electron the shift ($\Delta\lambda$) in the wave length of a photon, Compton-scattered through an angle ϕ , (Fig.1.1) is given by,

$$\Delta\lambda = \frac{2h}{mc} \sin^2 \frac{\phi}{2} \quad (1.1)$$

However, the above relation is modified in the case of a free electron having a finite linear momentum. So that the

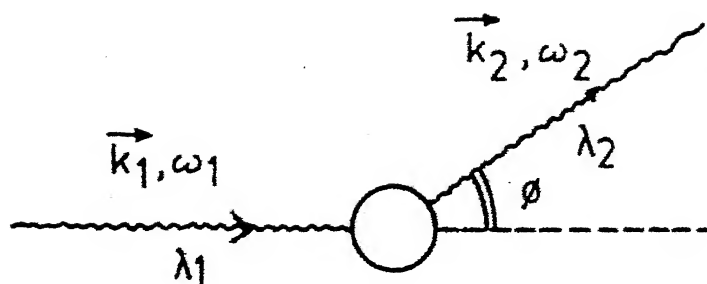


Fig. 1.1: Basic process of Compton scattering.

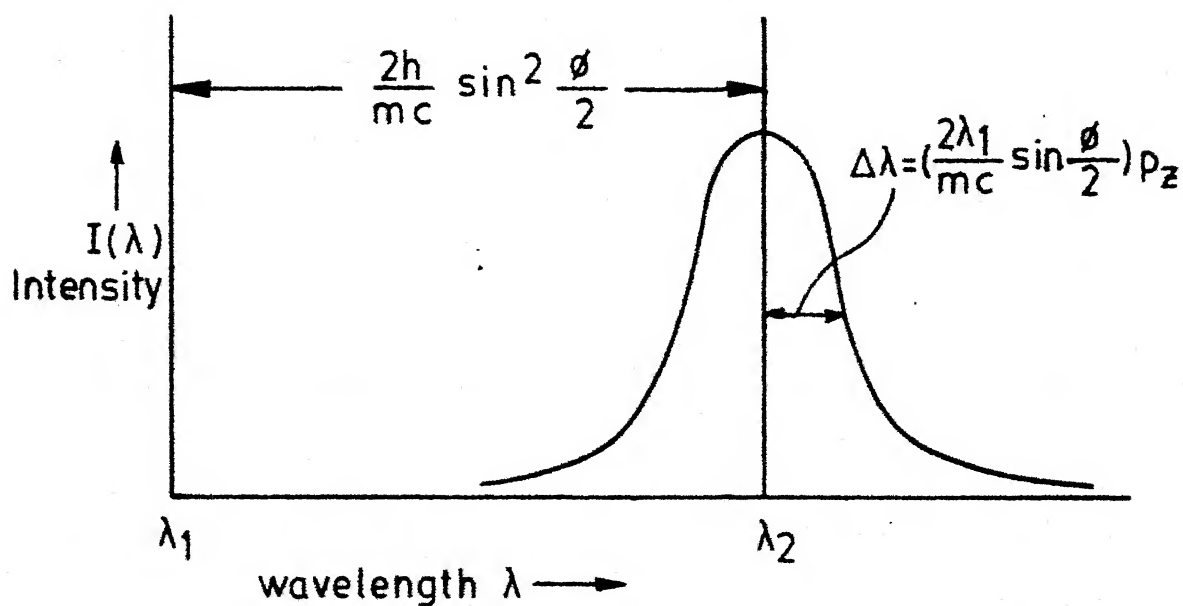


Fig. 1.2: Schematic diagram of the Compton profile.

Compton-scattered line is Doppler-broadened. The energy momentum conservation laws [5] give a modified expression,

$$\Delta\lambda = \frac{2h}{mc} \sin^2 \frac{\phi}{2} - \left(\frac{2\lambda_1}{mc} \sin \frac{\phi}{2} \right) p_z \quad (1.2)$$

where λ_1 is the wavelength of the incident photons, p_z is the z-component of the electron momentum \vec{p} along the scattering vector (which is taken to be z-axis). It is seen from (1.2) that the intensity distribution, $I(\lambda)$, in the scattered radiation lineshape will be determined by the z component of the electron momentum. Such a broadened lineshape or the plot of $I(\lambda)$ versus λ (Fig. 1.2), is generally known as the Compton profile (CP). We shall now briefly discuss the theory of CP in the impulse approximation (IA).

1.2.2 Impulse Approximation:

Consider the inelastic scattering of a photon from a system containing electrons. Let \vec{k}_1 and ω_1 be the wave vector and frequency of the incoming photon while \vec{k}_2 and ω_2 represent corresponding quantities for outgoing photons. A schematic diagram of the process is already shown in Fig. 1.1. The Hamiltonian for an electron in an electromagnetic field is given by,

$$H = \frac{\vec{p}^2}{2m} + V(r) + \frac{e^2}{2mc^2} \vec{A}^2 - \frac{e}{mc} \vec{p} \cdot \vec{A} \quad (1.3)$$

where for simplicity we have considered only a one-electron

system. In (1.3) the terms in \vec{A}^2 and $\vec{p} \cdot \vec{A}$ are to be treated as perturbations. Since the scattering is weak the cross section for the process can be calculated in the lowest order Born approximation. The terms responsible for the scattering are the \vec{A}^2 term in the first order and $\vec{p} \cdot \vec{A}$ term in the second order. It can be shown [12] that for energy transfers large compared to the binding energy of the electrons the contribution from the $\vec{p} \cdot \vec{A}$ term is small and can be neglected. The cross-section for the Compton scattering ($\hbar = c = 1$) is then given by,

$$\frac{d\sigma}{d\Omega d\omega} = \left(\frac{d\sigma}{d\Omega}\right)_{Th} \left(\frac{\omega_1}{\omega_2}\right) \sum_f |\langle f | e^{i\vec{k} \cdot \vec{r}} | i \rangle|^2 \delta(E_f - E_i - \omega)$$

where $(d\sigma/d\Omega)_{Th} = \text{Thomson cross-section}$

$$= \left(\frac{e^2}{4\pi m}\right)^2 (\vec{\epsilon}_1 \cdot \vec{\epsilon}_2) \quad (1.4)$$

$|i\rangle$ and $|f\rangle$ are respectively the initial and final states of the electron, while $\vec{k} = \vec{k}_1 - \vec{k}_2$ and $\omega = \omega_1 - \omega_2$ are respectively the momentum and energy transferred to the electron. The δ -function represents energy conservation and $\vec{\epsilon}_1$ and $\vec{\epsilon}_2$ denote the polarization vectors for the initial and final states of the photon.

We can rewrite (1.4) as

$$\frac{d\sigma}{d\Omega d\omega} = \left(\frac{d\sigma}{d\Omega}\right)_{Th} \frac{\omega_1}{\omega_2} S(\vec{k}, \omega) \quad (1.5)$$

where,

$$S(\vec{k}, \omega) = \sum_f |\langle f | e^{i\vec{k} \cdot \vec{r}} | i \rangle|^2 \delta(E_f - E_i - \omega) \quad (1.6)$$

and $S(\vec{k}, \omega)$ contains all the information about the state of the electron and is known as the dynamical scattering factor. It is related to the EMD and is thus of interest to us.

Now we assume that the energy transferred to the electron during the collision is large compared to the binding energy of the electron. In other words, we assume that the time of the interaction is short enough to consider the particle unbound during the scattering (i.e. the particle sees a constant potential during the interaction). This is the essence of impulse approximation. Under this approximation (IA), $S(\vec{k}, \omega)$ can be written as,

$$S^I(\vec{k}, \omega) = \int d\vec{p} \rho(\vec{p}) \delta(\omega - \frac{k^2}{2m} - \frac{\vec{k} \cdot \vec{p}}{m}) \quad (1.7a)$$

$$= \frac{m}{k} J_{\frac{k}{m}}(q) \quad (1.7b)$$

where $\rho(\vec{p})$ is the EMD and $J_{\frac{k}{m}}(q)$ is the Compton profile (CP) such that

$$\rho(\vec{p}) = |\chi(\vec{p})|^2 = \frac{1}{(2\pi)^3} \left| \int e^{i\vec{p} \cdot \vec{r}} \psi(\vec{r}) d\vec{r} \right|^2 \quad (1.8)$$

and

$$J_{\frac{k}{m}}(q) = \int d\vec{p} \rho(\vec{p}) \delta(q - \vec{p} \cdot \vec{k}) \quad (1.9)$$

where $q = \frac{m\omega}{|\vec{k}|} - \frac{1}{2} |\vec{k}|$, and the quantity q is thus the measure of the electron momentum in the direction of momentum transfer. If z -axis is chosen along \vec{k} , the scattering vector, the expression for CP becomes,

$$J_k(q) = \int_{-\infty}^{+\infty} dp_x dp_y [\rho(\vec{p})]_{p_z=q} \quad (1.10)$$

Equation (1.7a) clearly shows that the scattered photon is shifted in frequency both by a momentum transfer term $(\frac{k^2}{2m})$ and a Doppler shift term $(\frac{\vec{k} \cdot \vec{p}}{m})$. It is seen from (1.9) that the CP is simply a projection of the EMD, $\rho(\vec{p})$, on the scattering vector. The above form (eq.1.8) of $\rho(\vec{p})$ can be extended to a many-electron system, by writing,

$$\rho(\vec{p}) = \sum_i^{\text{occ}} f_i \rho_i(\vec{p}) \quad (1.11)$$

where f_i is the occupancy of the state i .

The simple and straightforward relation (1.10) between EMD and CP rests on the validity of the impulse approximation which is, therefore, very important for the determination of EMD.

1.3 Validity of the Impulse Approximation:

The validity of the IA is studied in some detail by Eisenberger and Platzman [12], and by Currat et al. [13]. By considering 1s hydrogenic systems it is shown [12] that the correction to IA is of the order of $(E_B/E_R)^2$ where E_B

is the binding energy and E_R is the recoil energy of the electron. For a typical X-ray energy (≈ 20 keV) the correction to the IA is quite small for the outer electrons because $E_B \approx 10-100$ eV. A calculation for Li (1s), C(1s) and Al(2s,2p) employing excited state one-electron continuum wavefunctions showed [13] a good agreement with the results employing IA. Examination of the validity of IA and comparison with experimental results indicate that IA adequately describes CP through (1.10). Our calculations described in Chapter 6 are made within the framework of IA.

1.4 Experimental Determination of CP:

An experiment to determine the CP consists of a measurement of the energy spectrum of photons Compton-scattered at a fixed angle θ (Fig. 1.1 and 1.2). Earlier measurements of CP were carried out employing X-rays, from either Ag K_α (22.2 keV) or Mo K_α (17.4 keV) radiation. Experimental arrangement for X-ray Compton scattering is described by Cooper [5]. In 1971, Felsteiner et al. [3] introduced 59.54 - keV gamma rays from ^{241}Am together with a Ge(Li) spectrometer to study CP. Since then the 159.0 - keV gamma rays from ^{123}Te [4] as well as the 412 - keV gamma rays from ^{198}Au [14] have also been employed. The details of the gamma ray Compton scattering experiment and its methodology are described in the literature [4,7,9] and today

almost all the CP measurements are carried out with gamma rays. There are some definite advantages offered by the gamma ray measurements as compared to the earlier X-ray technique [4] .

These are:

- i) The gamma ray sources give monochromatic radiation as compared to the X-ray sources which usually emit a doublet (e.g. $K_{\alpha_1 \alpha_2}$) riding on a continuous background of Bremsstrahlung
- ii) The entire energy spectrum of the scattered gamma rays is accumulated almost simultaneously, unlike the point-by-point wavelength scan in the case of X-rays. This results in the reduction of counting periods.
- iii) The higher energy of gamma rays improve the validity of impulse approximation, allowing the interpretation through (1.10). Secondly the ratio of Compton to photoelectric cross-section goes as $(E\gamma/Z)^3$. The use of gamma rays give a better Compton to photoelectric ratio even for high Z and make it possible to study elements with high Z.

Data from experimentally measured CP have to be processed for effects like detector resolution, multiple scattering, background correction etc. Systematic studies of these effects during the last few years [7] have enabled us to carry out such a data analysis with proper understanding.

We shall now briefly discuss another important technique (viz. ACPAR) used for studying EMD.

1.5 Positron Angular Correlation Studies:

The use of positron annihilation process for investigating solid state properties is now well established [8]. The low energy (≈ 200 keV) positrons emitted from a suitable radioactive source (e.g. ^{22}Na) penetrate into the matter, thermalize in short time ($\approx 10^{-10}$ sec) and then annihilate with electrons. The annihilation characteristics depend almost entirely upon the state of the positron and electron just prior to the annihilation. The information about the annihilation process is transmitted to the observer via the annihilation gamma rays (through parameters like energy, momentum and lifetime) without appreciable attenuation or scattering. These features make the positron annihilation technique attractive for studying the electronic properties of matter.

The experimental techniques involving positron annihilation can be divided into following methods.

- i) Study of two-photon angular correlation,
- ii) Study of Doppler-broadening of annihilation radiation lineshapes,
- iii) Study of positron lifetimes,
- iv) Study of $2\gamma/3\gamma$ yield.

The first two methods are directly related to the study of RMD. In the following we outline the first method.

Consider the process in which the positron annihilates with an electron having antiparallel spin giving rise to two gamma rays. The law of conservation of momentum demands that the emitted photons be collinear in the centre-of-mass system. In the laboratory frame of reference, the annihilating positron-electron pair possesses finite momentum and the annihilating photons, therefore, deviates from collinearity. This deviation can be observed as an angle $\theta_z = p_z/mc$ which is usually of the order of a few milliradians (1 a.u. = 7.3 milliradians). Since the positron is thermalised at the time of annihilation its momentum can be neglected. It is then mainly the momentum of the electron which gives rise to a deviation from collinearity.

Considering the initial state of the system as a product of the ground state electron and positron wavefunctions, the two-photon momentum density, $\rho(\vec{p}')$, is given [8] by

$$\rho(\vec{p}') = \frac{r_0^2 c}{(2\pi)^3} \left| \int \psi_- (\vec{r}) \psi_+ (\vec{r}) e^{-i\vec{p}' \cdot \vec{r}} d\vec{r} \right|^2 \quad (1.12)$$

where $\rho(\vec{p}') d\vec{p}'$ is the probability of annihilation with the emission of a photon pair having a momentum between \vec{p}' and $\vec{p}' + d\vec{p}'$, $\psi_+(\vec{r})$ and $\psi_-(\vec{r})$ are the ground state wavefunctions for the positron and electron respectively, and $r_0 = e^2/mc^2$ is the classical electron radius. For the case of thermalised positron, $\rho(\vec{p}')$ gives a good approximate description of the

EMD itself. However the positron being positively charged tends to keep away from the nucleus and hence annihilates preferentially with the outer (or conduction) electrons. The expression (1.12) is identical (barring some constants) with (1.8) for the case of constant positron wavefunction.

Unlike CP studies, experimental determination of angular correlation of positron annihilation radiation (ACPAR) employs a variety of geometries [9,10]. In the so-called long-slit geometry one measures the coincidence counting rate $N(p'_z)$, which is related to $\rho(\vec{p}')$ through the following relation,

$$N(p'_z) = \iint_{-\infty}^{+\infty} \rho(\vec{p}') dp'_x dp'_y \quad (1.13)$$

Other geometries (e.g. point slit or multi-counter geometry) on the other hand measure a coincidence counting rate,

$$N(p'_y, p'_z) = \int_{-\infty}^{+\infty} \rho(\vec{p}') dp'_x \quad (1.14)$$

An account of how different geometries have been used for the study of Fermi surface (FS) or EMD is given in literature [8,10].

From the above discussion of the two methods it is clear that the momentum density, $\rho(\vec{p})$ or $\rho(\vec{p}')$, plays a central role in the interpretation of the observed profiles (CP or ACPAR). In the next section we shall briefly examine the problem of calculating EMD.

1.6. Calculation of Momentum Density:

1.6.1 The Electron Wavefunction:

Computation of realistic electron wavefunctions in a metal is a major important problem in physics. Earlier theoretical calculations of EMD employed either a free electron or free-atom wavefunctions. Although a number of band structure methods have been available all these years, it is only recently that these methods have been extended to derive momentum wavefunctions and momentum densities. A number of calculations using APW, KKR, OPW etc. are now available.

1.6.2 The Positron Wavefunction:

A knowledge of positron wavefunction, $\psi_+(\vec{r})$, is indispensable for any meaningful interpretation of ACPAR data. The methods [8] commonly used for calculating $\psi_+(\vec{r})$ are a) Wigner-Seitz method or b) plane-wave expansion method. Alternatively one can employ any of the standard band structure methods and calculate $\psi_+(\vec{r})$ for the lowest ($\vec{k}_+ = 0$) state. An interesting method developed by Kubica and Stott [15] employs the concept of pseudopotential for the positron and combines the merits of Wigner-Seitz and plane wave expansion method.

1.6.3 The Positron-Electron Correlations:

Many authors [16,17] have studied the effect of positron-electron correlations on annihilation rates and ACPAR curves

employing many-body theories. Such studies have indicated that the $e^+ - e^-$ correlations have a pronounced effect on the annihilation rates which depend on the effective electron density at the positron site. However, their effect on the momentum distribution curve is less marked and, in particular, the position of the discontinuity in the momentum distribution (at $p = p_F$) shows no shift due to these correlations [16]. This conclusion is especially important for the use of ACPAR curves for FS studies. An analogous result is obtained by Luttinger [18] in the case of interacting electron gas.

1.6.4 The Electron-Electron Correlations:

The electron-electron interaction can play a significant role in the interpretation of CP data from simple (e.g. Li, Na, Al) metals. The properties of the interacting electron gas are studied in some detail [19] and their effect on EMD has also been examined [20]. In our calculation of EMD in transition metals, we have neglected the electron-electron correlation effects, apart from those entering via the one-electron potential.

In the following we shall briefly outline the form of EMD obtained in different cases.

1.6.5 The Free Electron Gas:

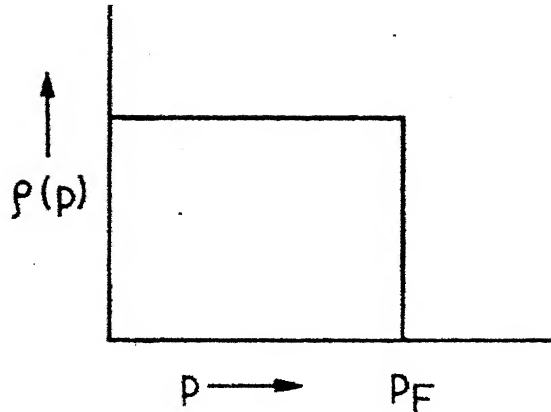
In the case of non-interacting electron gas the momentum density has an isotropic and constant value upto Fermi momentum p_F where it suddenly drops to zero (Fig. 1.3a). In this case the CP or ACPAR is given by the relation,

$$\begin{aligned} N(p_z) &\propto 2\pi (p_F^2 - p_z^2) && \text{if } p_z < p_F \\ &= 0 && \text{if } p_z > p_F \end{aligned} \quad (1.15)$$

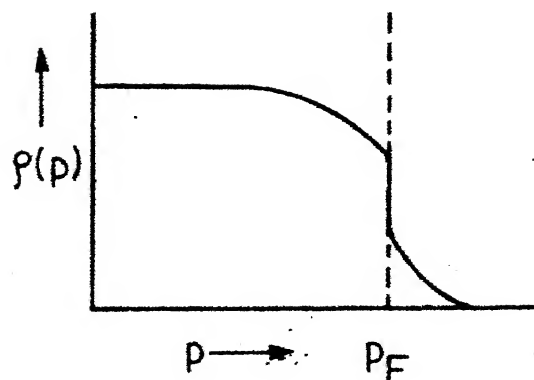
which has parabolic behaviour. However, in the case of interacting electron gas electron-electron correlations push a part of the occupied states below p_F to the higher momenta values. As a consequence the sharp discontinuity smoothens slightly and a tail is developed in the momentum density (Fig. 1.3b).

1.6.6 The Free Atom:

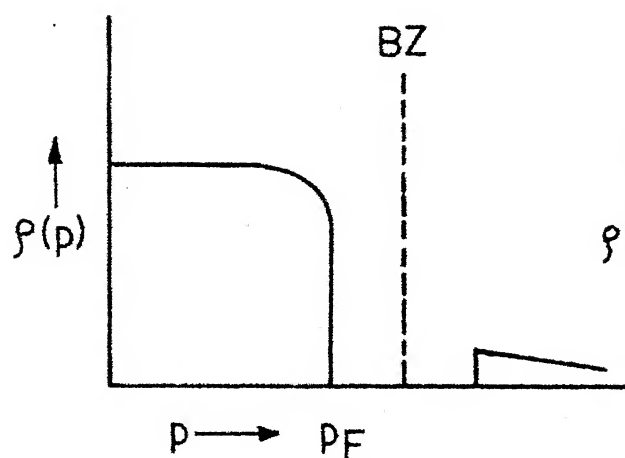
The momentum distribution due to atomic s, p and d electrons (for the same shell) is shown in Fig. 1.4. It is seen that only the s electrons can contribute to EMD at $p = 0$. The reciprocity of the r - and p - space is also quite clear from Fig. 1.4. The wavefunctions which are more spread in r - space are more peaked towards the low-momentum region in the p-space. The momentum distribution in this case, is isotropic and is given by,



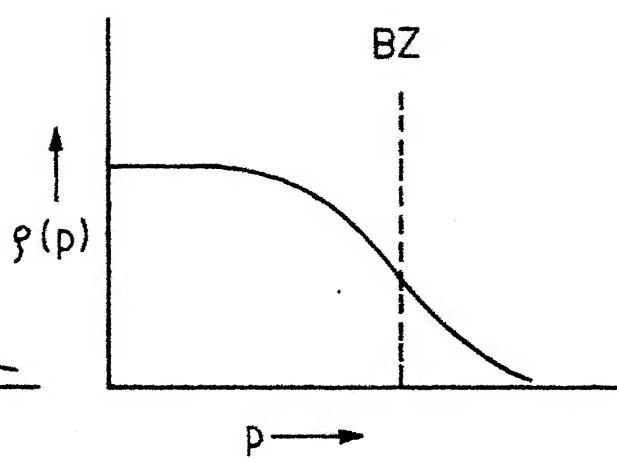
(a) Non-interacting electron gas.



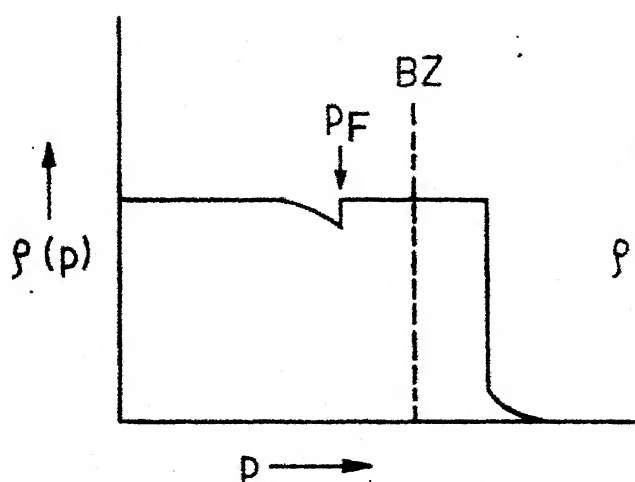
(b) Interacting electron gas.



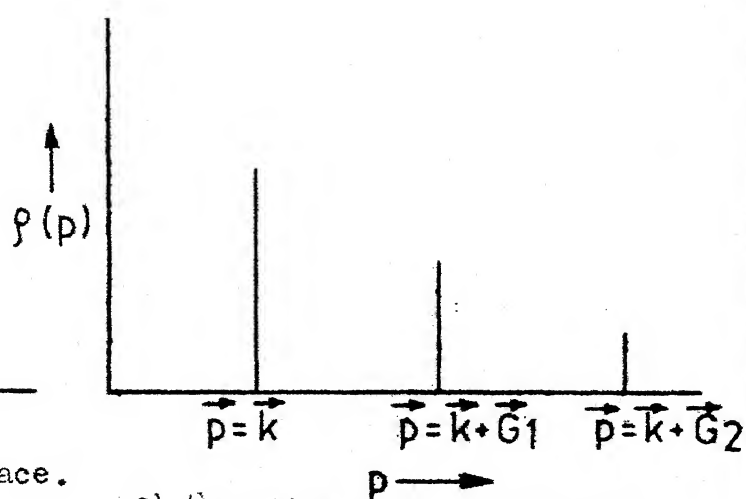
(c) First band Fermi surface.



(d) No Fermi surface.

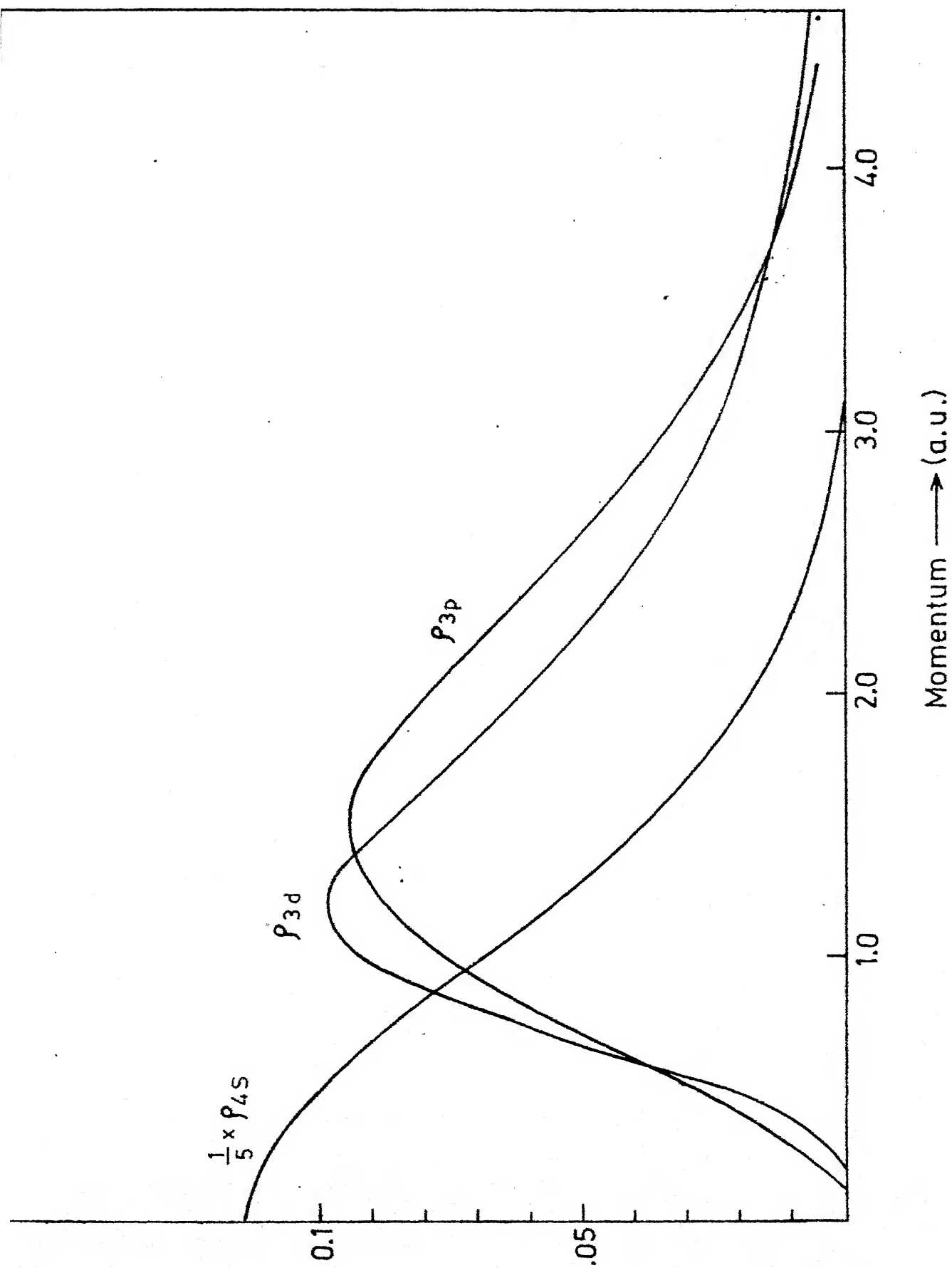


(e) Second band Fermi surface.



(f) One dimensional momentum distribution.

Fig. 1.3: The momentum distributions for various cases.



$$\rho_{nl}(p) = \frac{2(2l+1)}{4\pi} \left(\frac{2}{\pi}\right) \left| \int_0^\infty dr r^2 P_{nl}(r) j_l(pr) \right|^2 \quad (1.16)$$

where $P_{nl}(r)$ are atomic wavefunctions. Usually the 'core' contribution to the EMD in metals is calculated by using (1.16).

1.6.7 The Conduction Electrons:

In the case of metals, the conduction electrons, as well as the positron states are Bloch states. The wavefunction of an electron in a state \vec{k} and band j can be written as,

$$\psi_{\vec{k},j}(\vec{r}) = u_{\vec{k},j}(\vec{r}) e^{i\vec{k} \cdot \vec{r}} \quad (1.17)$$

$$\text{with } u_{\vec{k},j}(\vec{r}) = \sum_{\vec{G}} c_{\vec{G}}(\vec{k}) e^{i\vec{G} \cdot \vec{r}} \quad (1.18)$$

where $c_{\vec{G}}$ are the momentum wavefunctions and \vec{G} 's are the reciprocal lattice vectors. In a similar fashion the plane wave expansion of positron wavefunction $\psi_{\vec{k}=0}(\vec{r})$ would give

$$\psi_{\vec{k}=0}(\vec{r}) = \psi_+(\vec{r}) = \sum_{\vec{G}'} e_{\vec{G}'} e^{i\vec{G}' \cdot \vec{r}} \quad (1.19)$$

The momentum densities for the two cases are then given by,

$$\begin{aligned} \rho(\vec{p}) &= \sum_{\vec{k},j} \rho_{\vec{k},j}(\vec{p}) \\ &= \sum_{\vec{k},j} \sum_{\vec{G}} |c_{\vec{G}}(\vec{k})|^2 \delta(\vec{p} - \vec{G} - \vec{k}) \end{aligned} \quad (1.20a)$$

and

$$\rho(\vec{p}') = \sum_{\vec{k}, j} \sum_{\vec{G}'} |c_{\vec{G}'}'(\vec{k})|^2 \delta(\vec{p}' - \vec{G}' - \vec{k}) \quad (1.20b)$$

where

$$c_{\vec{G}'}(\vec{k}) = \sum_{\vec{G}} B_{\vec{G}} c_{\vec{G}-\vec{G}'}(\vec{k}) \quad (1.20c)$$

In(1.20) the first summation indicates that all the occupied states below the Fermi level should be considered. The second summation, together with the δ -function shows that electrons in state \vec{k} will contribute not only at momenta $\vec{p} = \vec{k}$ (normal or N-process) but also at momenta $\vec{p} = \vec{k} + \vec{G}$ (Umklapp or U-process). The contributions to $\rho(\vec{p})$ from the states in completely filled zone will be continuous but that from partially filled zones will be non-zero only at \vec{p} such that $(\vec{p} - \vec{G})$ lies inside the FS. The momentum density then exhibits discontinuities not only at $\vec{p} = \vec{p}_F$ but at $\vec{p} = \vec{p}_F + \vec{G}$ also, its magnitude being weighted by a factor $c_{\vec{G}}(\vec{k})^2$. Fig. 1.3c, 1.3d, 1.3e, and 1.3f shows the behaviour of $\rho(\vec{p})$ for some interesting cases. In this manner the effects due to i) Fermi surface ii) momentum wavefunctions and iii) U-processes combine to build the EMD, $\rho(\vec{p})$ and consequently the CP, $J(q)$ or ACPAR, $N(p_z)$, curves.

The inner 'core' states being nearer nucleus give an appreciable contribution in the high momentum region (so-called high momentum components, HMC). In the case of positron

annihilation, the overlap of positron -electron wavefunction is appreciable at large r -values and the HMC arise mostly out of the U-processes. For Compton scattering, however, the HMC derive their contributions from the core states as well as from the U-processes.

Unless a pseudopotential method is used, one does not calculate the actual electron states in solids using plane wave expansion (1.17). Although the details of $\rho(\vec{p})$ may change depending on the method used, essential form of $\rho(\vec{p})$ remains same.

Details of a band structure method for the calculation of EMD will be discussed in Chapter 3.

1.7 Comparison of CP and ACPAR Techniques:

A comparison of the CP and ACPAR methods [9] is given in Table 1.1. From experimental point of view, the choice of various geometries and superior momentum resolution are the main advantages of ACPAR method. However, for theoretical interpretation, it is more straightforward to calculate CP which do not require a knowledge of positron wavefunctions. The CP and ACPAR methods can be complimentary to each other and it is desirable to experimentally study the same systems by both the techniques as well as to theoretically calculate the two momentum densities employing same method and same electron wavefunctions.

Table 1.1

Comparison between positron annihilation and Compton
profile methods

Feature	Angular correlation of positron annihilation radiation with LS geometry	Compton profile
Probe	Positron	Photon
Quantity measured	Angular correlation of the annihilation photon pair $N(p_z)$	Intensity distribution of the energy spectrum of the scattered photon $J(p_z)$
Information provided and assumptions of validity	$N(p_z) = \iint \rho(p) dp_x dp_y$ (i) Positron is thermalized before annihilation; (ii) positron-electron correlation is negligible	$J(p_z) = \iint \rho(p) dp_x dp_y$ impulse approximation
Typical momentum resolution	0.07 at. units	0.4 at. units
Counting efficiency	Relatively low, typical counting periods of 1 week per (hkl) direction	Higher if γ -rays and Ge(Li) detectors are used; typical counting periods of 2 to 3 days per (hkl) direction
Quality of the samples (single crystals)	Must be free from defects; surface purity very essential	Optimum thickness necessary; too thin samples would give poor yields, while too thick samples will cause multiple scattering effects
Data corrections	Straightforward	Complicated.

1.7.1 Comparison Between Theory and Experiment:

As far as EMD is concerned two approaches are available for a comparison between theory and experiment. First method consists of reconstructing the EMD, $\rho(\vec{r})$, from CP (or ACPAR) curves measured for a number of different orientations of a single crystal specimen, and comparing this reconstructed EMD with theoretical EMD. Alternatively, one can theoretically calculate a 'model' EMD and obtain single crystal CP (or ACPAR) curves $J(q)$ or the anisotropies $J_{hkl} - J_{h'k'l'}$, using (1.10). Although the former 'unfolding' method, employing an expansion of $\rho(\vec{r})$ in terms of lattice harmonics, as suggested by Mijnaerends [2] has been tried on several metals, it has not yet proved to be a unique method owing to the problems inherent in any 'unfolding' or 'deconvolution'. Perhaps a better strategy is to combine the above two methods.

In view of this we have extended (Chapter 6) our calculations of EMD to predict directional CP curves and their anisotropies.

1.8 Motivation Behind Our Present Work:

In this section we wish to lay down the motivation behind our present work.

It is seen from above that for any meaningful comparison between theoretical and experimental CP or ACPAR curves, a

calculation of the EMD is essential. Among metals, the EMD of transition metals is one of the most interesting because of their interesting electronic structure [22,23]. The best approach for calculating the EMD of transition metals is the band structure method so that the effects on EMD due to Fermi surface, the d bands, s-d hybridization etc. can be properly examined. The EMD in 4d transition metals hitherto appears to be an unexplored area except for the work on Nb [24] and Mo [25].

We found it interesting to calculate the EMD of Pd and Ag for the following reasons. In the first place the EMD of the 3d metals Ni and Cu, isoelectronic with the 4d metals Pd and Ag have been well studied theoretically [26] and experimentally [27]. It should, therefore, be interesting to study the EMD in Pd and Ag and compare it with Ni and Cu (all fcc metals) to examine the effects of band structure, Fermi surface etc. Again, the band structure and electronic properties of Pd are among the most fascinating among the 4d metals [28]. In view of the fact that there are not many band structure calculations for the 4d metals, we thought it better to employ the fast but approximate method of Hubbard and Mijnen [26] rather than use a more sophisticated band structure method. Calculations of EMD in Ni and Cu employing Hubbard-Mijnen method are already available [26] so a direct comparison of

these results is also possible. It is true that ~~now~~ experimental data on Compton profiles of Pd and Ag is yet available for a comparison between theory and experiment but it is expected that such studies on heavy metals employing 412-keV gamma rays would soon be made [14]. Until then our studies provide computer-simulated Compton scattering studies of Pd and Ag and can perhaps provide suggestions for designing and analyzing an actual experiment. In the absence of any experimental data, the emphasis in our approach in the present work has been to study the role of band structure and Fermi surface on EMD. In other words, we feel that EMD is yet another ground state property (e.g. electronic specific heat, susceptibility etc.) which can be predicted by a band structure calculation and compared with experiment. In the past such calculations in momentum space have been ignored and we feel that our calculations provide a systematic review of the results of EMD in transition metals. To this end, we have discussed in Chapter 5, systematics of the EMD in 3d metals. Again a comparison between the EMD for Compton scattering, $\rho(\vec{p})$, and the two-photon momentum distributions, $\rho(\vec{p}')$, is very instructive and interesting. The angular correlation of positron annihilation in Pd, Ag and Pd-Ag alloys are being studied theoretically and experimentally [29] and we feel that our EMD calculations can prove interesting and complementary data for such a comparison.

Lastly we felt that a comparison of theory and experiment in this area can be made more sensitively through the anisotropies ($J_{111} - J_{100}$ etc.) than through single crystal profiles, J_{hkl} . We have therefore extended our EMD calculations in Chapter 6 to predict the anisotropies in Pd and Ag.

REFERENCES

1. J.W.M. DuMond, Phys. Rev. 33, 643 (1929); Rev. Mod. Phys. 5, 1 (1933).
2. M. Cooper, J.A. Leake and R.J. Weiss, Phil. Mag: 12, 797 (1965).
3. J. Felsteiner, R. Fox and S. Kahana, Phys. Lett. A 33, 442 (1970); Solid State Commun. 9, 61 (1971).
4. P. Eisenberger and W.A. Reed, Phys. Rev. A5, 2085 (1972).
5. M. Cooper, Adv. Phys. 20, 453 (1971).
6. A very readable review of the Compton profile technique, particularly from a chemist's point of view is given by I.R. Epstein in MTP International Review of Science, Physical Chemistry, Series II, Theoretical Chemistry.
7. The Compton Effect, edited by B.G. Williams, McGraw-Hill (1975).
8. R.N. West, Adv. Phys. 22, 263 (1973); Proceedings of Third International Conference on Positron Annihilation, Otaniemi, Finland (1973), edited by P. Hautajarvi and A Seeger. Also see, I.Ya. Dekhtyar, Phys. Rep. 9C, 243 (1974).
9. R.M. Singru, Phys. Status Solidi B, 30, 11 (1975).
10. S. Berko and J. Mader, Appl. Phys. 5, 287 (1975).
11. S. De Benedetti, C.E. Cowan, W.R. Konneker and H. Primakoff, Phys. Rev. 77, 205 (1950).
12. P. Eisenberger and P.M. Platzman, Phys. Rev. A2, 415 (1970).
13. R. Currat, P.D. DiCicco and R.J. Weiss, Phys. Rev. B4, 4256 (1971).
14. M. Cooper, P. Pattison and J.R. Schneider (Private communication).
15. P. Kubica and M.J. Stott, Appl. Phys. 4, 213 (1974).

16. C.K. Majumdar, Phys. Rev. 140, A 227 (1965).
17. S. Kahana, Phys. Rev. 129, 1622 (1963), see also: Positron Annihilation, Academic Press: New York and London, 1967; A.K. Rajgopal and C.K. Majumdar, Prog. Theo. Phys. 44, 13 (1970). More complete references can be found in Ref. 8.
18. J.M. Luttinger, Phys. Rev. 119, 1153 (1960).
19. See, for example P. Nozieres, The Theory of Interacting Fermi Systems (W.A. Benjamin Inc. New York, 1964).
20. L. Lam and P.M. Platzman, Phys. Rev. B9, 5122 (1974) and the references therein.
21. P.E. Mijharends, Phys. Rev. 160, 512 (1967).
22. J. Friedel in, The Physics of Metals, I. Electrons, edited by J.M. Ziman.
23. J. Callaway, Energy Band Theory (Academic Press: New York and London, 1964).
24. S. Wakoh, T. Fukamachi, S. Hosoya and J. Yamashita, J. Phy. Soc. Jap. To be published.
25. S.M. Kim and W.J.L. Buyers, Can. J. Phys. 50, 1777 (1972).
26. P.E. Mijharends, Physica (Utr.) 63, 235 (1973); R.M. Singru and P.E. Mijharends, Phys. Rev. B9, 2372 (1974); C.S. Wang and J. Callaway, Phys. Rev. B11, 2417 (1975).
27. P. Eisenberger and W.A. Reed, Phys. Rev. B9, 3242 (1974).
28. F.M. Muller, A.J. Freeman, J.O. Dimmock and A.M. Furdyna, Phys. Rev. B1, 4617 (1970).
29. P.E. Mijharends, Private communication.

Chapter 2

ELECTRON MOMENTUM DISTRIBUTION IN NICKEL AND COPPER EMPLOYING RENORMALIZED-FREE-ATOM MODEL^{*}

2.1 Introduction:

In this Chapter we present an application of the renormalised-free-atom (RFA) model to the calculation of EMD. The RFA model was developed by Hodges et al. [1] who applied it to calculate some ground state properties of the transition metals. Berggren [2] employed RFA wavefunctions to calculate the EMD for Compton scattering in Ti [3], V [4], and Fe [4] and showed that the gross features of the CP data could be described by this computationally simple model. We have extended this method to the calculation of EMD for positron annihilation and have calculated the CP and ACFAR curves in Ni and Cu, and compared them with the experiment.

The motivation for the present work was as follows:

- 1) To test whether the RFA model is valid equally for describing positron annihilation and Compton scattering processes.

^{*} Work described in this Chapter is already published as a paper: D.G. Kanhere and R.M. Singru, J. Phys. F. Metal Phys. 5, 1146 (1975).

2) To apply the RFA model to calculate CP and ACPAR curves for Ni and Cu for which experimental data as well as band structure calculations of EMD exist. An overall comparative study of all these results can thus become instructive.

3) To test the sensitivity of the RFA results to the outer electronic configuration (i.e. $3d^8 4s^2$ vs. $3d^9 4s^1$ for Ni) of the transition metals.

2.2 RFA Model:

In the RFA model [1] one starts with the free-atom Hartree-Fock wavefunctions for outer electrons and truncates them at the radius (r_{WS}) of the Wigner-Seitz (WS) sphere. The wavefunctions are then renormalised to unity within the WS sphere to preserve charge neutrality. In this way the free atoms are 'prepared' in an approximate way to enter the solid and in a 3d-transition metal such renormalised-free-atom wavefunctions should give a fair description [2] of the true crystal wavefunction at $\vec{k} = 0$. It has been shown [1] that the RFA model gives fairly accurate estimates of some of the band structure properties for 3d-transition metals.

In our calculations we employed the free-atom orbital wavefunctions $P_{nl}(r)$ as given by Herman and Skillman [5]. Only the free-4s-atom wavefunctions were renormalised after

which they seemed to satisfy the WS boundary condition $P'_{4s}(r) = 0$ at $r = r_{WS}$ only approximately. It must be remembered that in this approximation (RFA model) we have assigned the momentum eigenfunctions calculated for the $\vec{k} = 0$ electrons to all the 4s electrons. The 3d wavefunctions were not renormalised (see Sec. 2.6).

2.3 Compton Profiles:

The procedure followed by us for computing the CP curves was very similar to the one described by Berggren [2]. For the sake of completeness, we reproduce below the important formulas used by us. The contribution by 4s electrons ($\vec{k} = 0$) was evaluated by writing the EMD per atom as

$$\rho(\vec{p}) = 2 \sum_{\vec{k}} \delta_{\vec{p}-\vec{k}-\vec{K}_n} |\psi_0^c(\vec{K}_n)|^2 \quad (2.1)$$

where the summation is over all occupied states and the momentum transform

$$\psi_{\vec{k}}^c(\vec{p}) = (2\pi)^{-3/2} \int d^3r e^{-i\vec{p} \cdot \vec{r}} \psi_{\vec{k}}(\vec{r}) \quad (2.2)$$

is related to $\psi_0^c(\vec{K}_n)$ by the identity $\psi_{\vec{k}}^c(\vec{p}) = \psi_0^c(\vec{K}_n)$ through the relation $\vec{p} - \vec{k} = \vec{K}_n$.

Before replacing the region of integration in Eq. (2.2) by the WS sphere an appropriate correction [6] was applied. The final expression used for the isotropic Compton profile was,

$$J_{4s}(p_z) = 4\pi \sum_{n=0} |\psi_o^c(\vec{K}_n)|^2 G_n(p_z) \quad (2.3)$$

where the functions G_n are given by Berggren [2-4].

The isotropic contribution by core ($1s^2 2s^2 2p^6 3s^2 3p^6 3d^n$) electrons was obtained by extreme tight binding approximation in which the EMD is written as,

$$\rho_{nl}(p) = \frac{2(2l+1)}{4\pi} \left(\frac{2}{\pi}\right) \left| \int_0^\infty dr r^2 P_{nl}(r) j_l(pr) \right|^2 \quad (2.4)$$

where $P_{nl}(r)/r$ are the free-atom orbital wavefunctions [5] and $j_l(pr)$ is the spherical Bessel function. The whole procedure was tested by calculating the Compton profile for polycrystalline V. These calculations gave good agreement with the results of Berggren [2] for V.

2.4 Positron Wavefunction:

The positron wavefunction $\psi_+(\vec{r})$ was calculated by a plane wave expansion

$$\psi_+(\vec{r}) = \Omega^{-1} \sum_{\vec{K}} A_{\vec{K}} e^{-i\vec{K} \cdot \vec{r}} \quad (2.5)$$

described in earlier reports where the results for $\psi_+(\vec{r})$ for three symmetry directions [100], [110] and [111] for Ni [7] and Cu [8] are also shown. For the computation of isotropic $\rho(p')$, the positron wavefunction was spherically averaged by the method described earlier [7].

2.5 Positron Angular Correlation:

The momentum density $\rho(\vec{p}')$ of the two photon pair arising from positron annihilation with 4s electrons is given [6] by

$$\rho(\vec{p}') = 2 \sum_{\vec{k}} \delta_{\vec{p}' - \vec{k}, \vec{K}_n} |C_{\vec{k}}(\vec{K}_n)|^2 \quad (2.6)$$

where the summation includes all the occupied states and $C_{\vec{k}}$, the Fourier transform of the product of electron and positron wavefunctions, is defined as

$$C_{\vec{k}}(\vec{p}') = (2\pi)^{-3/2} \int d\vec{r} e^{-i\vec{p}' \cdot \vec{r}} \psi_+(\vec{r}) \psi_{\vec{k}}(\vec{r}) \quad (2.7)$$

As before, making use of the relation $\vec{p} - \vec{k} = \vec{K}_n$ and remembering that in the RFA model used by us $\vec{k} = 0$ for the 4s-electrons we have $C_{\vec{k}}(\vec{p}') = C_0(\vec{K}_n)$.

Taking a spherical average and integrating as before (2.3) we can get the expression for ACPAR curve for long slit geometry as,

$$N_{4s}(p'_z) = 4\pi \sum_{n=0}^{\infty} |C_0(\vec{K}_n)|^2 G_n(p'_z) \quad (2.8)$$

The isotropic contribution from the core electrons was obtained (Compare Eq. (2.4)) by employing,

$$\rho_{nl}(p) = \frac{2(2l+1)}{4\pi} \left(\frac{2}{\pi}\right) \left| \int_0^{\infty} dr r^2 R_+(r) P_{nl}(r) j_l(p'r) \right|^2 \quad (2.9)$$

where $R_+(r)/r$ described the spherically averaged positron wavefunctions and other quantities were the same as that of Eq. (2.4).

2.6 Results and Discussion:

2.6.1 Compton Profiles:

The CP curves for polycrystalline Ni and Cu resulting from our calculations are presented in Figs. 2.1 and 2.2 where they are also compared with the experimental gamma ray Compton profiles of Eisenberger and Reed [9] by normalising to same total areas (including the extrapolated areas beyond $p_z = 5.0$). It is seen that the RFA model used by us predicts satisfactory CP curves for Ni and Cu, as it did for Ti [3], V [2] and Fe [4]. A band calculation of the CP curves for Ni is reported by Rath et al. [10] and their curve gives a closer agreement with the experiment (see Fig. 1, Ref. 10).

The sensitivity of CP curves (in the low momentum region) to the choice of electronic configuration has already been demonstrated for V [2] and Ti [3]. We have repeated such an exercise for nickel, for which the atomic configuration is $3d^8 4s^2$, while the configuration compatible with solid state experience is closer to $3d^9 4s^1$. Fig. 2.3 shows a comparison of the CP curves calculated in different ways. As expected, the free-atom wavefunctions for a $3d^8 4s^2$ configuration show the widest divergence from the experimental curve while the RFA

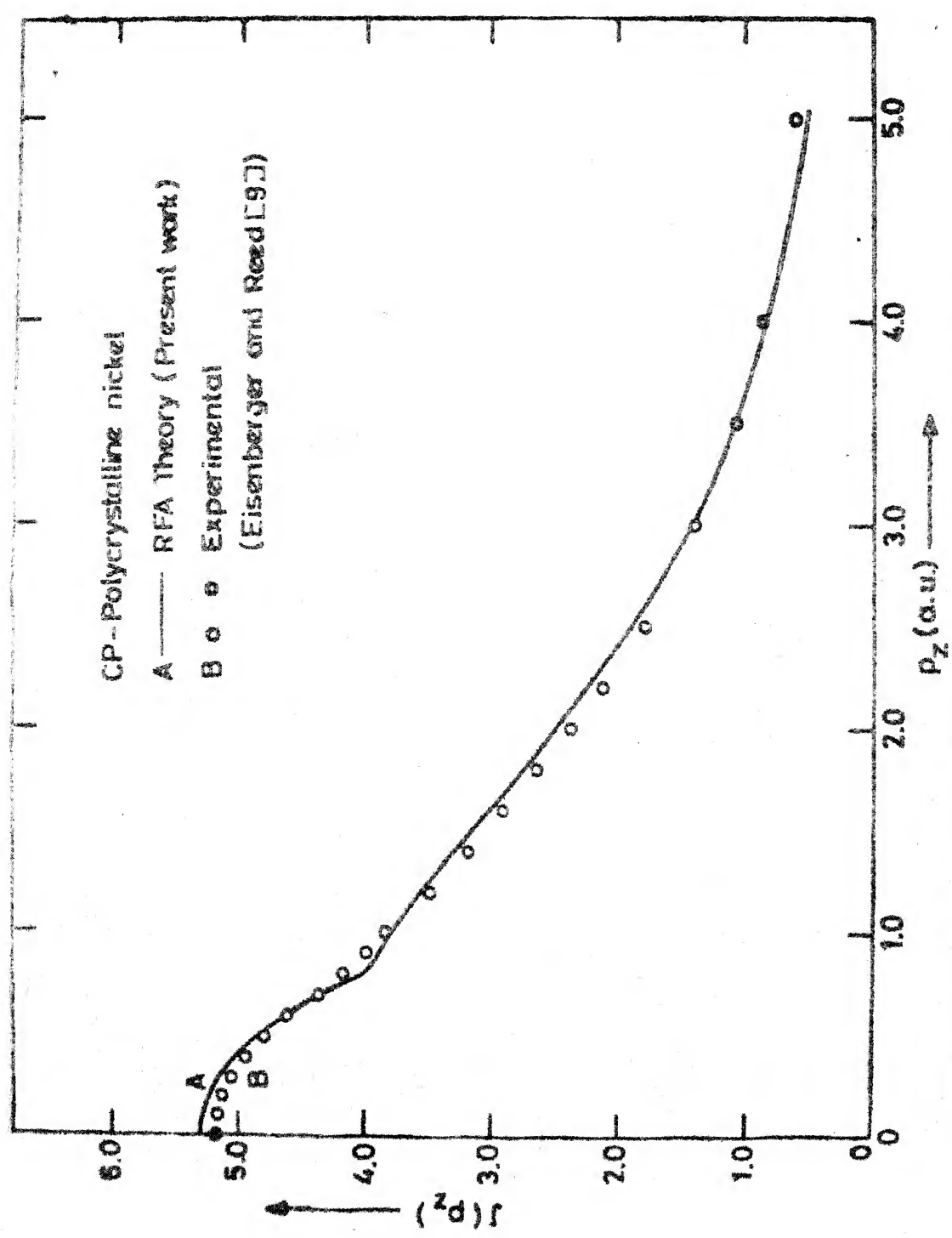
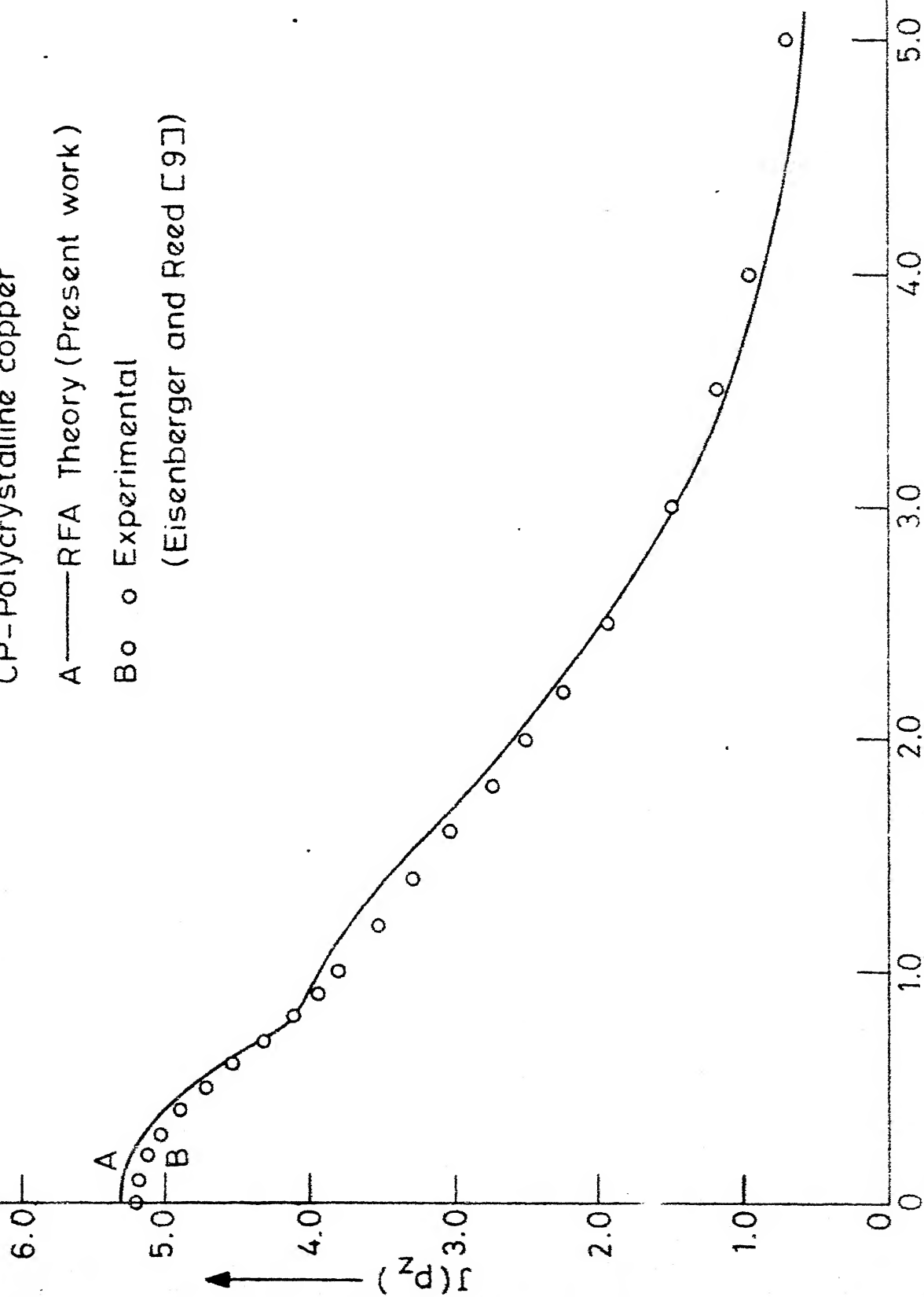


Fig. 2.1: Calculated and experimental Compton profiles of polycrystalline nickel.

CP-Polycrystalline copper
 A — RFA Theory (Present work)
 B o Experimental
 (Eisenberger and Reed [9])



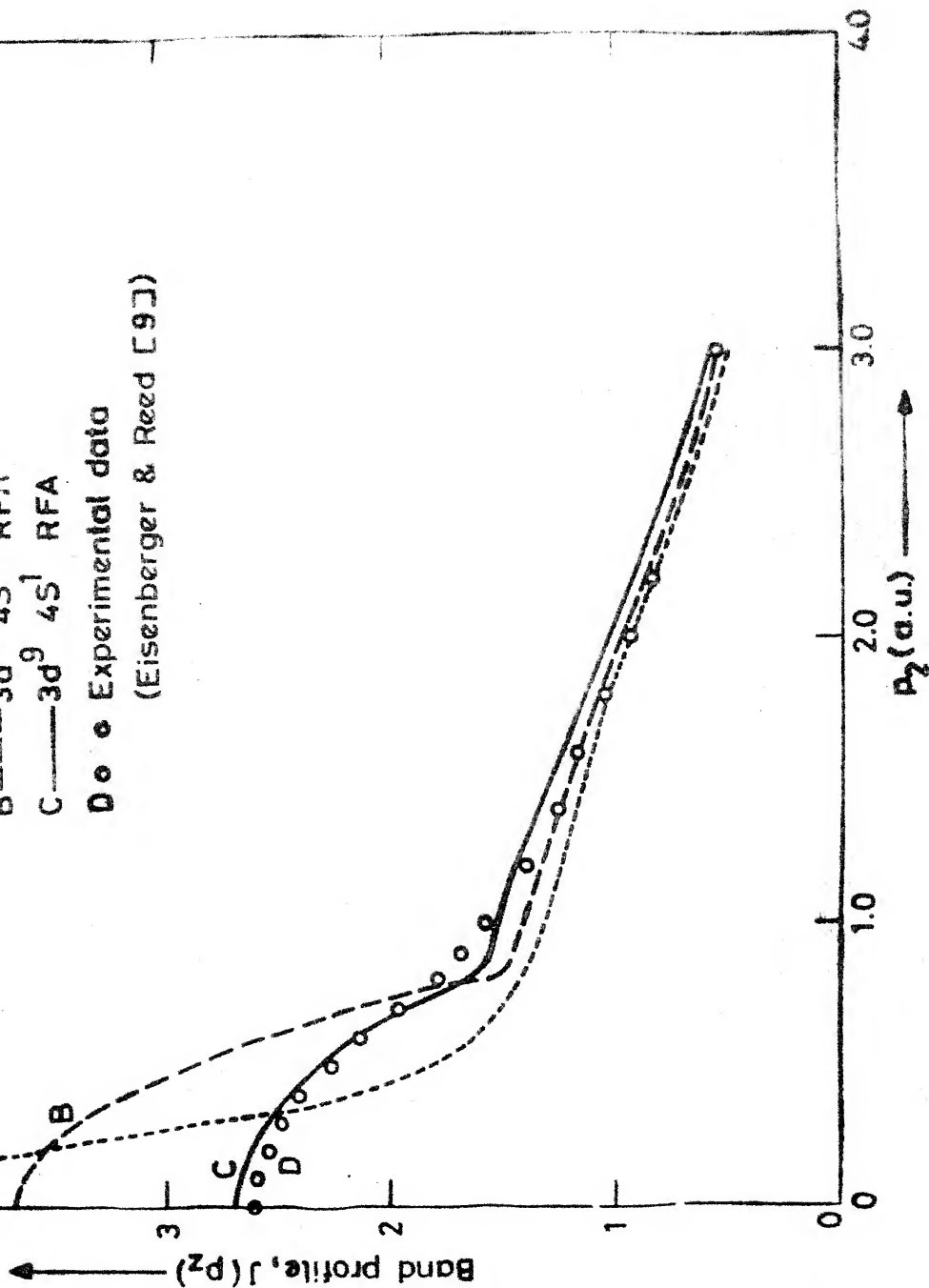
CP- Band profile for Ni

A-----3d⁸ 4s² free-atom

B-----3d⁸ 4s² RFA

C-----3d⁹ 4s¹ RFA

D ○ ● Experimental data
(Eisenberger & Reed [9])



wavefunctions for a $3d^9 4s^1$ configuration show closest agreement. Earlier APW calculations [11] for nickel have suggested an electronic configuration $3d^{10-x} 4s^x$ with $0.5 < x < 1.0$. Our calculations indicate that the RFA curve based on such a configuration would give a closer agreement with experiment.

It has been suggested [2] that a better way to compare the theoretical curve with experiment is to subject the theoretical curve to a convolution and deconvolution by the proper detector response function. Such a procedure has the effect of smoothing the kink in the theoretical curve (Fig. 2.1) and improving its agreement with experiment. The RFA curves in Figs. 2.1 and 2.2 would show a better agreement if such a procedure is followed.

2.6.2 Positron Annihilation:

The results of our calculations on the momentum density for positron annihilation are summarised in Tables 2.1 and 2.2 which show the values of Fourier components $C_{\vec{k}}$ (Eq. (2.7)) for the 4s-electrons of nickel and copper. In the case of copper a comparison with earlier results (Table 2.2) is shown, the difference between the two being due to the different approaches used to describe the electron and positron states.

Table 2.1

Table of Fourier Components for nickel

$(2\pi/a) K_n$	[000]	[111]	[200]	[220]	[311]
$C_o (K_n)$					
(Present work)	0.925	-0.078	-0.075	-0.034	+0.008

Table 2.2

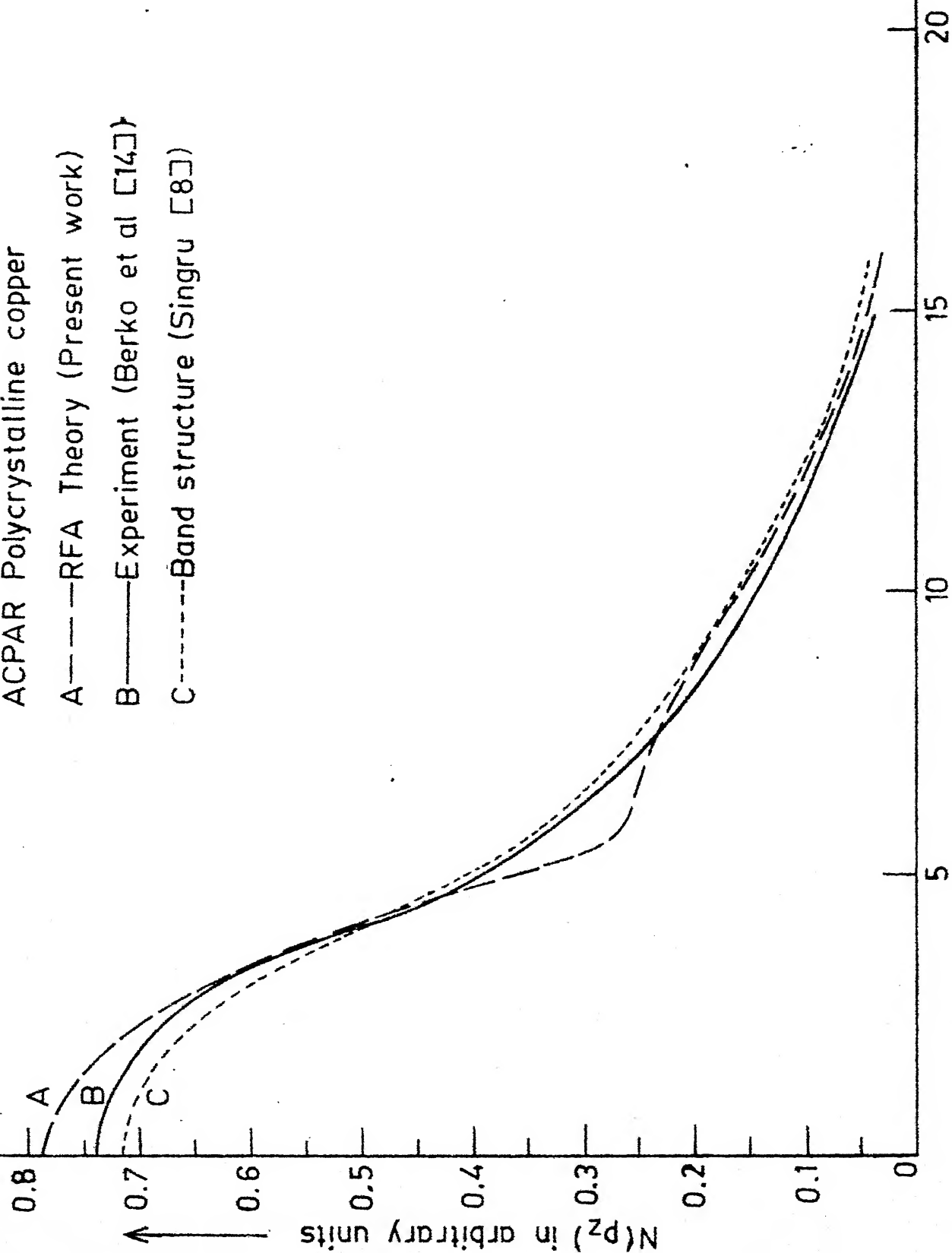
Table of Fourier Components for copper

$(2\pi/a) K_n$	[000]	[111]	[200]	[220]	[311]
$C_o (K_n)$					
Present work	0.925	-0.078	-0.068	-0.013	+0.007
$C_o (K_n)$					
(Berko and Plaskett [6])	0.953	-0.127	-0.087	-0.009	+0.006

The theoretical ACPAR curves (for long slit geometry) for polycrystalline nickel and copper calculated by us are presented in Fig. 2.4 and 2.5 where a comparison with the experimental curves and with the band structure calculations is also given. It is evident that the RFA model does not describe the positron annihilation data as well as it does the Compton scattering data. In particular the RFA curve shows a marked deviation (e.g. the deep kink) in the region around the Fermi momentum (p_F) as well as in the very low momentum region. It must be remembered, however, that as compared to Compton scattering, positrons (because of their positive charge) sample the outer electrons with a greater degree of overlap. For example, for copper the ratio $N_{4s,3d}(p_z = 0); N_{total}(p_z = 0)$ is about 0.5. As a result, the band structure effects assume greater importance for positron annihilation. This argument is supported by the relatively better agreement between the experiment and band structure calculations (shown in Figs. 2.4 and 2.5). This is not surprising because the band structure calculations take into account the exchange-correlation effects of the d-electrons, hybridization and most important of them all the details of the Fermi surface shapes. The residual disagreement (Figs. 2.4 and 2.5) between the experiment (curve B) and the band structure calculations (curve C) could be due to possible enhancement effects, uncertainties in the spherical averaging etc. However our results suggest that RFA model gives a poor description of the 4s-electrons vis-a-vis positron annihilation.

ACPAR Polycrystalline copper

- A---RFA Theory (Present work)
- B——Experiment (Berko et al [14])
- C-----Band structure (Singru [8])



It might be argued that in view of the large number of 3d electrons in nickel and copper the effect of renormalization of the 3d-states should be included [2]. Our calculations indicated that renormalization of 3d-states had the effect of broadening the curves and widening the deviations between RFA theory and experiment. It may be pointed out that a comparison of different results of positron annihilation studies in copper [12] indicates that the 3d-electrons are more spreadout in position space than the free-atom wavefunctions indicate. This might perhaps be due to the possibility that the effect of renormalization of 3d-wavefunctions and the effect of the d-hybridization with conduction band act in opposite directions. Considering all this, we did not renormalise the 3d-states in our calculations.

2.7 Conclusions:

Referring back to the motivation behind this work we conclude that

- a) RFA model cannot give a satisfactory description of the positron annihilation process for which a detailed calculation employing band structure is necessary.
- b) It gives a satisfactory but gross description of the overall features of the Compton profile of Ni and Cu.

c) Our results support an electronic configuration closer to $3d^9 4s^1$ for Ni.

However, the finer details and particularly the anisotropies of the Compton profiles cannot be described without a proper band structure calculation and hence the applicability of the RFA model is limited.

In the next Chapter we shall describe our band structure calculations of EMD.

REFERENCES

1. L. Hodges, R.E. Watson and H. Ehrenreich, Phys. Rev. B5, 3953 (1972).
2. K.-F. Berggren, Phys. Rev. B6, 2156 (1972).
3. K.-F. Berggren, S. Manninen and T. Paakkari, Phys. Rev. B8, 2156 (1973).
4. K.F. Berggren, Momentum Densities: An Outline of Theoretical Calculations, Report LiH-IFM-IS-28, University of Linköping, S-581 83, Linköping, Sweden (Unpublished).
5. F. Herman and S. Skillman, Atomic Structure Calculations, (Prentice-Hall: Englewood Cliffs, New Jersey 1963).
6. S. Berko and J.S. Plaskett, Phys. Rev. 112, 1877 (1958).
7. R.M. Singru and P.E. Mijnders, Phys. Rev. B9, 2372 (1974).
8. R.M. Singru, Pramana 2, 299 (1974).
9. P. Eisenberger and W.A. Reed, Phys. Rev. B9, 3242 (1974).
10. J. Rath, C.S. Wang, R.A. Tawil and J. Callaway, Phys. Rev. B8, 5139 (1973). C.S. Wang and J. Callaway, Phys. Rev. B11, 2417 (1975).
11. E.C. Snow, J.T. Waber and A. Switendick, J. Appl. Phys. 37, 1342 (1966).
12. J. Melngailis, Phys. Rev. B2, 563 (1970).
13. N. Shiotani, T. Okada, H. Sekizawa, T. Mizoguchi and T. Karasawa, J. Phys. Soc. Jap. 35, 456 (1973).
14. S. Berko, S. Cushner and J.C. Erskine, Phys. Lett. 27A, 668 (1968).

Chapter 3

BAND STRUCTURE METHOD FOR CALCULATION OF MOMENTUM DENSITIES

3.1 Introduction:

It was seen in the last chapter that for a detailed and quantitative analysis of the CP and ACPAR data, especially for predicting the anisotropies, theoretical calculations employing band structure methods are essential. For doing band structure calculations one has a choice of using any of the available standard methods (e.g. APW, KKR etc.) which are known to give good results for other ground state properties of transition metals. As emphasized in Chapter 1, our aim is to analyze the EMD in a physically transparent manner, clearly bringing out the role of d bands, the structure of Fermi surface and in general the electronic structure of transition metals. Therefore, instead of opting for an accurate, sophisticated and time-consuming method, we tried to seek a fast, but approximate method which can meet our needs. Towards this aim we have chosen Hubbard's method [1] especially developed for transition metals. This method has already been employed to calculate the EMD in Cu [2,3] Fe [2,4] and Ni [5].

In the following we first give a brief outline of the Hubbard's method and obtain an expression for the EMD,

$\rho(\vec{p})$, following Mijnders [2]. More details of the method

can be found in literature [1,2]. The results obtained by us by this method for Pd and Ag will be presented in the next chapter.

3.2 The Hubbard-Mijnarends Method:

In the KKRZ formulation, Ziman's determinantal equation giving the energy levels ϵ for the electron in state \vec{k} can be written as follows:

$$(\vec{k}_n^2 - \epsilon) B_n + \sum_{n'} \Gamma_{nn'} B_{n'} = 0 \quad (3.1)$$

In above $\vec{k}_n = \vec{k} + \vec{K}_n$, the \vec{K}_n being reciprocal lattice vectors; B_n are the coefficients of pseudo wavefunctions. The pseudo-potential matrix elements $\Gamma_{nn'}$ are given by,

$$\Gamma_{nn'} = \frac{4\pi}{\tau} \sum_l (2l+1) r_l^2 \gamma_l j_l(k_n r_l) j_l(k_{n'} r_l) P_l(\cos \theta_{nn'}) \quad (3.2)$$

where,

$$\gamma_l = - \frac{\tan \eta_l}{E' r_l^2 j_l(E' r_l) \{j_l(E' r_l) - (\tan \eta_l) n_l(E' r_l)\}} \quad (3.3)$$

Here τ is the volume of atomic polyhedron, $E' = \sqrt{E}$, $\eta_l(E)$ is the phase shift of the l -th partial wave scattered from atomic polyhedron (muffin-tin potential) at energy E , j_l and n_l are the spherical Bessel and Neumann functions respectively,

$\theta_{nn'}$ is the angle between \vec{k}_n and $\vec{k}_{n'}$, P_1 is the Legendre polynomial of order 1. One can choose r_1 arbitrarily in the interval $(0, r_i)$, r_i being the radius of the muffin-tin sphere.

In the case of the simple metals, $\tan \eta_1(E)$ is a smoothly varying function and is small. However, in the case of transition metals (i.e. d bands), $\tan \eta_2$ and hence also γ_2 passes through a narrow resonance at low energy.

In general γ_1 will be small, except near the resonance in $\tan \eta_2$. One can then write

$$\gamma_1 = \gamma_1' - \delta_1 \Gamma / (\epsilon_0 - E) \quad (3.4)$$

where Γ is the width of the resonance occurring for the partial wave $l = \lambda$ at $E = \epsilon_0$. Now γ_1' is always small, since the resonant part is subtracted out. We can rewrite (3.1) in the following form [1],

$$\begin{pmatrix} K + V - \epsilon I & h \\ h^* & (\epsilon_0 - \epsilon) I \end{pmatrix} \begin{pmatrix} B \\ a \end{pmatrix} = 0 \quad (3.5)$$

where the matrix elements of the submatrices are given by,

$$K_{nn'} = k_n^2 \delta_{nn'} \quad (3.6a)$$

$$V_{nn'} = \frac{4\pi}{r} \sum_l (2l+1) r_l^2 \gamma_l' j_l(k_n r_l) j_l(k_{n'} r_l) P_l(\cos \theta_{nn'}) \quad (3.6b)$$

$$h_{nm} = -4\pi r_\lambda \left(\frac{r}{\tau}\right)^{1/2} j_\lambda(k_n r_\lambda) Y_{\lambda m}(\vec{k}_n) \quad (3.6c)$$

and

$$a_m = \frac{4\pi r_\lambda}{\epsilon_0 - \epsilon} \left(\frac{r}{\tau}\right)^{1/2} \sum_n j_\lambda(k_n r_\lambda) Y_{\lambda m}^*(\vec{k}_n) B_n \quad (3.6d)$$

The matrix h is of the order $(2\lambda + 1)$; matrix B contains the non-resonant part and a the resonant part of the wavefunction.

The above equation (3.5) can be reduced to one with a lower order by separating the \vec{k}_n vectors in two sets, a preferred set P and the remainder R . Introducing the approximations $V_{PR} = V_{RP} = 0$ and neglecting V_{RR} with respect to $(k_n^2 - \epsilon)$ when \vec{k}_n belongs to the set R , one can get,

$$M(\epsilon) = \begin{pmatrix} K + V_{PP} - \epsilon I & h_P \\ h_P^* & A - \epsilon I \end{pmatrix} \begin{pmatrix} B_P \\ a \end{pmatrix} = 0 \quad (3.7)$$

and

$$(K_R - \epsilon I) B_R + h_R a = 0 \quad (3.8)$$

where

$$A_{mm'} = \epsilon_0 \delta_{mm'} - \frac{(4\pi)^2}{\tau} r_\lambda^2 \sum_n^{(R)} \left\{ \frac{j_\lambda^2(k_n r_\lambda)}{k_n^2 - \epsilon} Y_{\lambda m}(\vec{k}_n) Y_{\lambda m'}^*(\vec{k}_n) \right\} \quad (3.9)$$

and where the sum $\sum_n^{(R)}$ is over all the vectors of the

'remainder' set R . For the case of d-resonance the order of Eq. (3.7) is $(n_p + 5)$ where n_p is the number of preferred vectors.

The form of (3.7) is very similar to the one used in model pseudopotential schemes [6]. The submatrix V describes the nearly free electron (NFE) part of the conduction band (S-p) while the 5×5 submatrix A describes the d bands and the off-diagonal matrices h and h^* cause the hybridization between these bands. The submatrices A and V are energy dependent and the next step is to remove the energy dependence in the matrix M so that the problem is reduced to that of a diagonalization. This can be achieved by suitably approximating the energy dependence of A and V as follows,

$$M = \begin{pmatrix} K + V(k^2) & h \\ h^* & A(\epsilon_d) \end{pmatrix} \quad (3.10)$$

where ϵ_d is the mean d band energy.

A number of refinements of above approximations are suggested by Hubbard [1]. In essence the problem reduces to the solution of the secular equation,

$$(M - \epsilon I) \begin{pmatrix} B_p \\ a \end{pmatrix} = 0 \quad (3.11)$$

where B_p gives the non-resonant part of the wavefunction while A gives the resonant part. The remaining coefficients can be determined with the help of Eq. (3.8).

Lloyd [7] has shown that in the region outside the muffin-tin sphere (radius r_i) the wavefunction can be expanded in terms of plane waves having B_n as the plane wave coefficients.

$$\psi_{\vec{k}}(\vec{r}) = \frac{1}{(\tau)^{1/2}} \sum_n B_n e^{i(\vec{k} + \vec{k}_n) \cdot \vec{r}} \quad (3.12)$$

For $r < r_i$, i.e. within the inscribed sphere the wavefunction can be expanded in terms of spherical harmonics,

$$\psi_{\vec{k}}(\vec{r}) = \frac{4\pi}{(\tau)^{1/2}} \sum_L i^L \frac{R_L(r)}{R_L(r_i)} X_L Y_L(\vec{r}) \quad (3.13)$$

where the coefficients X_L (where $L \equiv l, m$) are determined by the continuity condition at $r = r_i$, i.e.

$$X_L = \sum_n B_n j_l(k_n r_i) Y_L^*(\vec{k}_n) \quad (3.14)$$

In practice only the first few l -values are retained in (3.13) and (3.14) and this truncation results in a slight discontinuity at $r = r_i$.

In the above we have sketched a bare outline of Hubbard's theory details of which can be found in the literature [1]. The next step now is to extend this method for calculation of electronic wavefunctions and momentum density.

In the independent particle model the electron momentum density is given by,

$$\rho(\vec{p}) = \sum_{j,k,i} f(\vec{k}, j) |A_j(\vec{k}, \vec{p})|^2 \delta(\vec{p} - \vec{k} - \vec{k}_i) \quad (3.15)$$

where $f(\vec{k}, j)$ is the Fermi-Dirac distribution function such that at $T = 0$ K, $f(\vec{k}, j) = 0$ if the state (\vec{k}, j) is unoccupied and $f(\vec{k}, j) = 1$ if the state is occupied. In (3.15) j is the band index while \vec{k}_i denotes the reciprocal lattice vector, where $A_j(\vec{k}, \vec{p})$ is the Fourier transform of the electron wavefunction, and is given by,

$$A_j(\vec{k}, \vec{p}) = \int_{\text{crystal}} e^{-i\vec{p} \cdot \vec{r}} \psi_{\vec{k}, j}(\vec{r}) d\vec{r} \quad (3.16)$$

The above expression can be simplified by using Eq. (3.12) and (3.13) for the electron wavefunction. Using these equations, Eq. (3.16) can be written as,

$$\begin{aligned} A_j(\vec{k}, \vec{p}) = & \sum_n B_n \delta(\vec{k}_n - \vec{p}) - \frac{4\pi r_i^2}{\tau} \frac{j_1(|\vec{k}_n - \vec{p}| r_i)}{|\vec{k}_n - \vec{p}|} \\ & + \frac{(4\pi)^2}{\tau} \sum_{l=0}^3 \sum_m X_{lm} \frac{1}{R_l(r_i)} \\ & \times Y_{lm}(\vec{p}) \int_0^{r_i} j_1(pr) R_l(r) r^2 dr \end{aligned} \quad (3.17)$$

Equations (3.15) and (3.17) form the basis of our computation of momentum distribution due to 4d (or 3d) and conduction

electrons. Contribution to the EMD from core electrons could be obtained by employing Eq. (2.4) and is already tabulated in the literature [8].

3.3 Computational Details:

The computational procedure followed by us was divided into following stages (Fig. 3.1).

a) Calculation of Phase Shifts and Radial Wavefunctions:

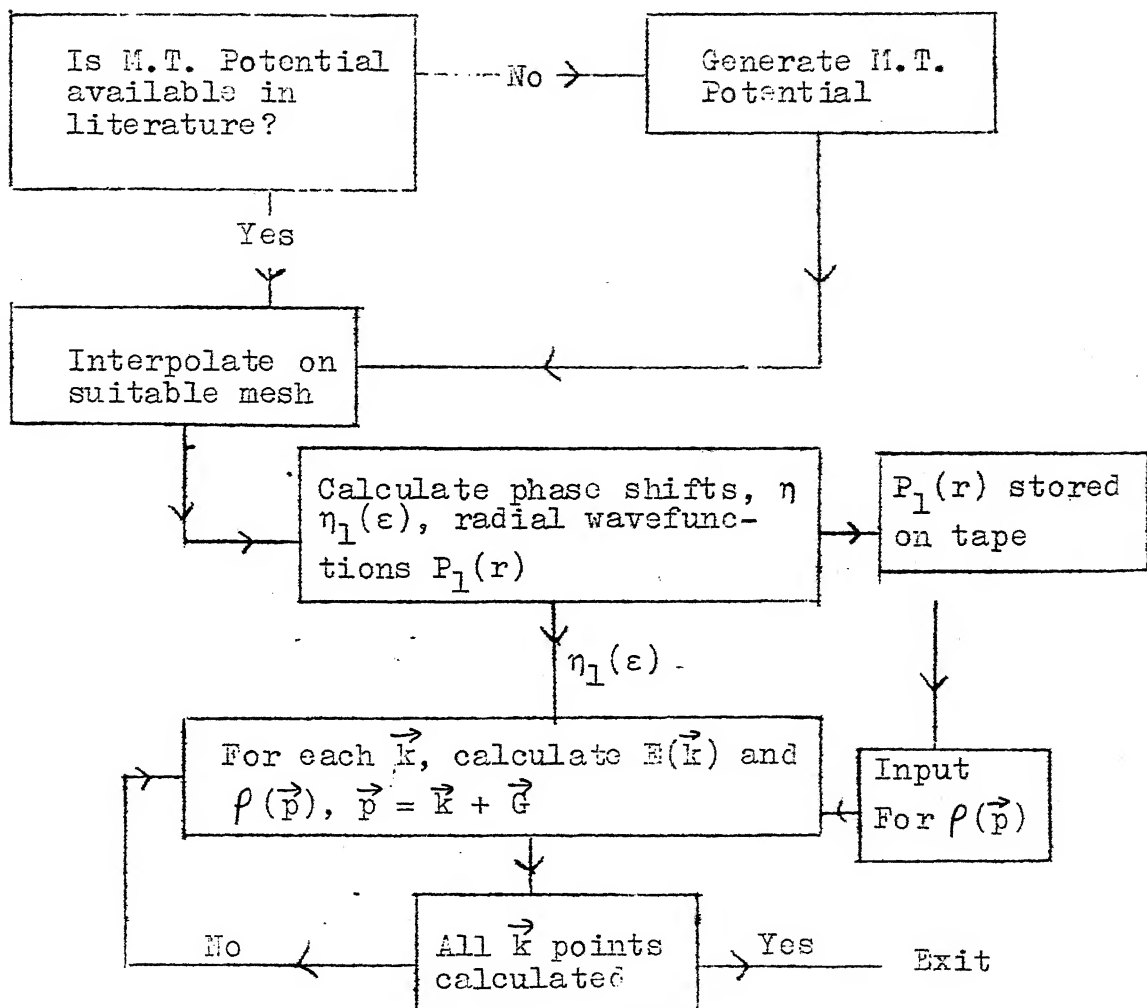
The starting point for the calculation of the phase shift is the muffin-tin potential [9.] interpolated on an appropriate Herman-Skillman mesh [10]. Employing the muffin-tin potential, phase shifts were calculated over entire energy range of interest at about 200 energy values with an interval of 0.01 Ry. (atomic units are used for other quantities). The radial part of the wavefunction was stored on a magnetic tape for further use. This stage of the calculation was independent of the crystal structure.

b) Calculation of Energy Eigenvalues (E_n), Wavefunctions (B_n and X_L coefficients) and Momentum Density $\rho(\vec{p})$:

Employing the phase shifts and radial wavefunction so obtained, we next calculated E_n , B_n , X_L and $\rho(\vec{p})$ (see Eq. (3.1) to (3.17)) for each selected \vec{k} -point. Partial waves upto $l_{\max} = 3$ were included in the expansion (3.13) of the wavefunction inside the inscribed sphere while 89 reciprocal lattice vectors were used in the expansion

Fig. 3.1

Flow diagram showing our computational procedure.



(3.12) outside the sphere. Mijnaresends [2] has reported a 3% increase in the $\rho(\vec{p})$ for Fe in the intermediate momentum region due to inclusion of $l = 3$ term. We have found that inclusion of 113 plane waves (instead of 89) had marginal effect on $\rho(\vec{p})$.

The accuracy of Hubbard's method has been discussed by Kaga [11] for the case of Pd and he has pointed out that the major errors in the energy values arise from the linear interpolations and extrapolations of the matrices $\hat{A}(\epsilon)$ and $\hat{V}(\epsilon)$ and from the small number of plane waves in the 'preferred set' P. We have studied [12] the effect of increasing the number of plane waves (in the P set) from 4 to 14 for Pd and Ag. Such an effect on energy values and momentum density $\rho(\vec{p})$ is shown in Tables 3.1 and 3.2 at some symmetry points. It can be seen that the energy levels of Pd near the Fermi energy (E_F) are fairly stable and are not affected significantly but energy values of the lower bands increase by as much as 0.03 Ry. bringing them in closer agreement with other results [13] as shown in Table 3.3. The effect of increasing the 'P' vectors is greater on $\rho(\vec{p})$, thus, for example at $(\vec{p} = 0, \rho(\vec{p}))$ decreases by as much as 20% while the energy eigenvalue at $\Gamma_{2,5}$ increases by 5% only. In the case of Ag (Table 3.4) we found that the maximum change in energy was of the order of 0.01 Ry. while the change in $\rho(\vec{p})$ at $\vec{p} = 0$ was only about 1%. In view of these observations we employed only 4 vectors

Table 3.1

Effect of the number of preferred vectors on the energy values of Pd. The first column gives \vec{k} vectors in units of $2\pi/a$ along with the BSW symbol. The second column specifies the number of preferred vectors, and the remaining columns give the energy values in Rydberg, for the lowest six bands.

\vec{k}	No. of p vectors	*ENERGY IN Ry.					
		1	2	3	4	5	6
Γ							
(0, 0, 0)	4	0.104	0.304	0.306	0.306	0.425	0.427
	14	0.101	0.319	0.320	0.320	0.427	0.427
X							
(0, 1, 0)	4	0.107	0.117	0.507	0.536	0.536	1.141
	14	0.131	0.161	0.505	0.533	0.536	0.855
K							
(0.75, 0.75, 0)	4	0.156	0.218	0.387	0.447	0.505	1.236
	14	0.179	0.220	0.389	0.446	0.503	1.105
L							
(0.5, 0.5, 0.5)	4	0.139	0.296	0.290	0.511	0.511	1.194
	14	0.159	0.301	0.312	0.510	0.511	0.652
U							
(0.25, 1.0, 0.25)	4	0.157	0.215	0.389	0.447	0.508	1.111
	14	0.180	0.227	0.390	0.443	0.504	1.106

* All values are with respect to the zero of the muffin tin potential which is at -0.85007 Ry.

Table 3.2

Effect of the number of preferred vectors on the momentum density $\rho(\vec{p})$ (for $\vec{p} = \vec{k}$) for Pd. n_p denotes the number of preferred vectors used.

$\vec{k} \backslash n_p$	Γ	X	K	L	U
4	0.912	0.197	0.255	0.193	0.280
14	0.865	0.175	0.248	0.174	0.267

Table 3.4

Effect of the number of preferred vectors on energy values of Ag. All other quantities in the table are similar to that for Table 3.1. The last column marked ρ_{tot} , gives the values of $\rho(\vec{p})$ for the two cases, where $\vec{p} = \vec{k}$.

\vec{k}	No. of 'p' vectors	ENERGY IN Ry.						ρ_{tot}
		1	2	3	4	5	6	
Γ								
(0, 0, 0)	4	-0.025	0.042	0.043	0.043	0.111	0.112	0.817
	14	-0.025	0.048	0.048	0.048	0.111	0.112	0.821
X								
(0, 1, 0)	4	-0.067	-0.065	0.160	0.176	0.176	0.645	0.141
	14	-0.057	-0.047	0.159	0.176	0.176	0.645	0.131
K								
(0.75, 0.75, 0)	4	-0.038	0.000	0.101	0.127	0.159	0.818	0.171
	14	-0.029	0.000	0.101	0.126	0.157	0.817	0.171
L								
(0.5, 0.5, 0.5)	4	-0.042	0.039	0.039	0.162	0.162	0.477	0.581
	14	-0.037	0.045	0.045	0.162	0.162	0.477	0.581
Σ								
(0.375, 0.375, 0)	4	0.023	0.037	0.085	0.089	0.089	0.262	0.791
	14	0.024	0.040	0.081	0.086	0.089	0.260	0.789

Table 3.5

Some parameters used in the calculations.

	Pd [14]	Ag [15]
a, lattice constant (a.u.)	7.3530	7.7112
Constant potential between the spheres, to be taken as Muffin-Tin zero (Ry.)	-0.85007	-1.1183
E_F , Fermi energy with respect to the zero of the Muffin-Tin potential (Ry.)	0.5246	0.518
r_i , Muffin-Tin radius (a.u.)	2.59968	2.726
ϵ_d^* , the mean d band energy (the energy at which $\tan \eta_2$ goes through a resonance)	0.335	0.070

* The values quoted are from our calculations.

Table 3.6

The preferred vectors (in units of $2\pi/a$) used in the calculations for Pd (14). In the case of Ag only first four vectors are used.

\vec{k}	:	1	(0, 0, 0)
		2	(-1, -1, -1)
		3	(0, -2, 0)
		4	(-1, -1, 1)
		5	(1, 1, 1)
		6	(1, 1, -1)
		7	(1, -1, 1)
		8	(1, -1, -1)
		9	(-1, 1, 1)
		10	(-1, 1, -1)
		11	(2, 0, 0)
		12	(-2, 0, 0)
		13	(0, 2, 0)
		14	(0, 0, 2)

in the 'P' set for Ag (thus saving computational time) while 14 vectors were used for Pd. Other numerical data about the parameters employed in our calculations are given in Table 3.5, while Table 3.6 lists the set of preferred vectors used by us. About 90 \vec{k} -points in $1/48$ of the Brillouin Zone (in the (100) and (110) planes) were used to calculate the energy eigenvalues. Employing suitable K-vectors, $\rho(\vec{p})$ was calculated for about 800 p-points in the above symmetry planes. Typical computer time taken to calculate JMD at one k-point (along with its U-processes) was about 2.0 minutes on the IBM 7044 Computer of the Indian Institute of Technology, Kanpur.

The results of our calculations for Pd and Ag are discussed in the next chapter.

REFERENCES

1. J. Hubbard, J. Phys. C 2, 1222 (1969). Also see: J. Hubbard, Proc. Phys. Soc. Lond. 92, 921 (1967); J. Hubbard and N.W.D. Dalton, J. Phys. C (Proc. Phys. Soc.) 2, 1, 1637. (1968). J. Hubbard and P.E. Mijnders, J. Phys. C 5, 2323 (1972).
2. P.E. Mijnders, Physica 63, 235 (1973).
3. R.M. Singru, Pramana 2, 299 (1974).
4. P.E. Mijnders, Physica 63, 243 (1973).
5. R.M. Singru and P.E. Mijnders, Phys. Rev. B9, 2372 (1974).
6. V. Heine, Phys. Rev. 153, 673 (1967); L. Hodges, H. Ehrenrich and N.D. Lang, Phys. Rev. 152, 505 (1966); D.G. Pettifor, J. Phys. C 5, 97 (1972).
7. P. Lloyd, Proc. Phys. Soc. Lond. 86, 825 (1965).
8. A. Harvey and R.J. Weiss, IBM J. Res. 9, 2 (1965).
9. Details of this are described in the next chapter.
10. F. Herman and S. Skillman, Atomic Structure Calculations, (Prentice-Hall: Englewood Cliffs, New Jersey, 1963).
11. H. Kaga, Phys. Letts 37A, 373 (1971).
12. We are grateful to R. Harthoorn for pointing out this effect.
13. F.M. Mueller, A.J. Freeman, J.O. Dimmock and A.M. Furdyna, Phys. Rev. B1, 4617 (1970).
14. K.C. Wong, ICTP, Preprint, IC/72/42 (1972).
15. S. Bhatnagar, Phys. Rev. 183, 657 (1969).

Chapter 4

ELECTRON MOMENTUM DENSITY IN Pd* AND Ag

4.1 Introduction:

In this chapter we present our results for the band structure and EMD for Pd and Ag and discuss their important features. Our results for the energy bands and Fermi surface are presented and compared with other theoretical results in Sec. 4.2 while the results for total EMD as well as the band-by-band contributions to the total EMD are discussed in Sec. 4.3. In the Sec. 4.4 the EMD of Pd and Ag are compared with that of Ni and Cu.

4.2 Energy Bands and Fermi Surface of Pd and Ag:

Our results for the band structure for Pd and Ag along important symmetry directions are shown in Fig. 4.1 and 4.2 respectively. For Pd, we have employed the muffin-tin potential which was constructed by Wong [1] using a non-relativistic free-atom HFS wavefunctions for a $4d^{10}5s^0$ configuration. The agreement between our results (Fig. 4.1)

* Preliminary results of our calculations for Pd are published in the paper: D.G. Kanhere and R.M. Singru, Phys. Letts. 53A, 67 (1975).

and those of Wong [1] is good. A detailed study of the electronic structure of Pd is made by Mueller et al. [2]. These authors have employed an APW method, as well as a combined interpolation scheme, and have included relativistic effects also. Krogh-Anderson [3] and Tewari [4] have also calculated the band structure of Pd. Our calculated eigenvalues for some symmetry points for Pd are compared with those of Mueller et al. [2] in Table 4.1. In general the agreement of our results with other results [1,2] is good. The width of the d band ($X_5 - X_1$) observed by us is closer to the results of Mueller et al. [2]. The cross sections of the Fermi surface for Pd by the (100) and (110) plane are shown in Fig. 4.3. The Fermi surface of Pd consists of (i) a Γ -centered sixth band electron sheet which displays large distortions. This sheet is primarily d-like, (ii) X-centered hole sheet formed from the fifth-band electrons giving rise to an open network in the extended zone, (iii) small hole pockets around X. Above features of the Fermi surface (Fig. 4.3) agree qualitatively with other calculations [2-4] and experimental results [5,6]. A L-centered fifth band hole pocket found by Mueller et al. [2] is not yet observed experimentally and is absent in our results. This difference could perhaps come from the relativistic effects.

Band structure of Ag has been calculated by Bhatnagar employing APW method, by Snow [8] employing self-consistent

Table 4.1

Comparison of some important band widths for Pd, obtained by us with others. All the energy values are in Rydbergs.

		Present work	Mueller et.al [2]
Width of the (sp) band	$X_4' - \Gamma_1$	0.754	0.751
Width of the d'band	$X_5 - X_1$	0.404	0.396
Separation	$X_4' - X_5$	0.310	0.308
Distance of E_F to upper most 'd' level	$X_5 - E_F$	0.017	0.018

Table 4.2

Comparison of some important bandwidths for Ag.
Energy values are in Rydbergs.

		Present work	Bhatna- gar [7]	Rijsenbrij and Fondse [9]
Width of the (sp) band	$X_4' - \Gamma_1$	0.670	0.652	0.688
Width of the 'd' band	$X_5 - X_1$	0.243	0.240	0.251
Separation	$X_4' - X_5$	0.469	0.457	0.442
Distance of E_F to upper most 'd' level	$E_F - X_5$	0.332	0.322	0.292

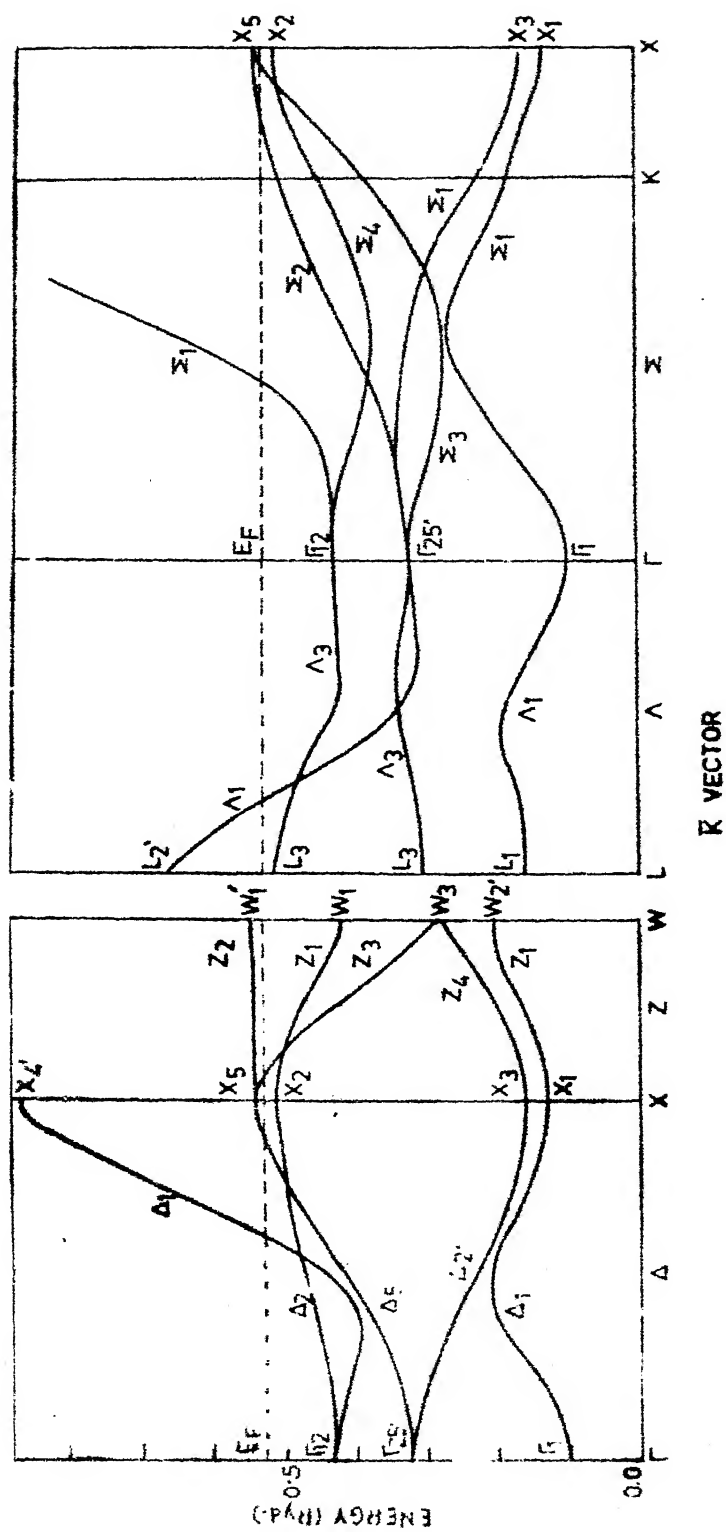


FIG. 4.1: Energy bands of Id along some symmetry directions.

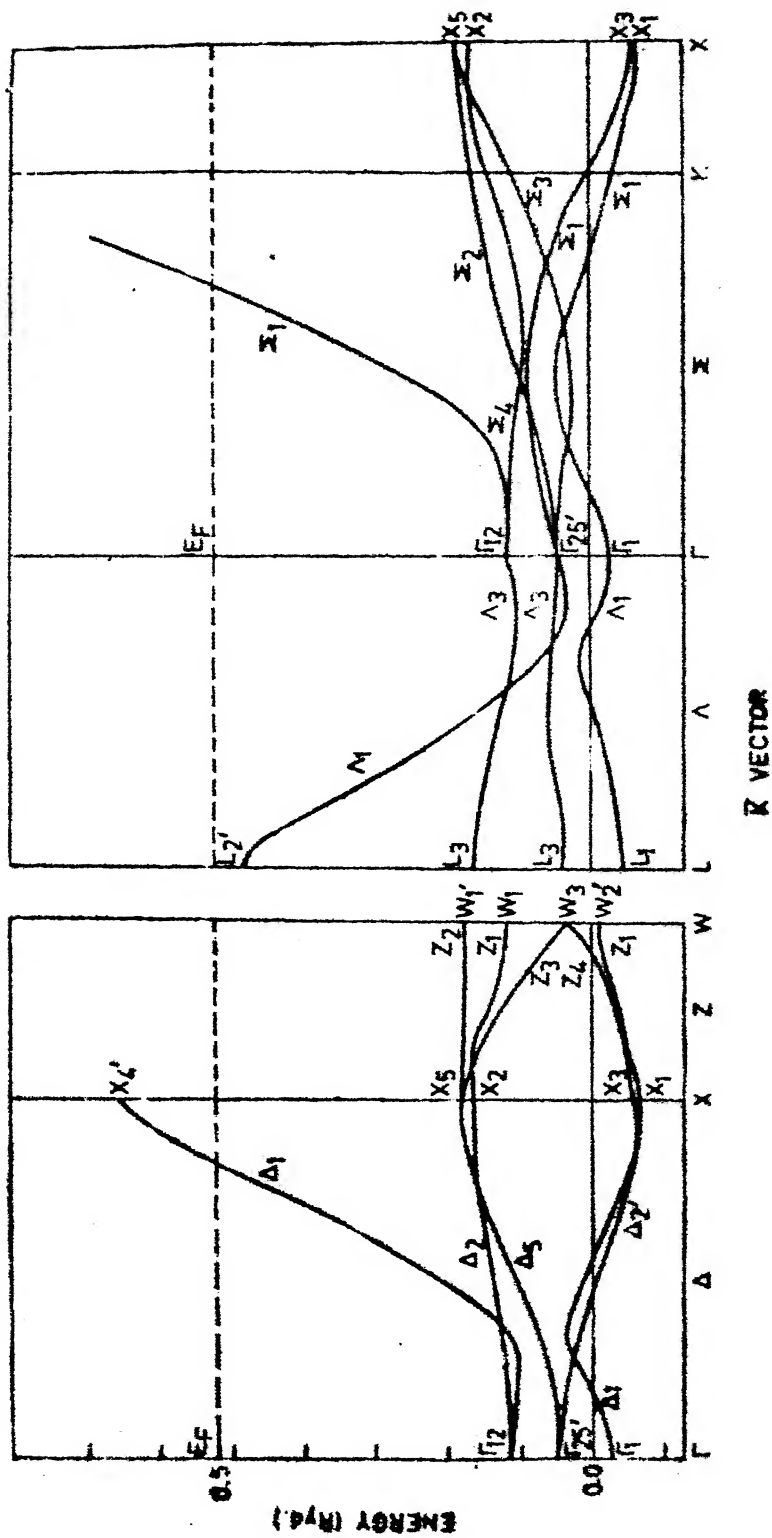
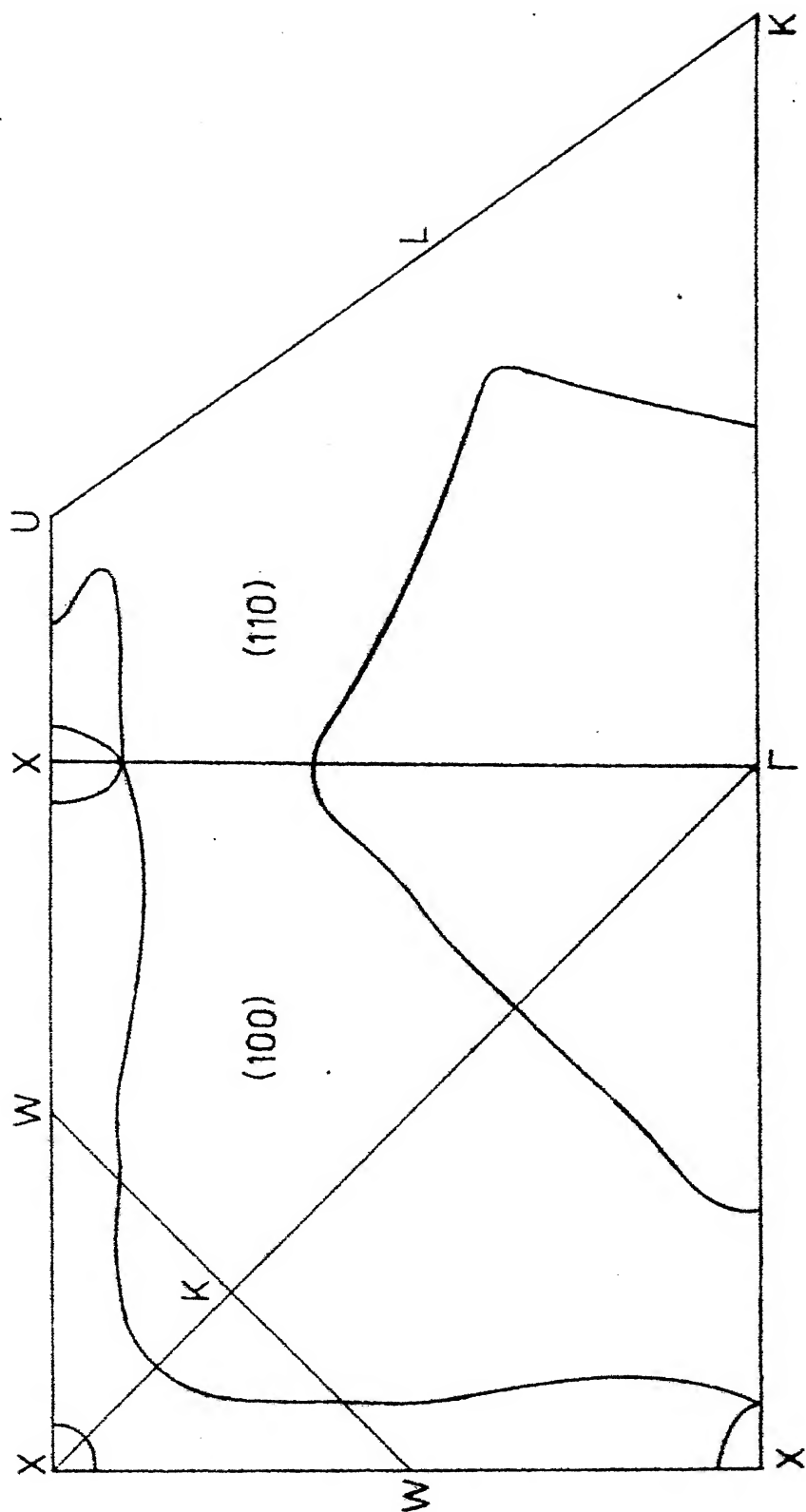
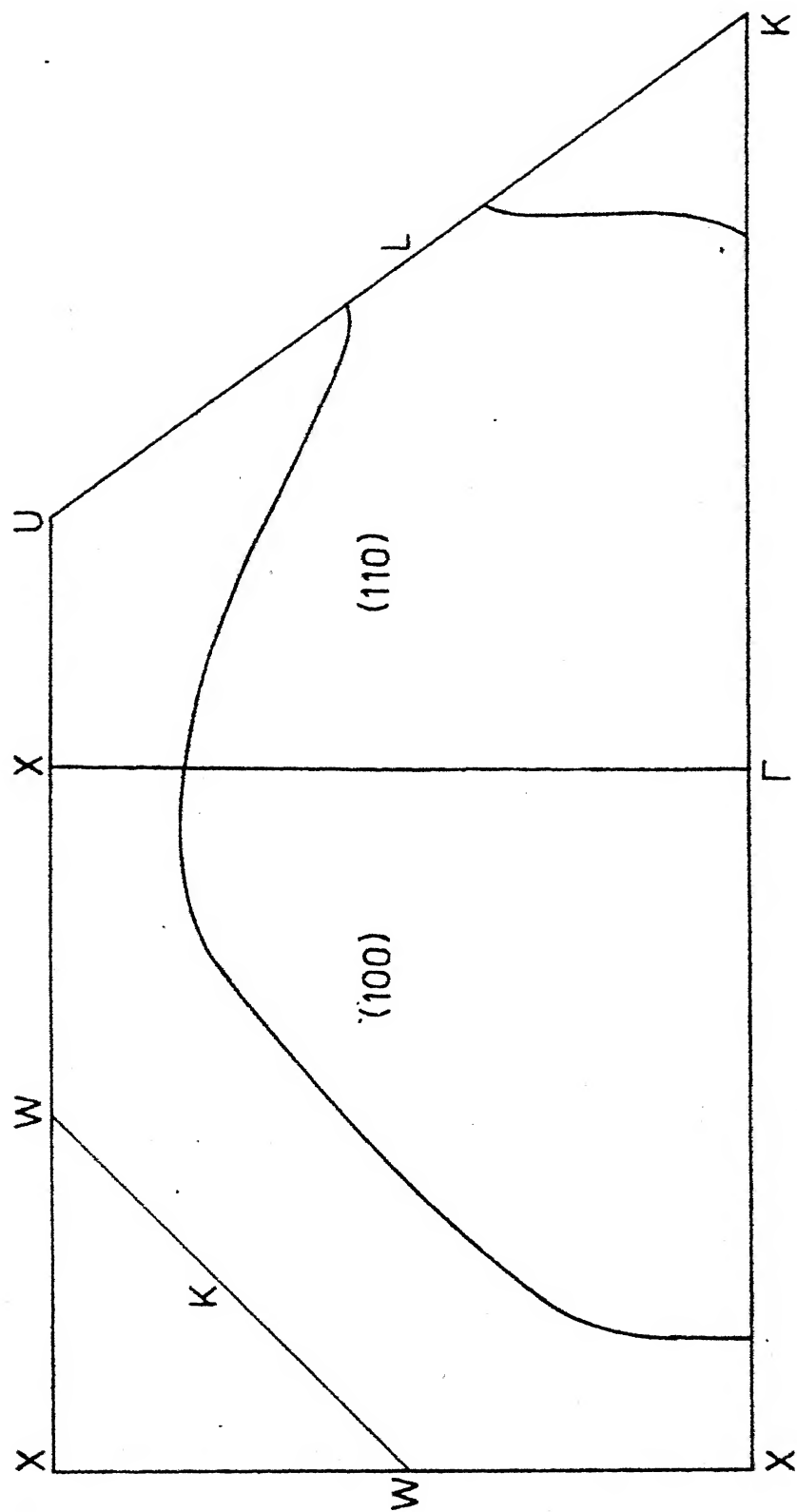


Fig. 4.2: Energy bands of Ag along some symmetry directions.



Fermi Surface of Palladium

Fig. 4.3: Sections of the Fermi surface of Pd by (100) and (110) planes.



Fermi Surface of Silver

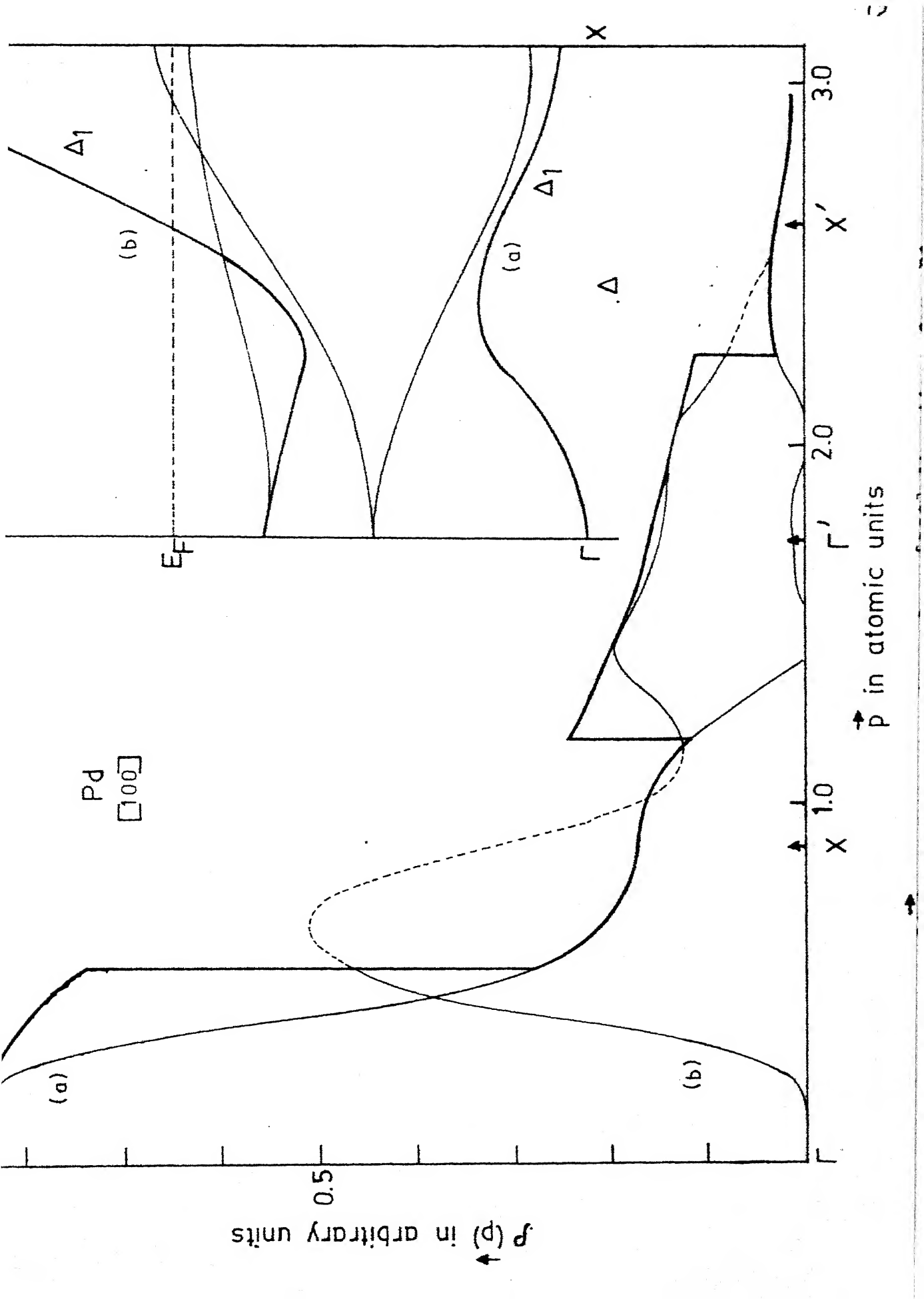
Fig. 4.4: Sections of the Fermi surface of Ag by (100) and (110) planes.

APW method, by Rijsenbrij [9] employing non-relativistic KKR method and by Christensen [10] by relativistic APW method. We employed the muffin-tin potential for Ag constructed by Bhatnagar [7]. A comparison of our results with other calculations is shown in Table 4.2 and it shows an overall satisfactory agreement. Fermi surface of Ag (Fig. 4.4) shows features common to other noble metals (viz. Cu and Au) in that it is in contact with the zone face at L giving rise to a neck along eight $[111]$ directions [11].

4.3 Electron Momentum Distribution for Pd and Ag:

The results of our EMD calculations for 4d and conduction electrons in Pd and Ag are presented in Fig. 4.5 to 4.24. The EMD for Pd along the important symmetry directions Δ (100), Σ (110) and Λ (111) is shown in Figs. 4.5 - 4.7. These curves show the total EMD as well as the band-by-band EMD with the relevant band structure shown in the inset. The labels a, b, ... correspond to the particular band which contributes to the EMD while the dashed part of the curve indicates the contribution from the unoccupied bands. The results for Ag are shown in Figs. 4.8 - 4.10 in a similar manner.

The curves describing total EMD show significant structure (i.e. valleys, steps etc.) which can be attributed to the sixth band electron Fermi surface and its reflections



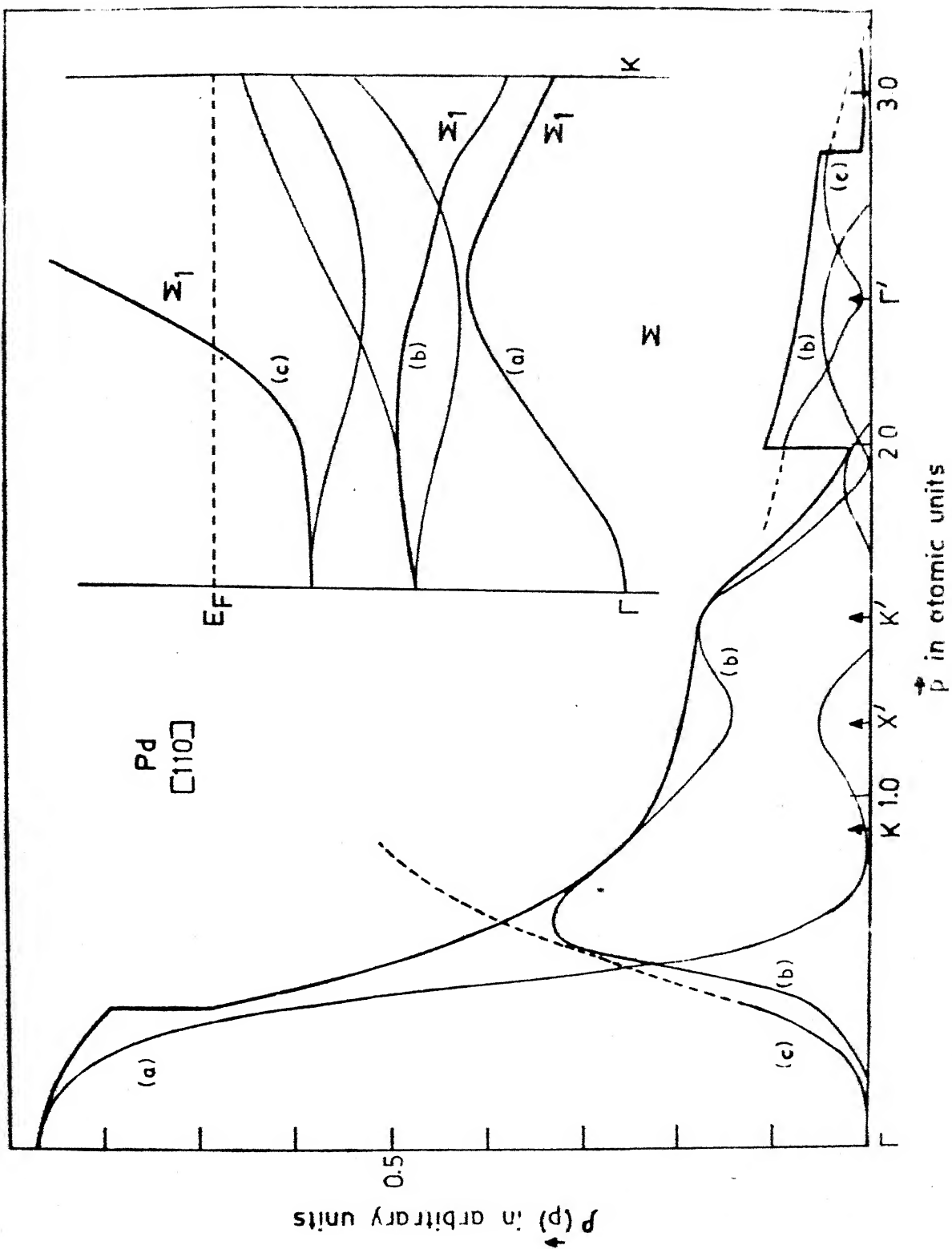


Fig. 4. Fermi surface map and Fermi level plot for Pd [110].

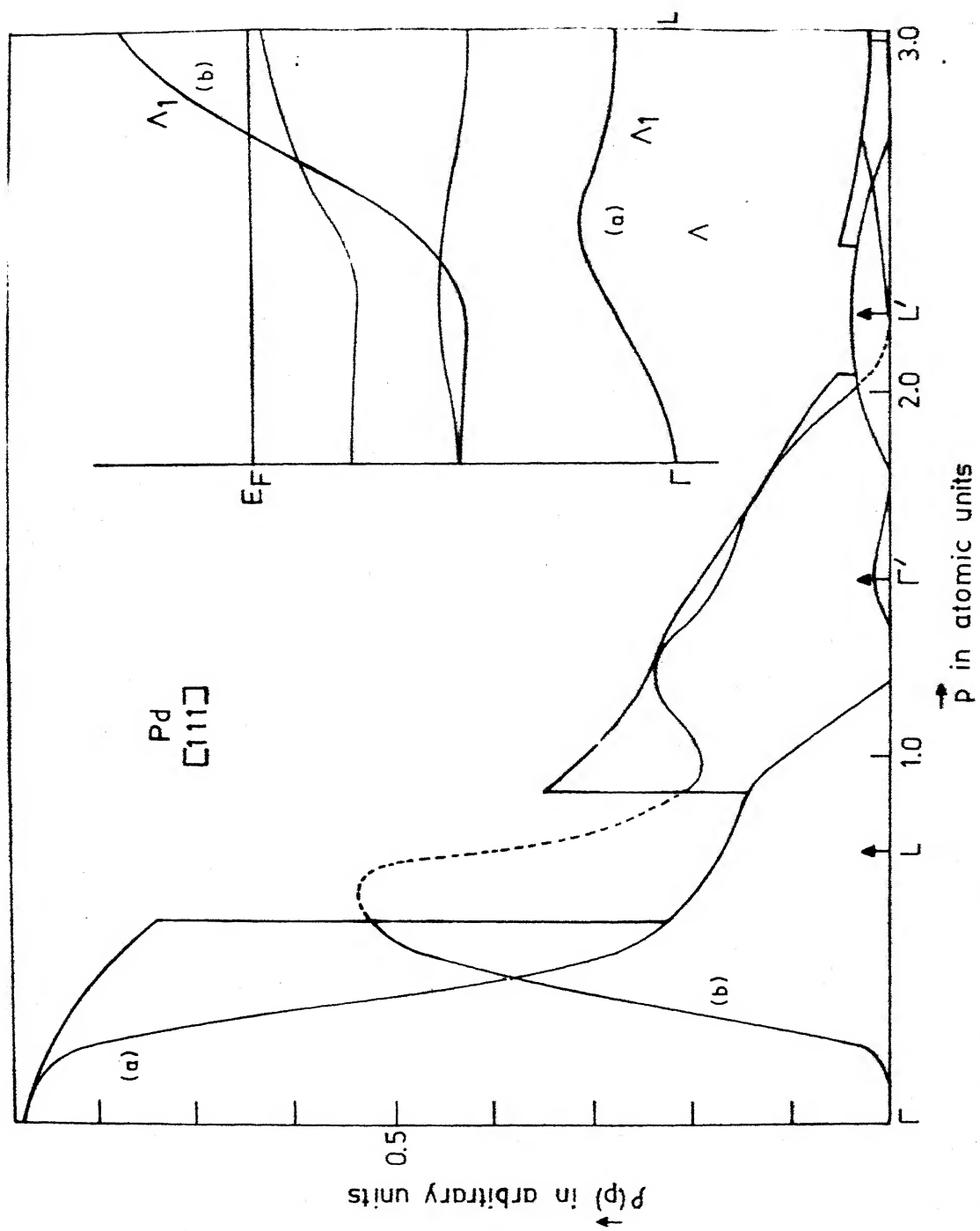


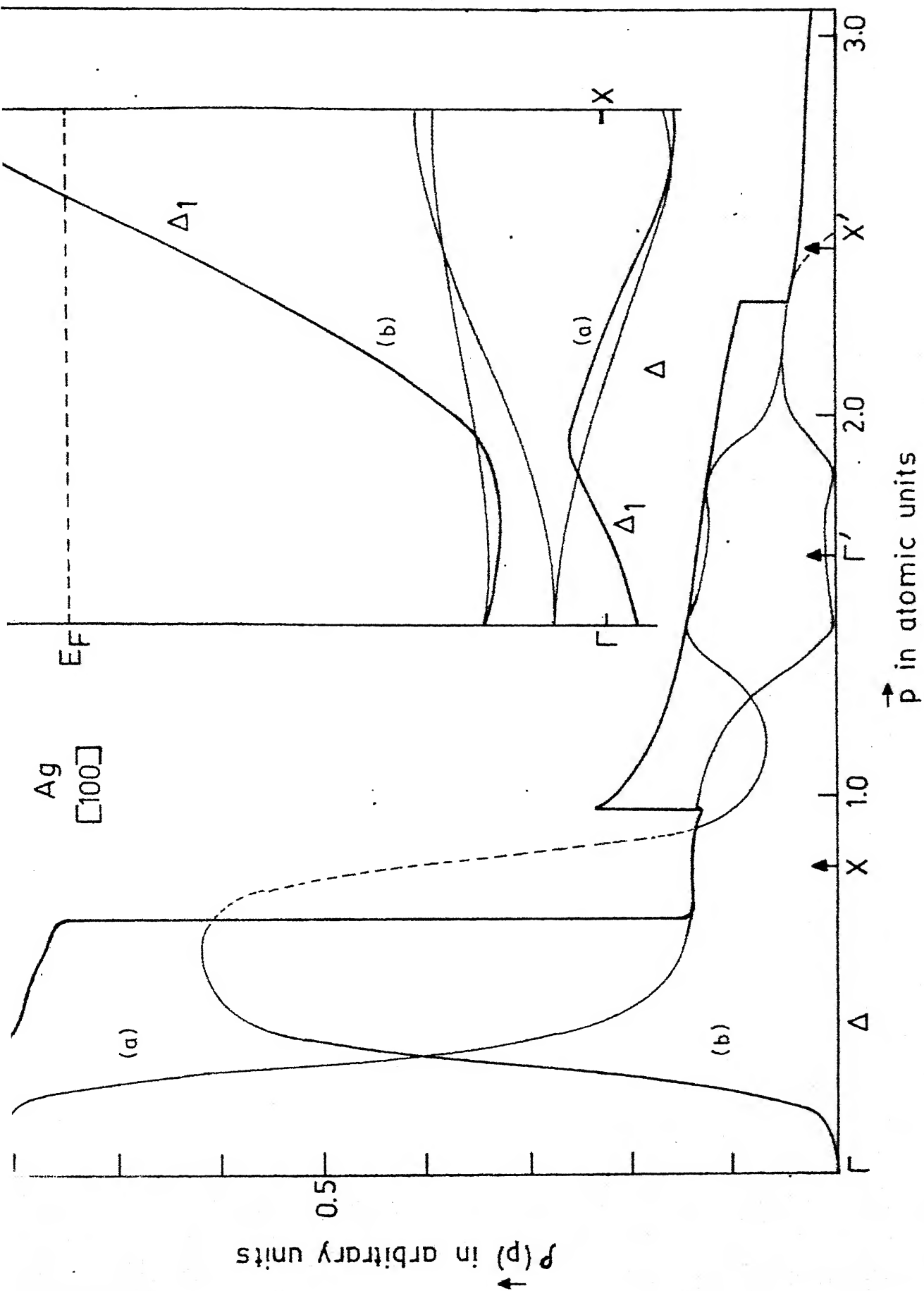
Fig. 4.7: $P(\vec{p})$ and band structure along $[111]$ direction for Pd.

in higher zones (through Umklapp processes). In particular prominent steps are observed for Pd along Δ and Λ directions. A smaller step is seen along the Σ direction and it can be explained as follows. The hybridized Σ_1 band (marked as 'c' in Fig. 4.6) crosses the Fermi level at a smaller k-value and its wavefunction retains the original d character at the Fermi level. The contribution of this band goes as p^4 and hence has smaller value at the Fermi level. The EMD in Pd shows strong momentum dependence and this can be ascribed to the s-d hybridization. If we examine the contribution to the EMD by individual bands, we notice that only the Δ_1 , Σ_1 and Λ_1 bands alone contribute. This is a result of a selection rule arising from a full symmetry possessed by $\rho(\vec{p})$, as pointed out by Mijnenends [12].

The effect of sp-d hybridization on EMD is shown by the individual bands but the net effect of hybridization on the total EMD is small. The contribution of the lowest Δ_1 , Σ_1 and Λ_1 bands (marked 'a' in Figs. 4.5-4.7) falls off as k increases because the bands hybridize with the higher bands. The contribution due to the higher Λ_1 and Δ_1 bands (marked 'b' in Figs. 4.5-4.7) varies initially as p^4 (as expected for a d band) but rises faster due to the mixing of s-character. Along the Σ direction, there are two higher Σ_1 bands (marked 'b' and 'c' in Fig. 4.6) and among these the 'b' band is d-like throughout the zone while 'c'

hybridizes with 'a' strongly and their respective EMD show this character. A prominent feature of all the EMD curves is the significant value of $\rho(\vec{p})$ at high momenta (HMC) which is contributed by the d-like states via the Umklapp processes. However, the momentum dependence in the region $p = 1.0 - 2.5$ a.u. along Σ direction is significantly different from that along Δ and Λ directions. This behaviour of EMD is expected to manifest itself in the anisotropy of directional CP.

The behaviour of the EMD in Ag along the three symmetry directions (Figs. 4.8 - 4.10) can be understood in a manner similar to Pd. The overall features of the EMD in Ag show similarity with that of Cu [12] as expected. As compared to Pd, Ag has narrower d bands which lie well below the Fermi level. As a result the states in Ag near Fermi level are almost completely hybridized and possess a dominant p character. These features of the bands are reflected in the sharper (as compared to Pd) steps, especially along the Σ direction in the first zone and relatively smaller steps in higher zones. The nearly-free electron (NFE) character of the EMD in Ag is shown by its flat behaviour in the first zone. Remembering that the 4d band is completely full in Ag, this result is not unexpected. The effect of the neck in the Fermi surface of Ag manifests



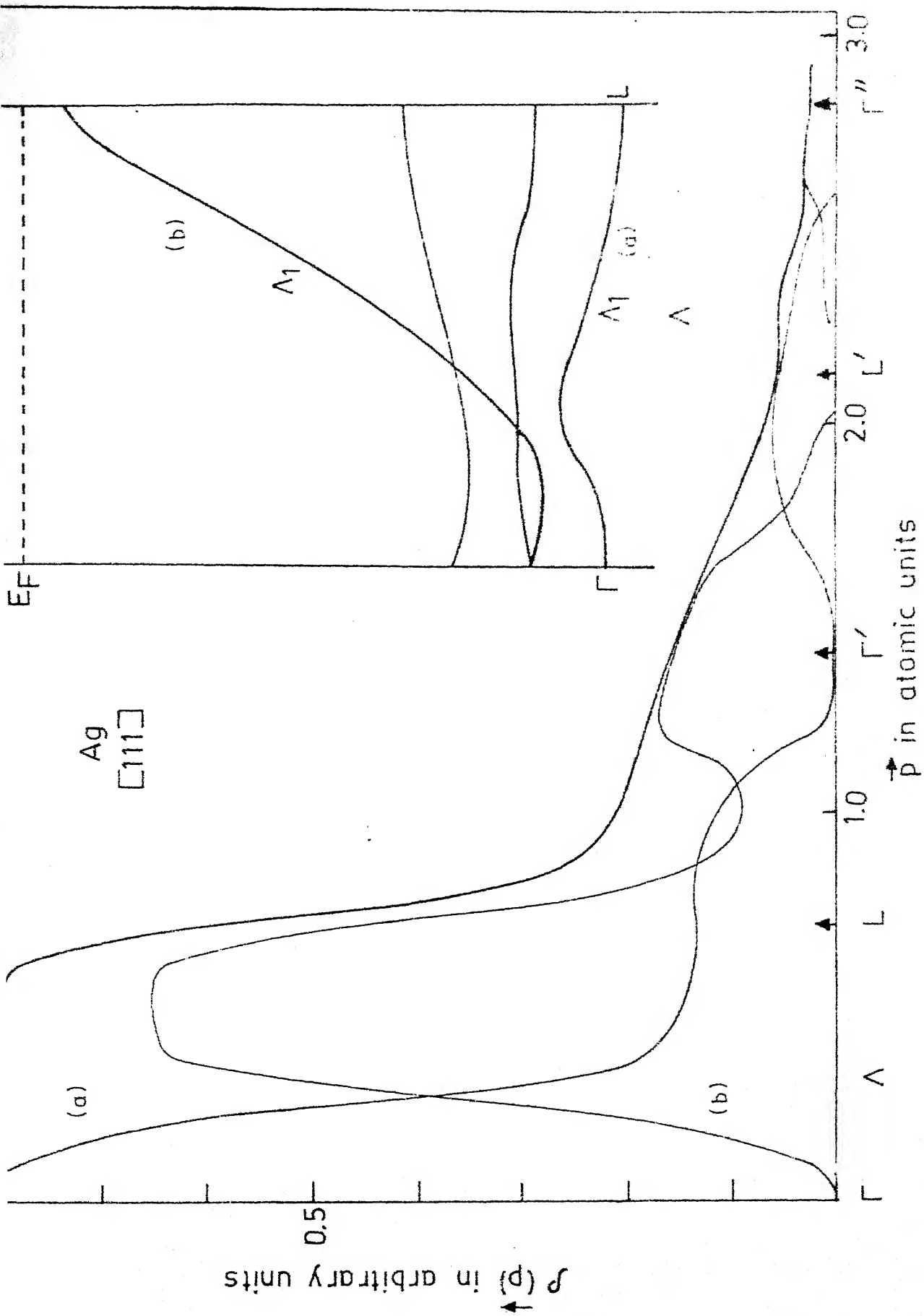
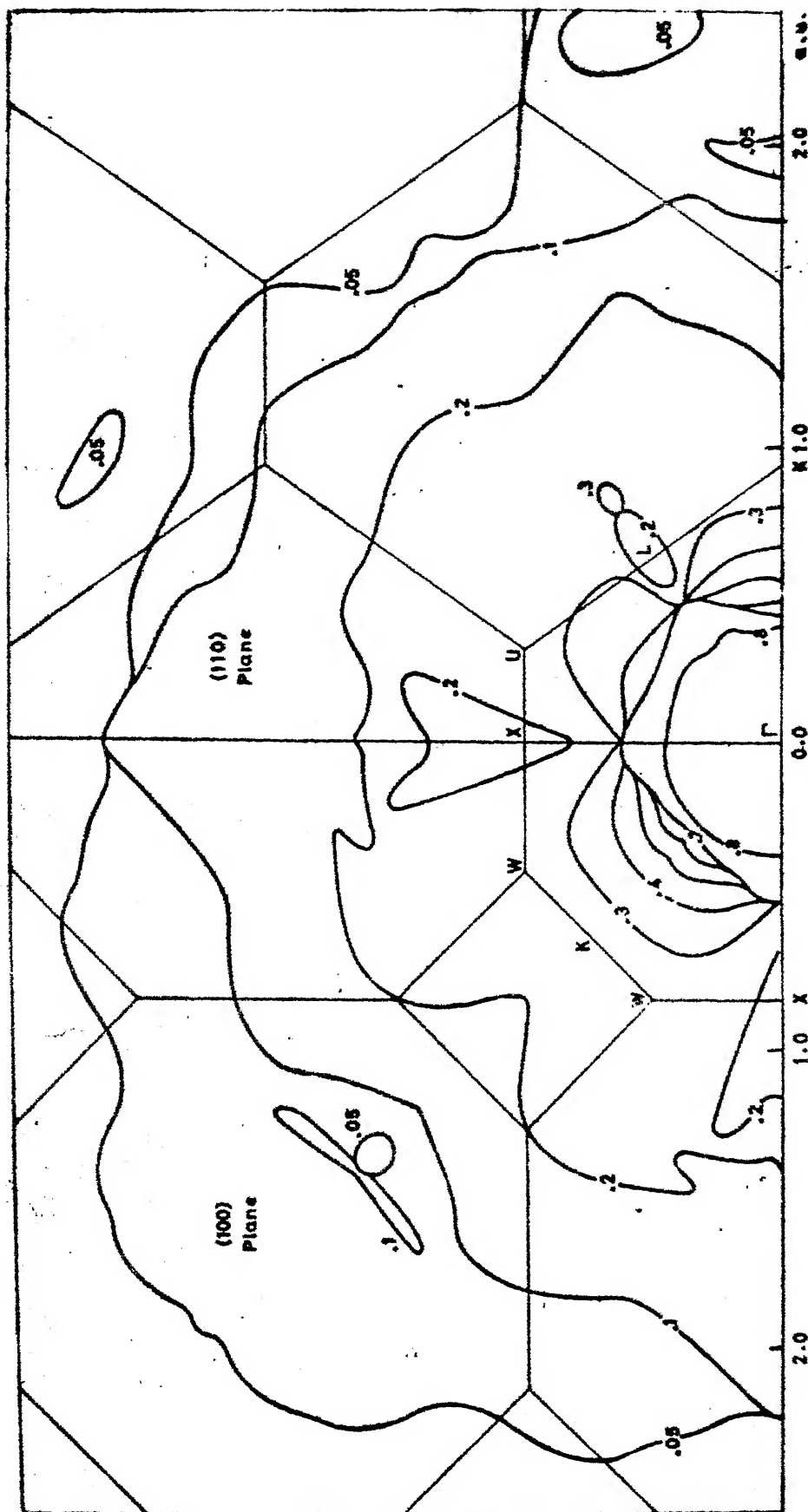


Fig. 4.10: $\rho(\vec{p})$ and band structure along $[111]$ direction for Ag.

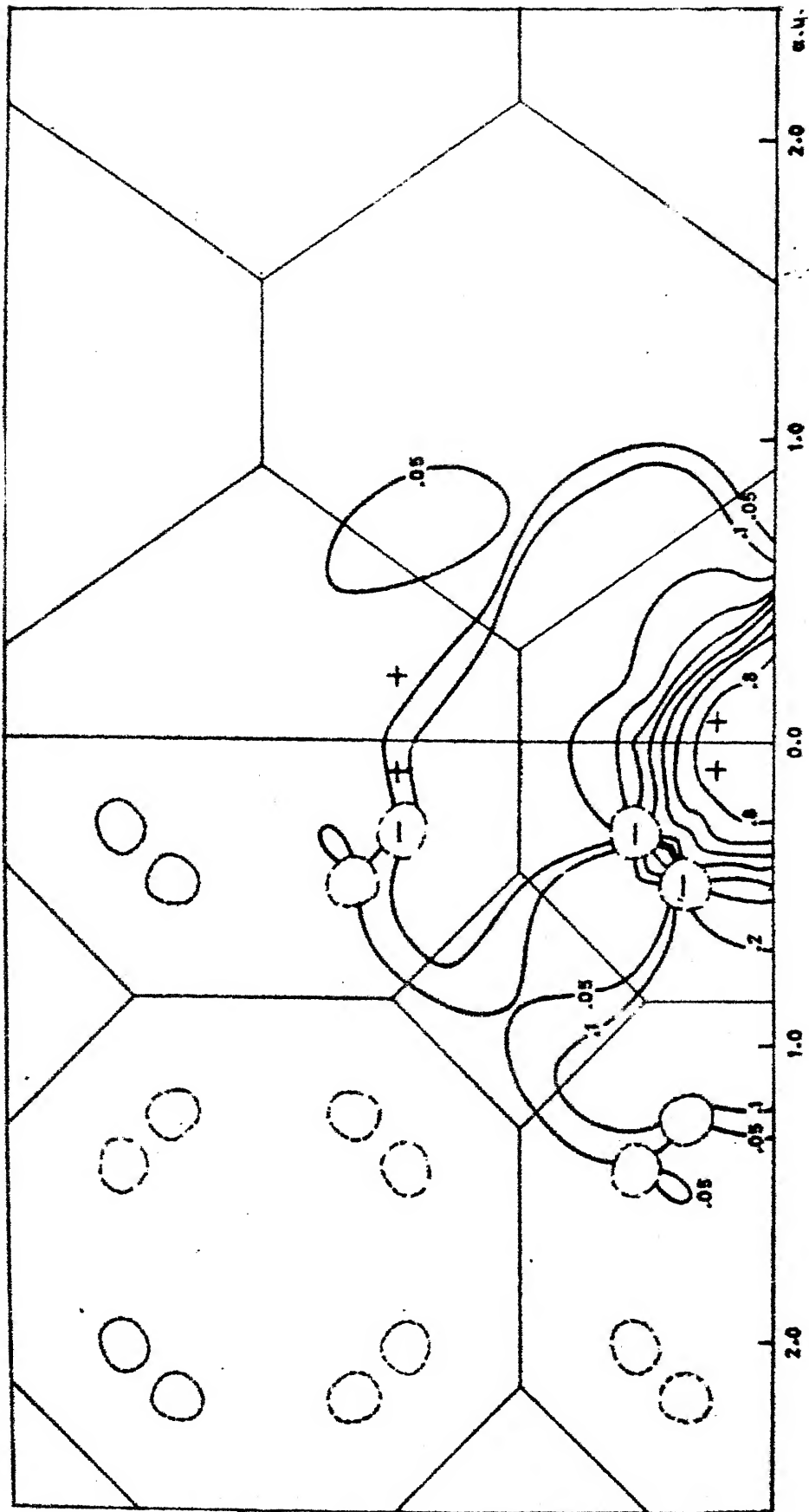
itself in the smooth behaviour of the EMD along the Λ direction, although the slope of EMD at the zone face is considerably large. The half-width of the EMD contributed by the lowest bands (marked 'a') are smaller in Ag than in Pd. This difference may be due to the smaller degree of hybridization in Ag. The EMD curves for Ag show less anisotropy in the region $p < 1$ a.u. when compared to Pd.

A deeper insight in the EMD is obtained if it is plotted as a contour-wise diagram in a plane. Such plots are especially useful to study the effects due to (i) small changes in band structure near the Fermi level or (ii) changes in the Fermi level itself due to alloying, which can be analyzed in the framework of rigid band model. We have, therefore, plotted the isodensities for Pd and Ag in the planes (100) and (110) in Figs. 4.11 - 4.24. The plots of total EMD contours are followed by the plots of EMD due to individual bands 1, 2, ..., 6, the numbering of the bands being done according to increasing energy (Fig. 4.1 and 4.2). The dotted curves (Figs. 4.11 to 4.24) represent the lines along which the bands touch. A transfer of EMD takes place across these lines as the symmetric (+ or -) character of the band changes. As a result of the selection rule [12] discussed above only the bands with (+) symmetry can contribute to the EMD. In Figs. 4.15, 4.16, 4.17 and 4.24 we have also shown the Fermi surface by indicating the unoccupied region by



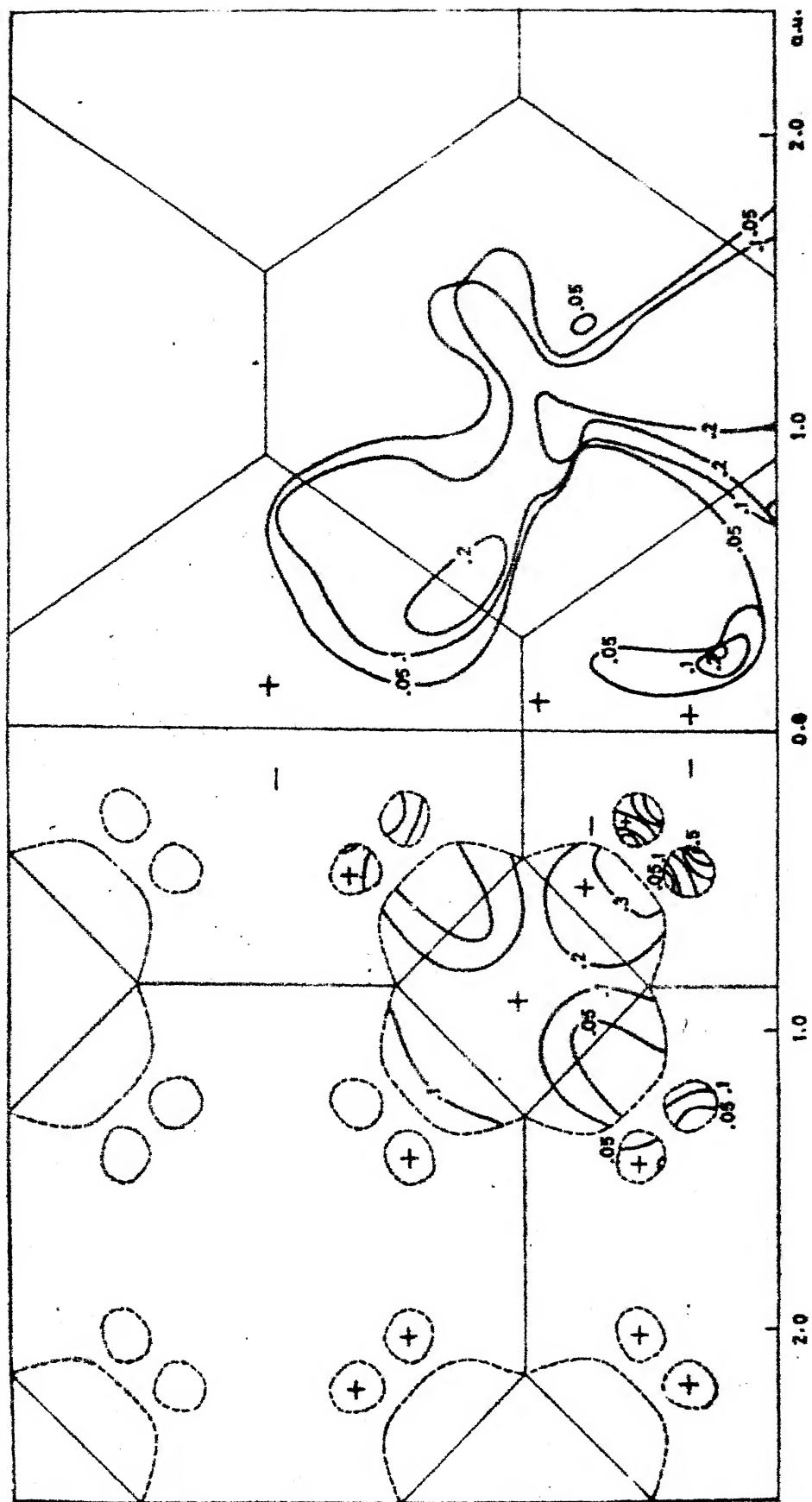
Pd: Total

FIG. 4.11: Pd: Total



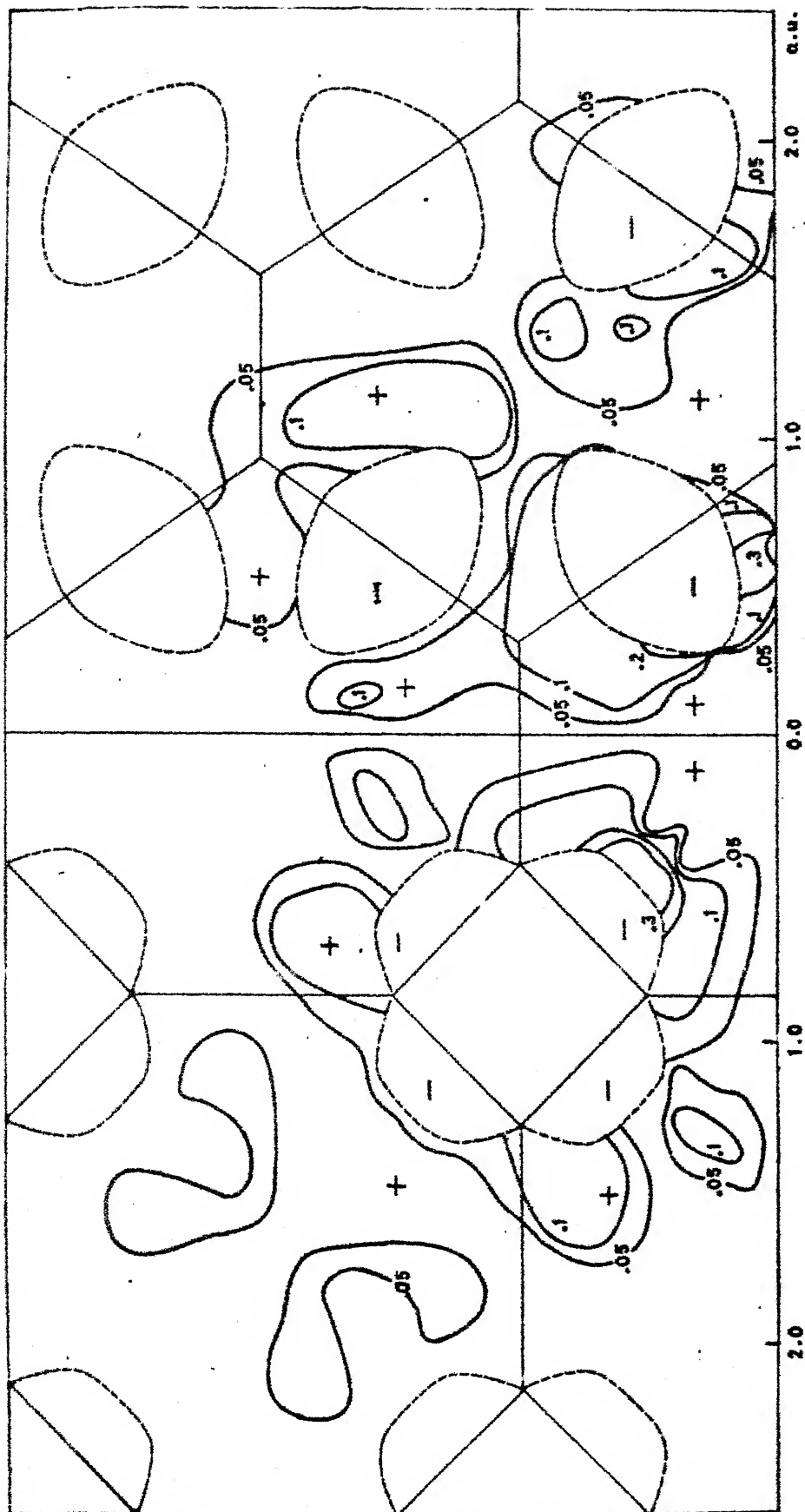
Pd: Band 1

Fig. 4.12: 4D isodensities for Pd: Band 1.



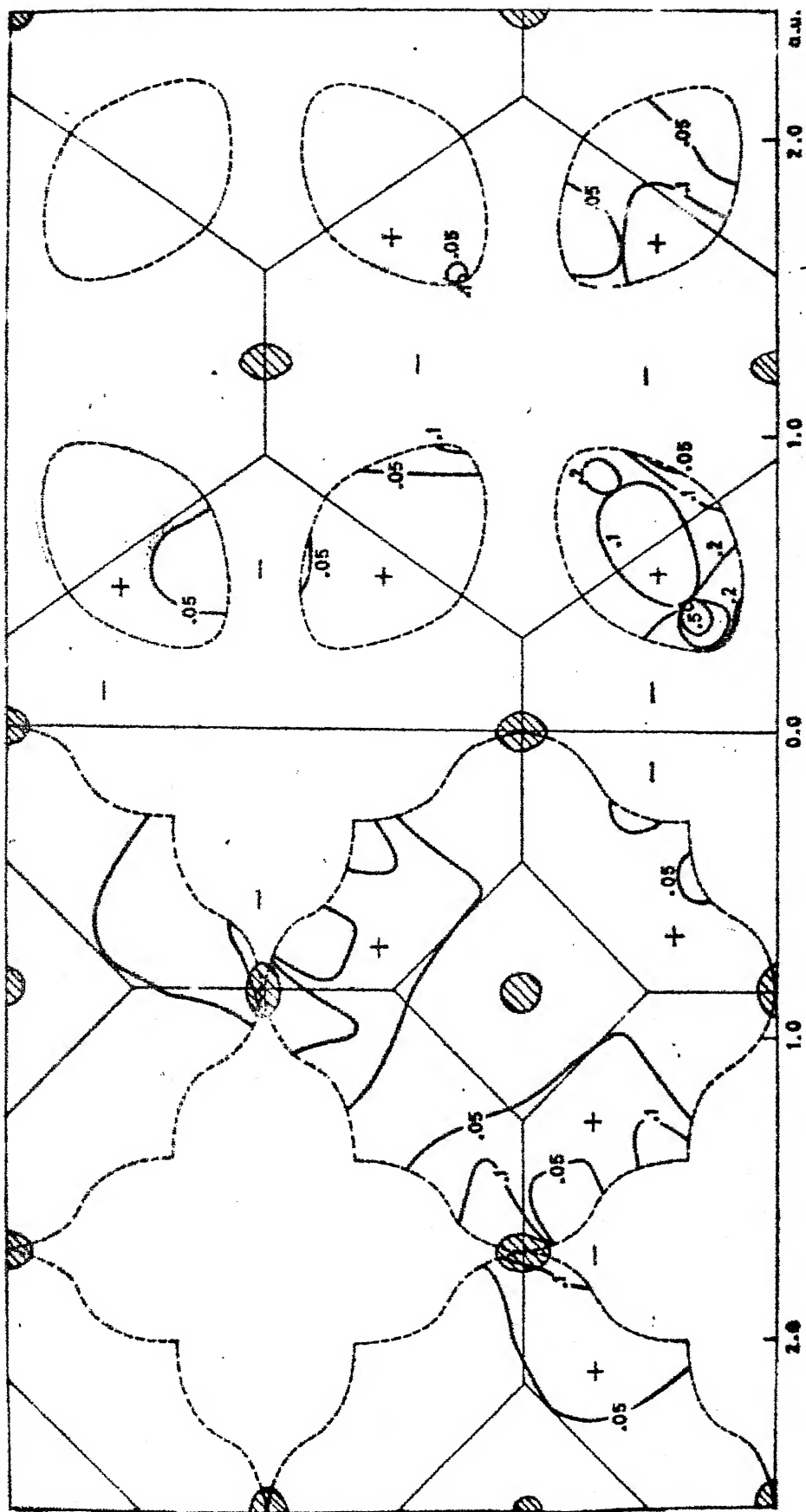
Pd: Band 2

Fig. 4.12: EMD isodensities for Pd; Band 2.



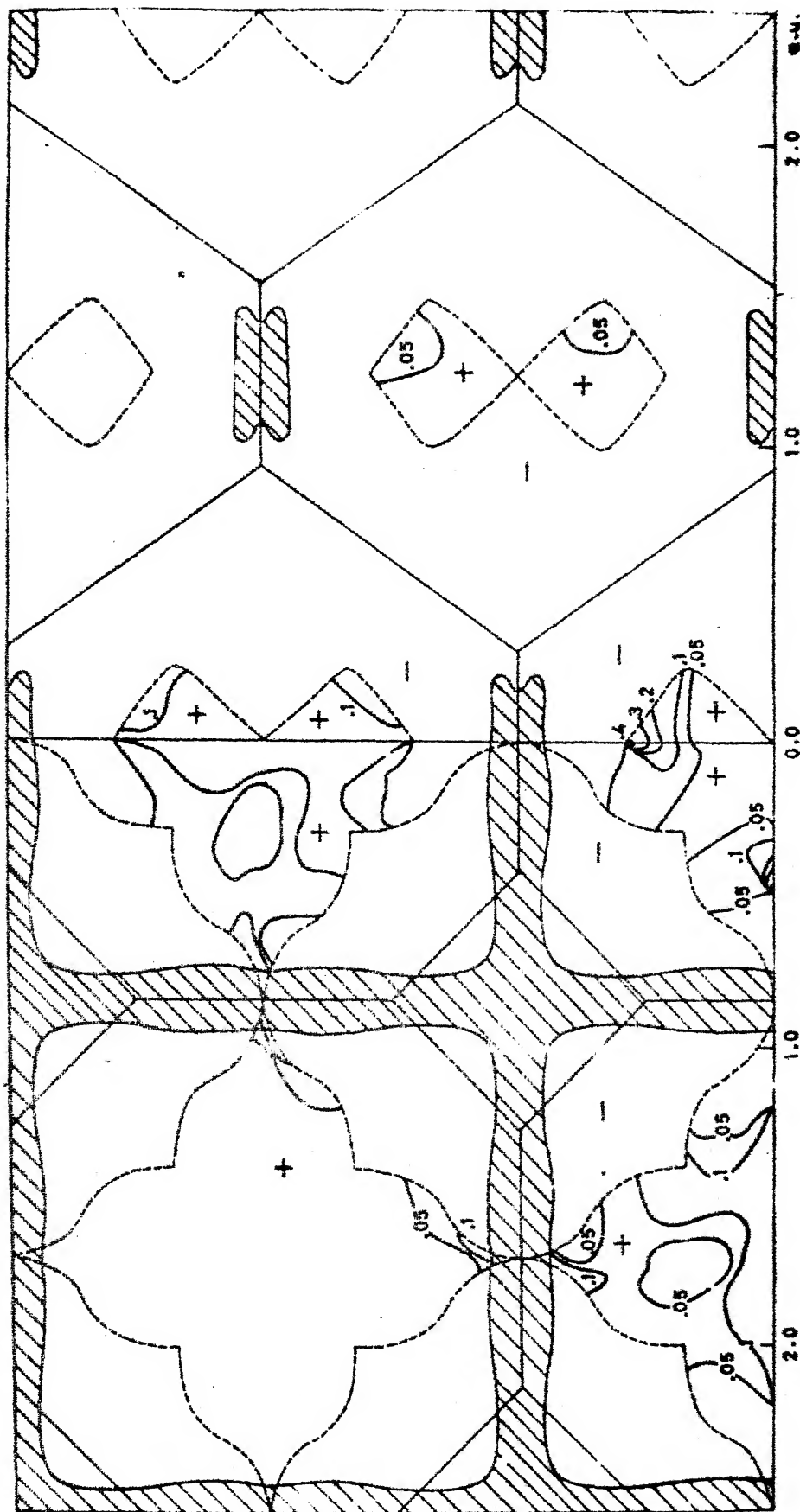
Ed: Rand E

Fig. 4.14: END isodenses for Pd; Band 3.



Id: Band 4

Fig. 4.15: EMD isodensities for Pd: Band 4.



Pd: Band 5

FIG. 4.16: EMD isodensities for Pd: Band 5.

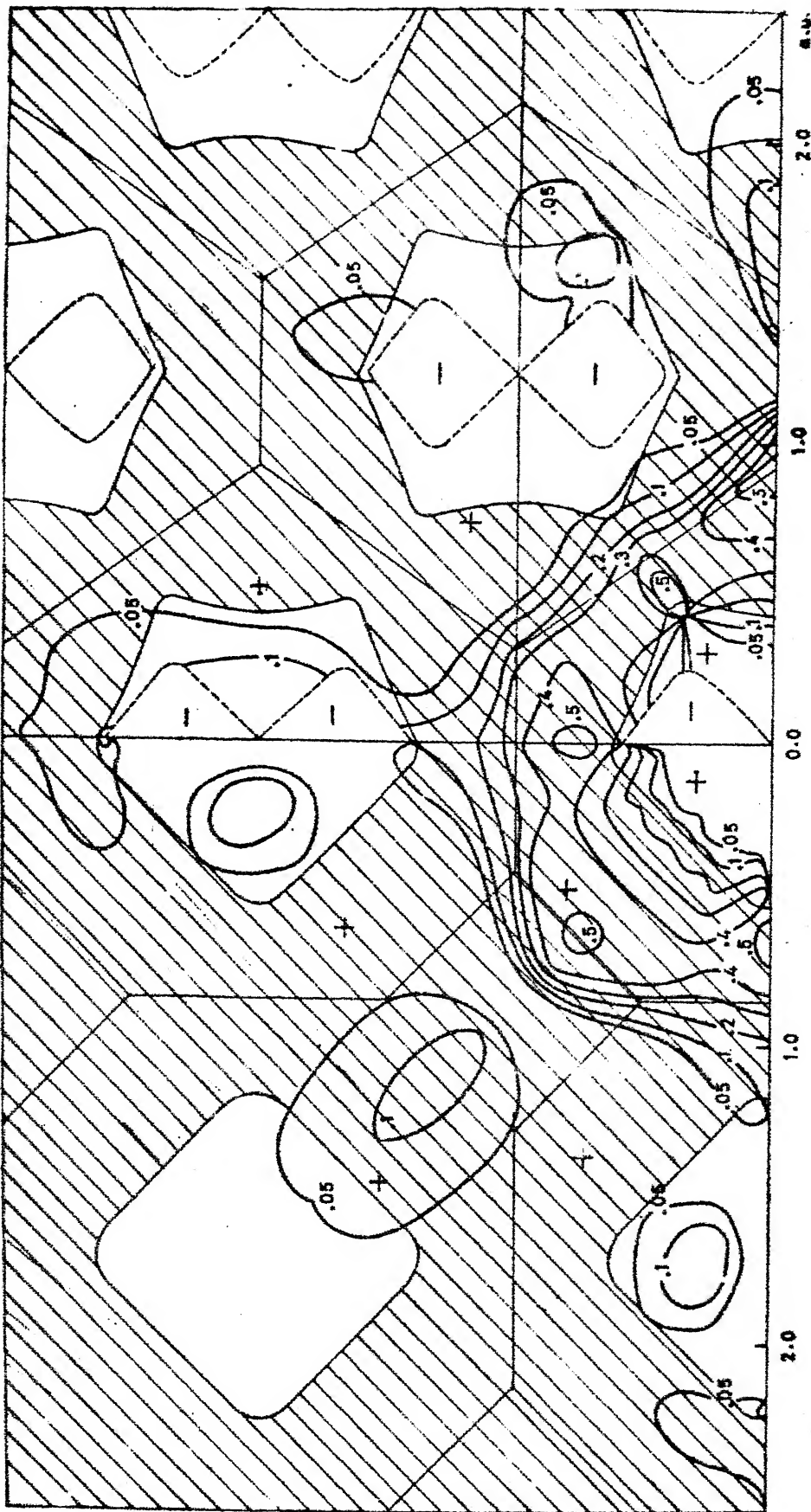


Fig. 4.17: EMD isodenses for Pd: Band 6.

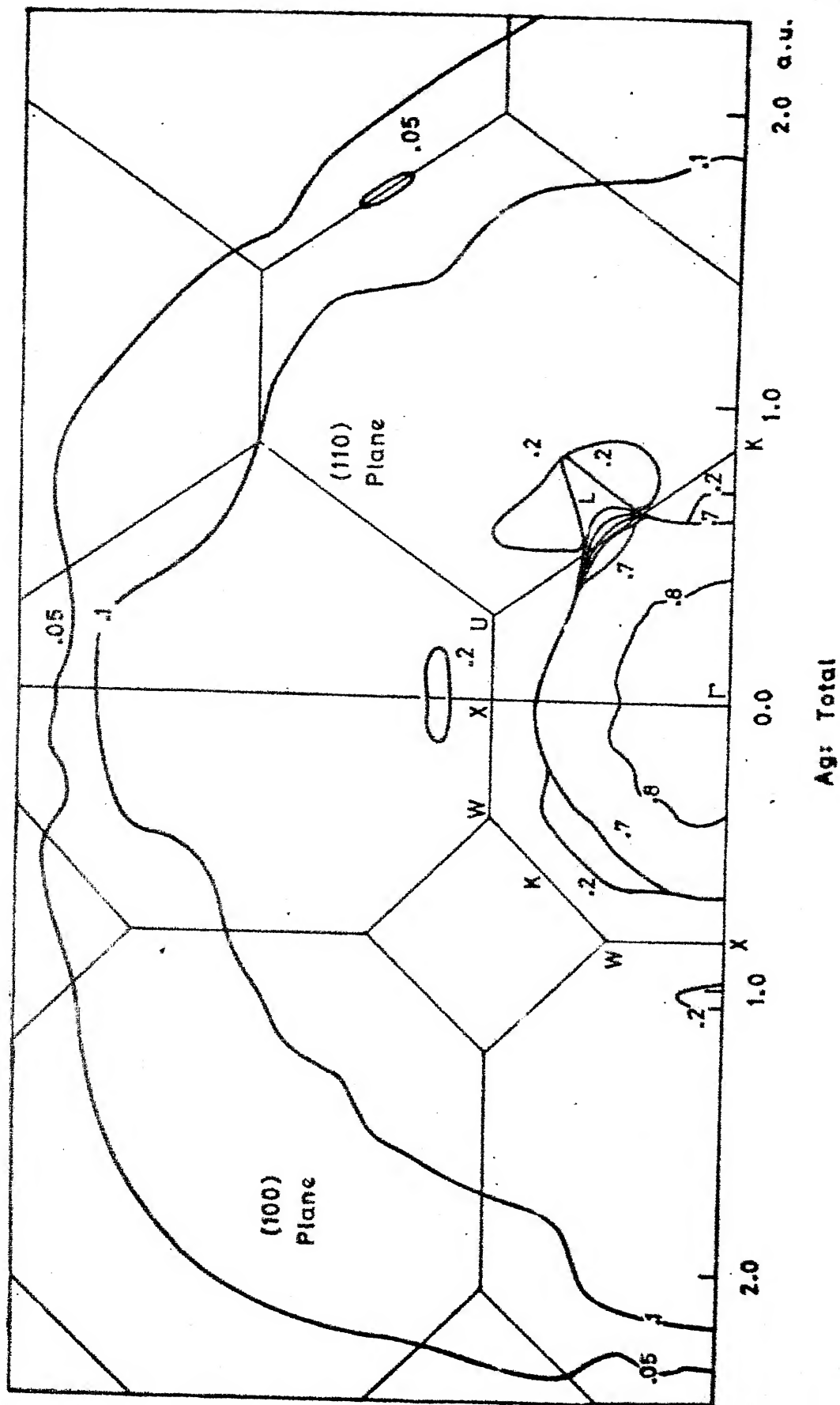
shaded area. The \pm signs indicate the representation of the band electron wavefunction in that region. The zone boundaries are shown by thin lines whereas the isodensities (contours) are shown by thick curves and magnitude of the EMD is indicated by the numbers 0.05, 0.1, 0.2, ..., 0.8, shown on the contours.

The total EMD for Pd (Fig. 4.11) in the (100) and (110) planes shows strong anisotropies even in the first zone. The isodensities for $\rho(\vec{p}) = 0.3 - 0.5$ show bulges in the (100) and (110) planes, arising mainly from the first band and partly from the second band (Figs. 4.12 and 4.13). This result indicates that for Pd even the low-lying, completely filled bands contribute to the anisotropy of the EMD. This aspect is made more clear if the isodensities of band 1, 2 and 3 (Figs. 4.12 to 4.14) are closely examined. A study of the isodensities in higher zones indicates that their contribution comes mainly from the d bands via the Unklapp process.

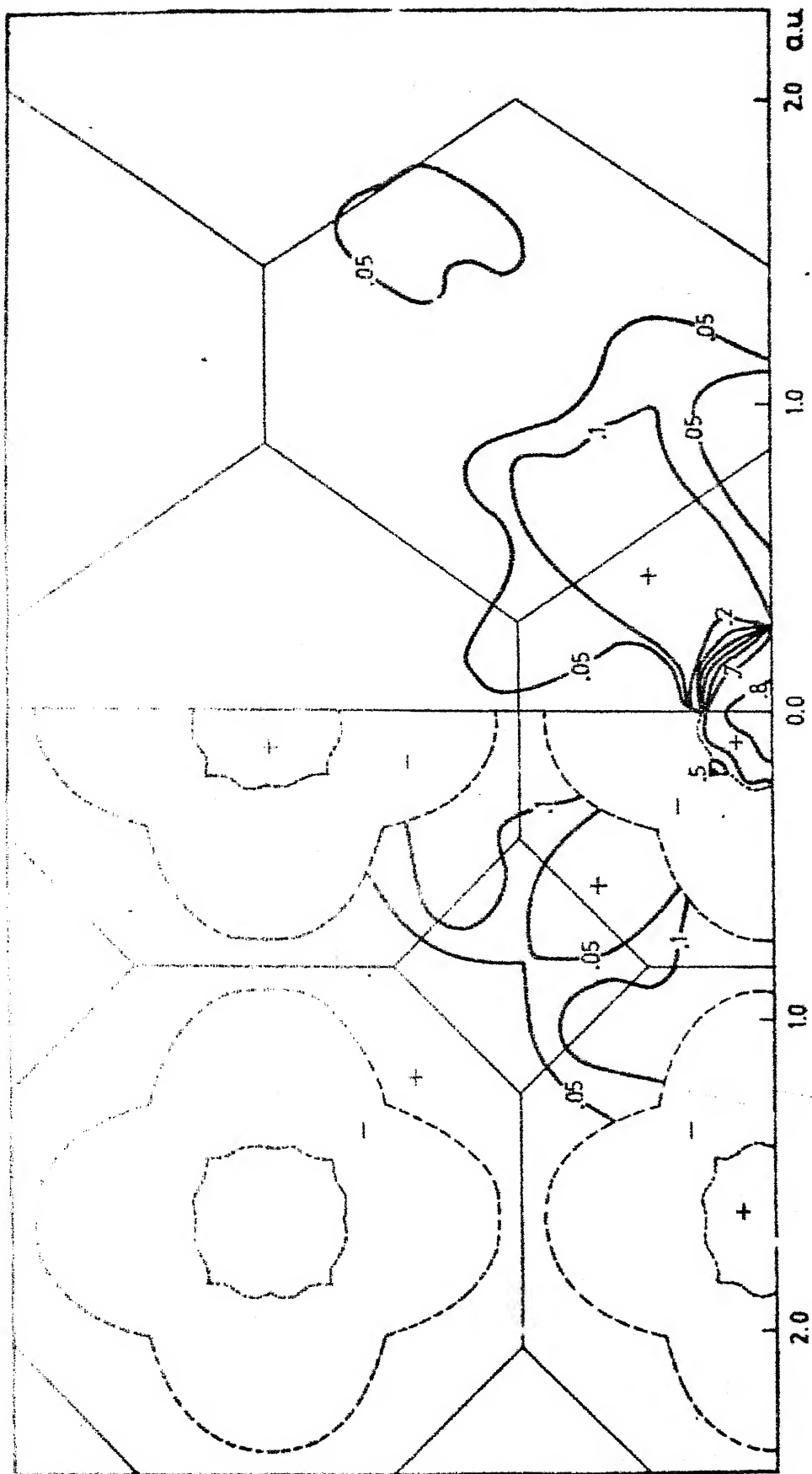
In the (110) plane, band 1 and 2 contribute all over the first zone because their wavefunctions have (+) symmetry and the selection rule [12] allows their contributions. On the other hand, the remaining bands contribute only in those regions of the zones where they have proper (+) symmetry. The validity of this selection rule in our results is nicely brought out by the isodensities. The remarks

made earlier about the effect of s,p,d... character of the bands on the EMD can also explain the nature of EMD in the (100) and (110) planes. Looking at the isodensities of band 4 (Fig. 4.15) we notice that the hole pockets centered around X cannot be observed by Compton profile experiments because of the negligible amount of EMD surrounding them. The fifth-band X-centered hole sheet (jungle-gym structure) is unobservable in the (110) plane owing to the wrong (-) symmetry of the fifth band. Examination of Fig. 4.17 shows that the sixth band contributes to the EMD mostly in the unoccupied parts of the zone. The effect of the Γ -centered sixth band Fermi surface on EMD is most significant along Δ and Σ directions but it becomes less significant as one moves away from these directions. This behaviour is expected to manifest itself in the anisotropy of Compton profiles. It is interesting to note that for the sixth band the contributions in higher occupied zones due to the U-processes are of the same order of magnitude as that in the first occupied zones.

The isodensities for Ag can be analyzed in a manner similar to the discussions given for Pd. Generally the anisotropy observed for Ag is less than that observed for Pd. The total EMD (Fig. 4.18) in the (100) plane falls off rather sharply in the first zone but the decline is slower in the higher zones. This behaviour is largely due to

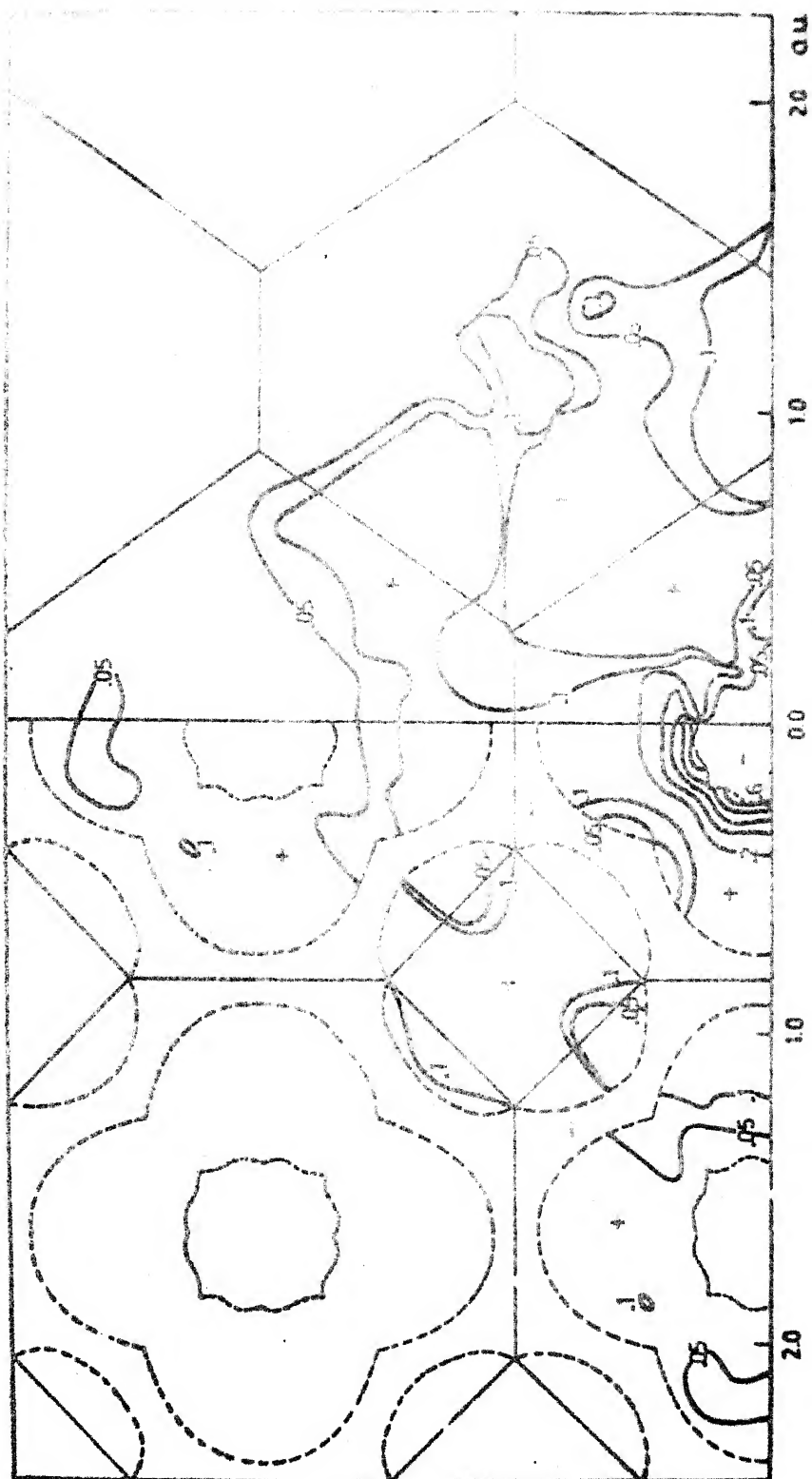


21. 1. 19: EMD isodenses for Ag: Total



Ag: band 1

Fig. 7.1: EMD isodensities for Agt Band 1.



Ag : band 2

Fig. 4.20: 3D isodensities for band 2.

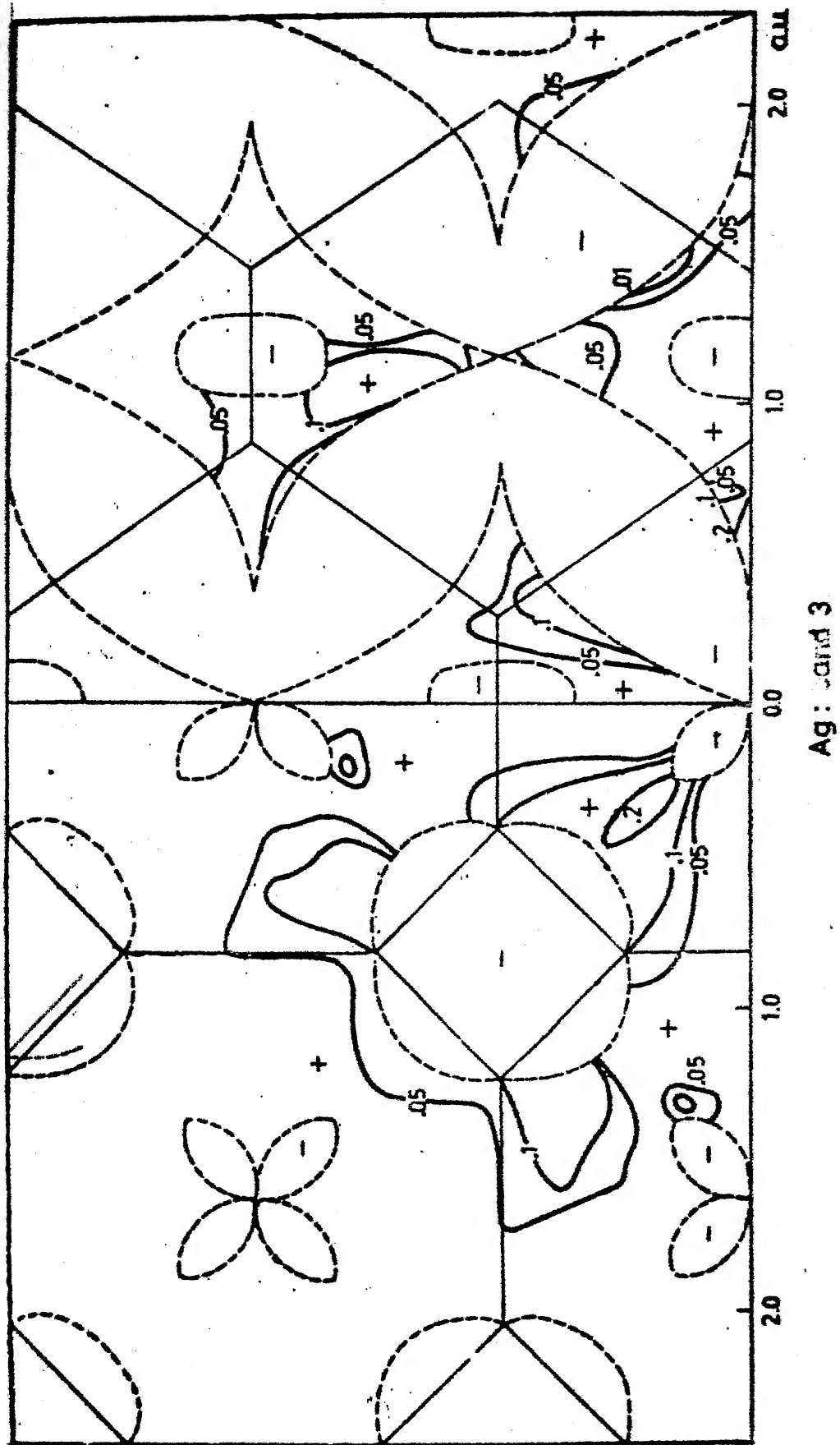
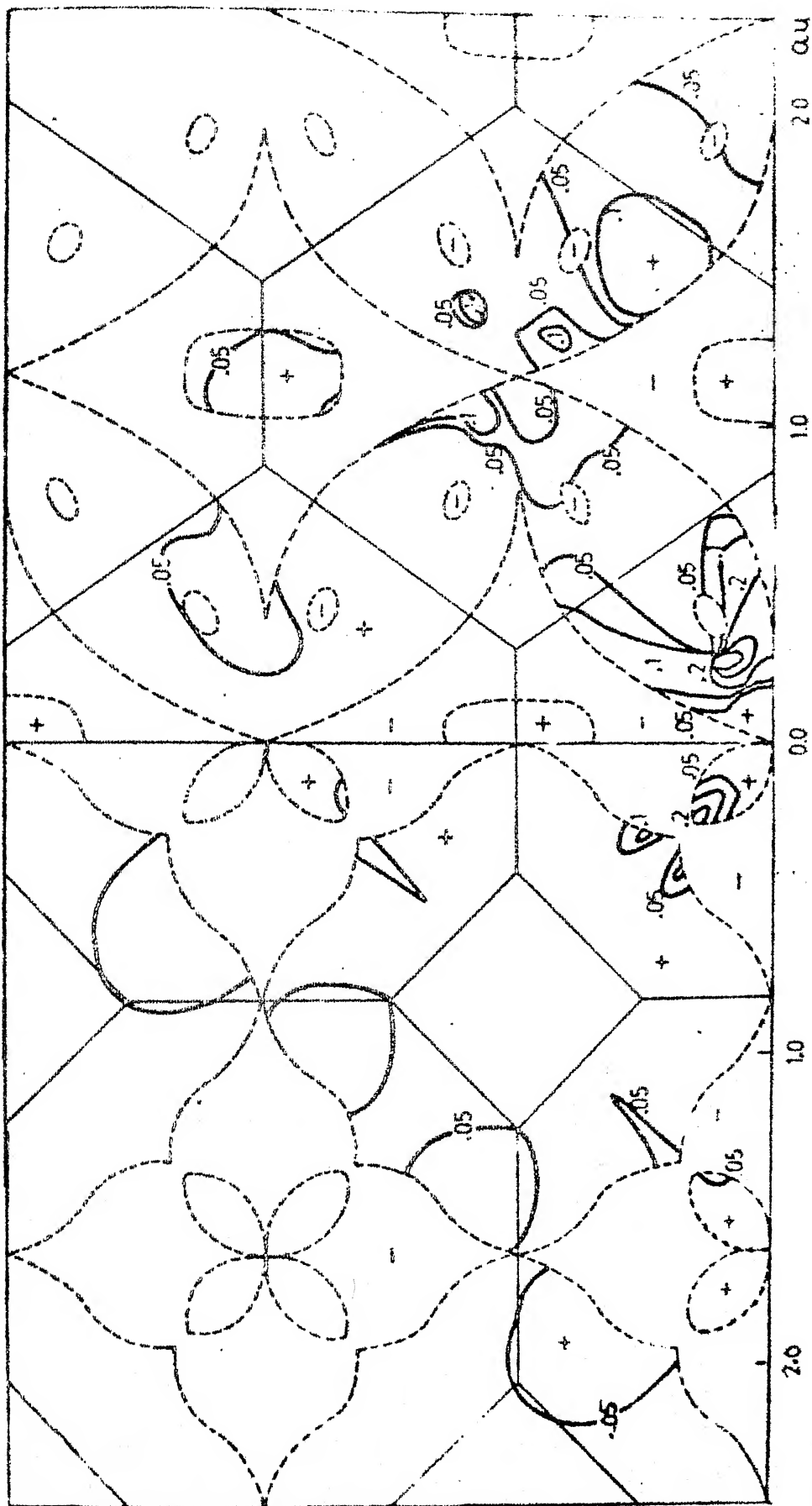
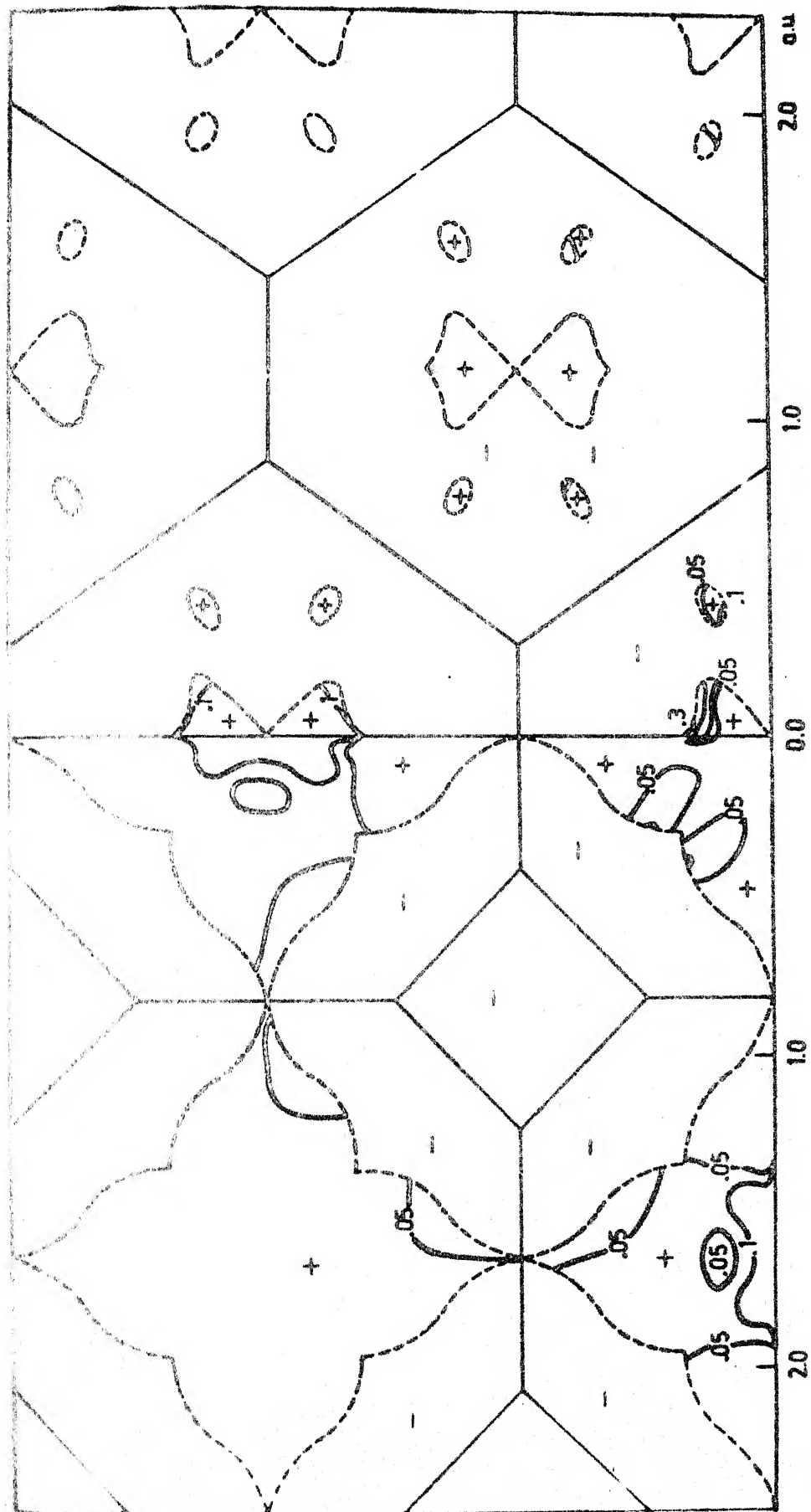


Fig. 4.21: EMD isodensities for Ag: Band 3.



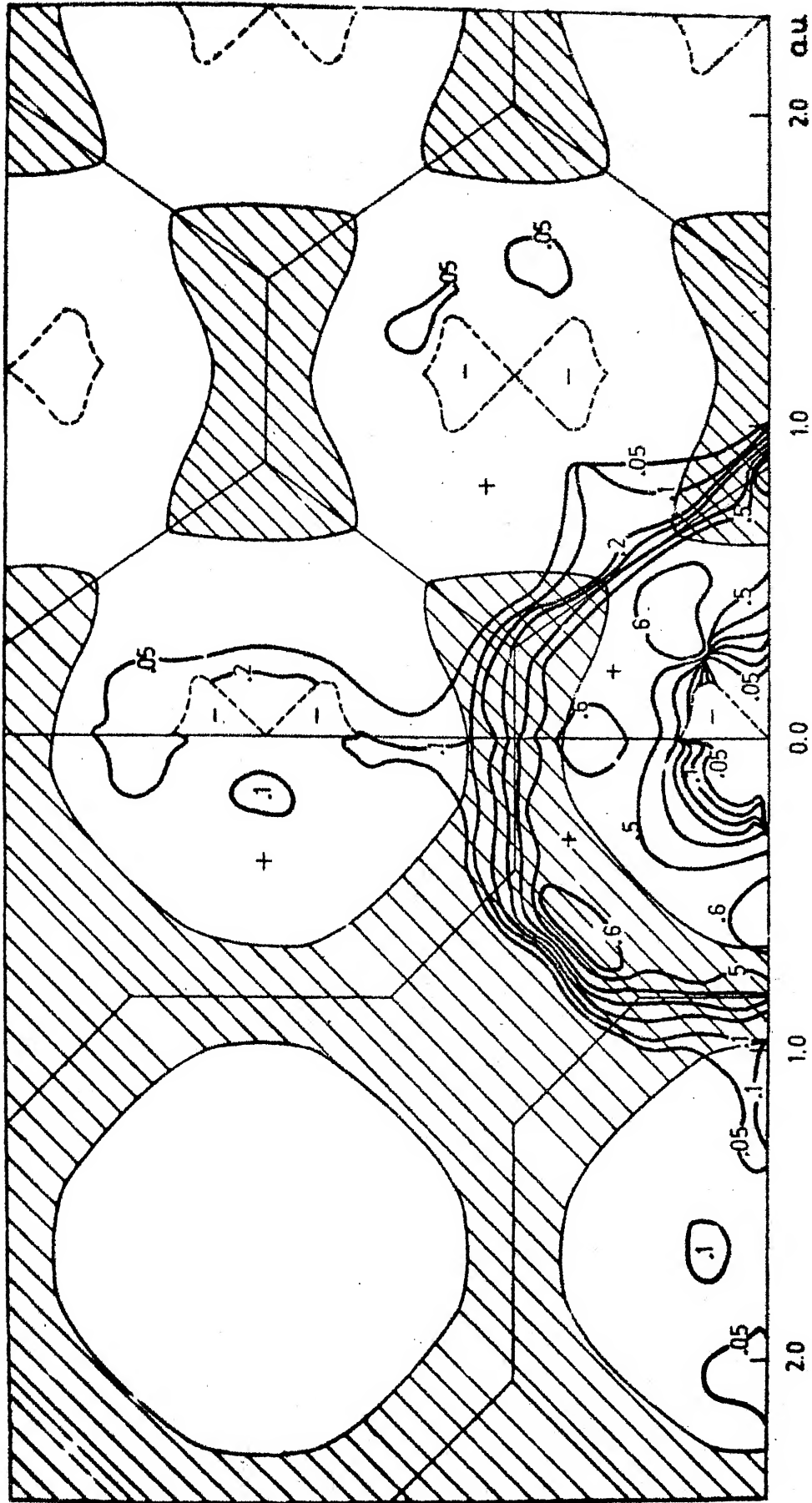
Ag : band 4.

FIG. 4.22: END isodensities for Ag: Band 4.



Ag : band 5.

Fig. 4.23: EMD isodensities for Ag: Band 5.



Ag : band 6.

Fig. 4.24: EMD isodensities for Ag1 Band 6.

the fact that for Ag the 5th band contributes significantly to the EMD near Fermi surface. The effect of the neck of the Fermi surface of Ag is clearly visible along the $[111]$ direction near L in Figs. 4.18 and 4.24. For Ag, band 1 contributes throughout the first zone in the (110) plane, but in the (100) plane it contributes only in those parts where it has (+) character. The contribution of the sixth band in the occupied part of the higher zone is much smaller than that in the first zone. A comparison of the total EMD contours (Fig. 4.11 and 4.18) shows that in the first zone, the effects of the sixth band Fermi surface is more important for Ag than for Pd.

We feel that our results for the total EMD (Fig. 4.11 and 4.18) for Pd and Ag can be useful for analyzing a future unfolding of experimental CP data for the reconstruction of EMD. The isodensities for individual bands, however, cannot provide a direct comparison with experimental CP data which are built only by the total EMD. Nevertheless, they can be compared with other theoretical band structure calculations of EMD to examine the effects of band structure on EMD. It may be pointed out that, in principle, the method of quasi-free $(e, 2e)$ scattering studies can measure [13, 14] the energy dependent momentum densities $\rho(\vec{k}, E)$.

4.4 Comparison of EMD: Ni vs Pd, Cu vs Ag.

A comparison of the total EMD for the isoelectronic elements Ni [15] and Pd along the symmetry directions [100], [110] and [111] shows that although the overall features of the EMD are similar, there are significant differences in their EMD along [111] direction. These differences are due to the 6th band Fermi surface. It must be remembered that Ni being ferromagnetic a direct comparison with Pd is not possible. However, the minor differences along [100] and [110] direction can be understood in terms of the crossing of the sixth band with the Fermi level.

A comparison between the isoelectronic elements Cu [12] and Ag reveals a remarkable similarity in their EMD, an observation to be expected from their similar band structure (characteristic of noble metals). Our results show that small changes in the neck radii (along the [111] direction) of these two metals do not show up significantly in their total EMD.

It would be interesting to compare the results of EMD for ACPAR and CP employing same electron wavefunctions. Such results for Pd [16] indicate a similarity between the two EMD's in the first zone. However, differences appear in the higher zones as CP shows significant high momentum components. As pointed out in Chapter 1, this behaviour is

to be expected because the positron is kept away from the nucleus and annihilates preferentially with the outer (conduction) electrons.

4.5 Limitations of Our Calculations:

In the end we wish to point out some limitations of our calculations.

- i) Firstly the approximations inherent in the Hubbard scheme are expected to limit the accuracy of our wavefunctions.
- ii) Our calculations do not take into account the relativistic effects which can be important for 4d metals. Although the qualitative features of the EMD for Pd and Ag are not expected to be affected much by relativistic effects, a quantitative estimate is not yet available.
- iii) We have calculated the EMD only in the two planes at limited number (≈ 90) of \vec{k} -points. We have not calculated the EMD beyond $p > 3.5$ a.u. because of the limitations of our method. This would limit the use of our results for the calculation of the directional profiles using (1.9).

Inspite of these limitations we feel that our results for Pd and Ag have given a good understanding of the EMD in these metals, underlining the importance of band structure methods for transition metals. The results of the present chapter become more directly applicable when

the methods outlined in Chapter 6 are employed to calculate directional profiles and anisotropies. The results suggest that experimental study of CP in Pd and Ag single crystals should be undertaken and our results (Chapter 4 and 6) can then provide a basis for a proper comparison between theory and experiment. It is known that Pd forms interesting alloys with Ag involving interesting changes in the electronic structure. Such Pd-Ag alloys are being studied by ACPAR [17]. We feel that our results for the EMD of pure Pd and Ag can provide an introductory basis to understand such studies and in particular to examine the role of positron in ACPAR.

REFERENCES

1. K.C. Wong, ICTP Preprint, IC/72/42 (1972).
2. F.M. Mueller, A.J. Freeman, J.O. Dimmock and A.M. Furdyna, Phys. Rev. B1, 4617 (1970).
3. O.K. Andersen, Phys. Rev. B2, 883 (1970).
4. S. Tewari, Solid State Commun. 11, 1157 (1972).
5. J.J. Vuillemin and M.G. Priestly, Phys. Rev. Letts. 14, 307 (1965); J.J. Vuillemin, Phys. Rev. 144, 396 (1966).
6. L.R. Windmiller and J.B. Ketterson, Phys. Rev. Letts. 21, 1076 (1968).
7. S. Bhatnagar, Phys. Rev. 183, 657 (1969).
8. E.C. Snow, Phys. Rev. 172, 709 (1968).
9. D.B.B. Rijssenbrij and J.M. Fondse, Solid State Commun. 17, 1081 (1975).
10. N.E. Christensen, Phys. Status Solidi (b) 54, 551 (1972).
11. D.J. Roaf, Phil. Trans. Roy. Soc. London A 255, 135 (1962-63).
12. P.E. Mijndarends, Physica. 63, 235 (1973).
13. V.G. Levin, V.G. Neudachin and Yu. F. Smirnov, Phys. Status Solidi (b) 49, 489 (1972).
14. R.M. Singru, Phys. Status Solidi (a) 30, 11 (1975).
15. R.M. Singru and P.E. Mijndarends, Phys. Rev. B9, 2372 (1974).
16. D.G. Kanhere and R.M. Singru, Phys. Letts. 53A, 67 (1975).
17. P.E. Mijndarends, private communication.

Chapter 5

SYSTEMATICS OF THE ELECTRON MOMENTUM

DENSITY IN TRANSITION METALS

5.1 Introduction:

Because of the interesting electronic structure of the transition metals, their energy band structure and other ground state properties have been a subject of great theoretical interest. Snow and Waber [1] and Matheiss [2] have systematically studied the band structure and other properties of the 3d metals, Ti through Cu. Although some band structure calculations of the EMD (relevant to CP as well as ACPAR) have been reported in literature, each of these studies pertain either to one or two metals. Similarly different band structure methods have been used for different metals. A systematic study of the EMD for the iron-series 3d metals employing the same band structure method can therefore be interesting. In this chapter we present our results for the EMD (pertaining to CP) for the 3d metals V, Cr, Fe, Ni and Cu calculated by employing Hubbard-Mijnarends-method. These results are then qualitatively discussed in terms of their respective band structure and systematic trends are pointed out.

5.2 The Band Structure of 3d Metals:

The band structure and the EMD for V, Cr, Fe, Ni and Cu were calculated along the three symmetry directions Δ , Σ and Λ by the method described in Chapter 3. The muffin-tin potential for Cr was generated by Lowdin's α -expansion method [1,3] using full Slater exchange. Atomic charge densities for the configuration $3d^n s^1$ were generated by using Herman-Skillman programme [4]. Muffin-tin potentials as reported by Mijnders [5], Wood [6], Wakoh [7,8] and Burdick [9] were used for V, Fe, Ni and Cu respectively. Other computational details are common and they are already discussed in Chapter 3.

Table 5.1 shows the lattice constant, important energy bandwidths, location of the resonance ϵ_d for the d phase shifts and location of Fermi energy (E_F) with respect to the bottom of the conduction band (Γ_1) for these metals. A detailed discussion of the systematics displayed by the energy bands etc. by these metals is given by Snow and Waber [1]. Our present calculations show trends similar to these. The band structure of all the transition metals is characterised by the presence of a fairly narrow d band that overlaps and hybridizes with a broader (and nearly free-electron) s-p band. As one goes along the iron 3d series one observes the following characteristics;

Table 5.1

Some parameters and bandwidths for the 3d transition metals.
All the energy values are in Rydbergs.

	V	Cr	Fe	Ni	Cu
a, lattice constant (a.u.)	5.7225	5.4494	5.406	6.65	6.8309
ϵ_d	0.868	0.892	0.492	0.534	0.306
$E_F - \Gamma_1$	0.54	0.58	0.59	0.67	0.66
Width of the 'd' band	0.55	0.52	0.40	0.36	0.265
Width of the occupied 'd' band	0.23	0.25	0.35	0.36	Completely occupied

where ϵ_d : Location of the resonance in $\tan \gamma_{12}$

$E_F - \Gamma_1$: Position of the Fermi level with respect to the bottom of the conduction band.

$X_5 - X_1$: Width of the 'd' band for fcc metals

$H_2 - H_{12}$: Width of the 'd' band for bcc metals

$E_F - X_1$: Width of the occupied 'd' band for fcc metals

$E_F - H_{12}$: Width of the occupied 'd' band for bcc metals.

a) As the atomic number increases ($Z = 23$ to 29) the 3d states are grouped into small energy range, i.e. the d-like states are more and more tightly bound. The width of the total d band ($X_5 - X_1$ or $H_{2,5} - H_{12}$, as shown in Table 5.1) decreases from V to Cu, but the width of the occupied d band ($E_F - X_1$ or $E_F - H_{12}$) increases.

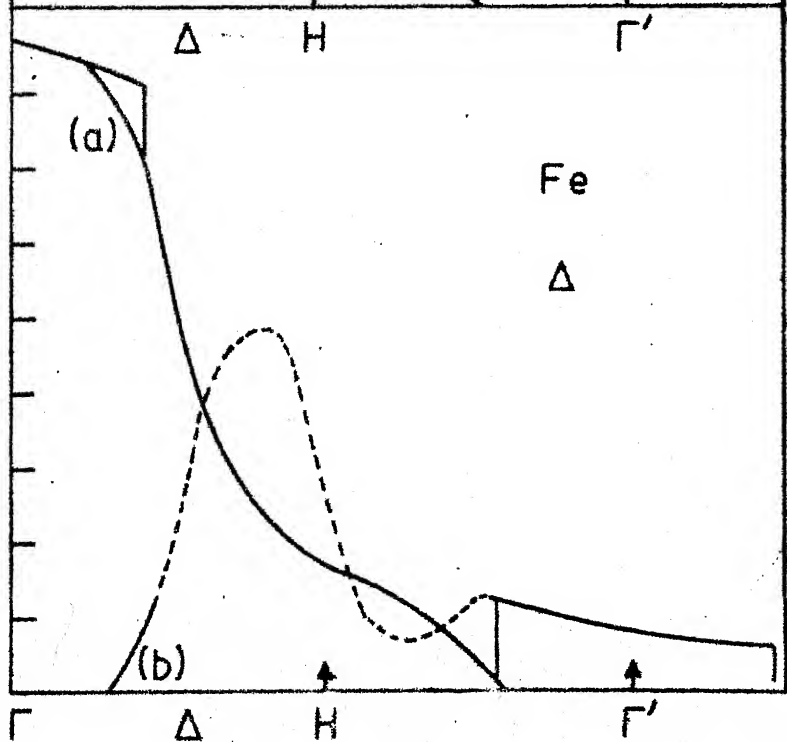
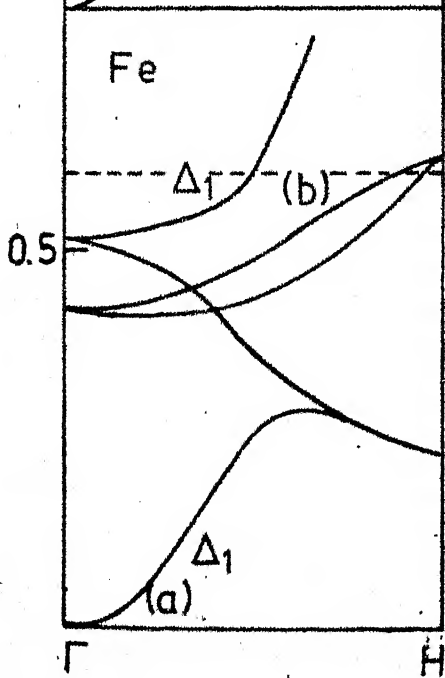
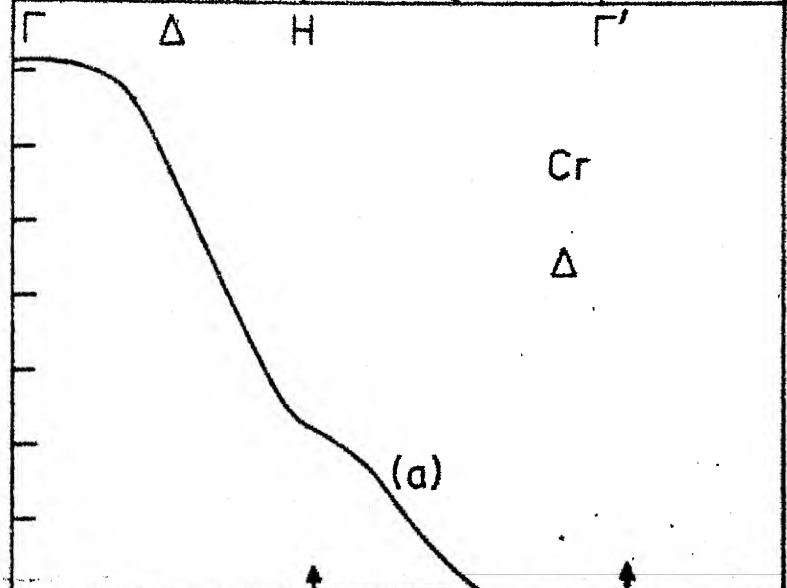
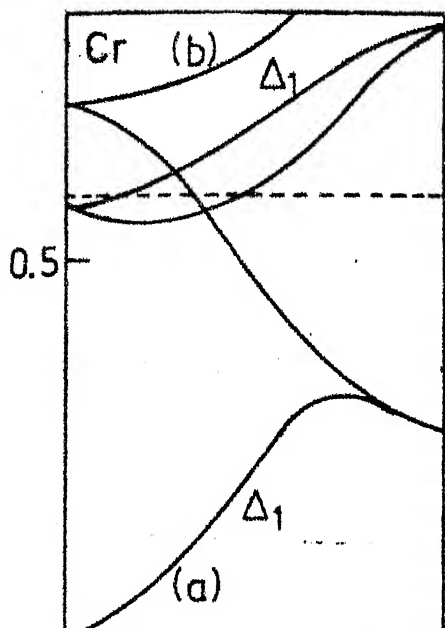
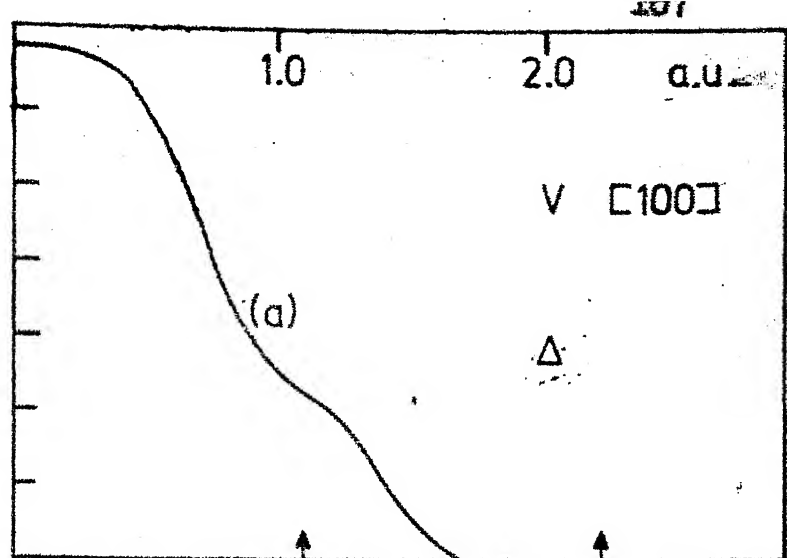
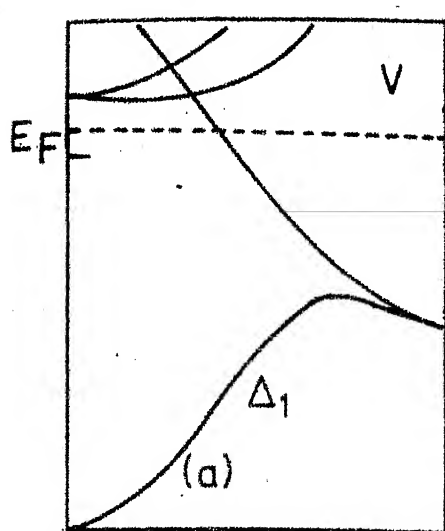
b) Compared with the bottom of the conduction band, ($E_F - \Gamma_1$) the Fermi level (E_F) rises with the atomic number because more and more d electrons are being accommodated.

5.3 Results for the EMD of 3d Metals and Discussion:

The plots of the total as well as band-by-band EMD for V, Cr, Fe (all bcc), and Ni and Cu (both fcc) along the three symmetry direction Δ , Σ and Λ are shown in Figs. 5.1 - 5.6. The relevant band structure is also shown in the figures. It is more convenient to divide the discussion about the systematics of these results according to the symmetry directions.

a) $\Delta(100)$ Direction:

The striking feature displayed by the total EMD is the sharp breaks occurring for Fe, Ni and Cu at their Fermi momenta (p_F). In the case of V and Cr only the occupied lower Δ_1 band contributes and the EMD shows a smooth character with no breaks at p_F . A small step appears for Fe as the higher Δ_1 band becomes partially occupied,



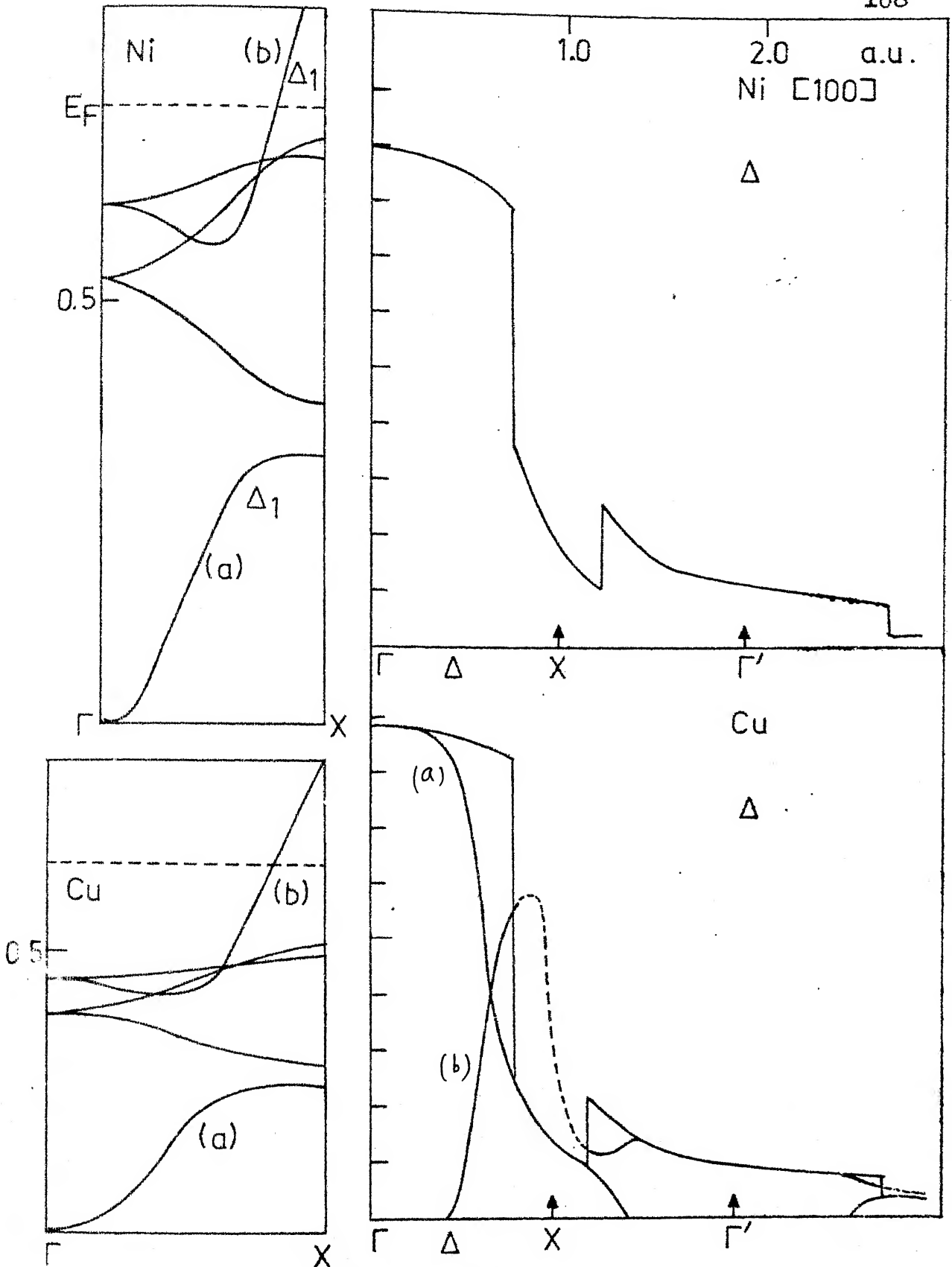


Fig. 5.2: Energy bands and $\rho(\vec{p})$ for Ni and Cu along [100] direction. The vertical scale of energy in the case of Ni is different.

and the step becomes progressively steeper for Ni and Cu. This effect can be understood by noting that for Fe the state at E_F has dominantly d-character while for Ni and Cu the character progressively changes to p-like. This behaviour is a consequence of the hybridization of the two Δ_1 bands. For V and Cr, the high momentum ($p > 2$ a.u) component (HMC) are absent while for Fe, Cu and Ni they are appreciable even at $p = 3$ a.u. and display smaller steps arising out of the Umklapp-processes (Chapter 1). Contribution to HMC mainly comes from the d-like states. The non-occupation of the d-like states around Γ_{12} in V and Cr explains the absence of the HMC in these metals. In Fe, Ni and Cu, the number of d electrons being more, the higher Δ_1 band starts getting occupied and it contributes to the HMC components (Figs.5.1 and 5.2).

The half width of the EMD contributed by the lower Δ_1 band decreases from 0.85 a.u. (V) to 0.6 a.u. (Cu) and the peak value $\rho(0)$ increases from 0.68 (V) to 0.89 (Cu). This behaviour of $\rho(0)$ signifies that the s-like states at Γ_1 become more and more spreadout in r-space as one goes along the series. The effect may also be due to the decrease in the d bandwidth and sp-d hybridization. Although the hybridization effect is seen for Fe, Ni and Cu around $p = 0.4 - 0.8$ a.u. in the EMD curves of the individual bands, the total EMD does not show such effect significantly.

However, in V and Cr where only the lowest hybridized band contributes, a small bulge is seen near the zone face.

b) Σ (110) Direction:

This is the most interesting direction to compare the systematics of EMD. Firstly, the EMD along this direction shows HMC for all the metals. Secondly the higher Σ_1 band lies closer to the Fermi level, thus making the EMD sensitive to the structure of Fermi surface. The HMC arise from the partial occupation of the higher Σ_1 bands. Fig. 5.7 shows how the position of Fermi level affects nature of EMD in V [10]. In Fig. 5.7, index 1 describes the case in which Fermi level cuts Σ_1 band twice giving rise to a multiply connected jungle-gym surface consisting of interconnecting arms along (100) direction and close hole pockets around N. The corresponding EMD shows remarkable structure. On the other hand if we take E_F to lie above point N_1' (Case 2), then the EMD shows no such structure.

Wakoh et al. [11] have shown that experimental results support case 1. Similar analysis can be made for Cr. The presence and size of the steps in Fe, Ni Cu can be explained in terms of the d-character at E_F as in the case of Σ direction.

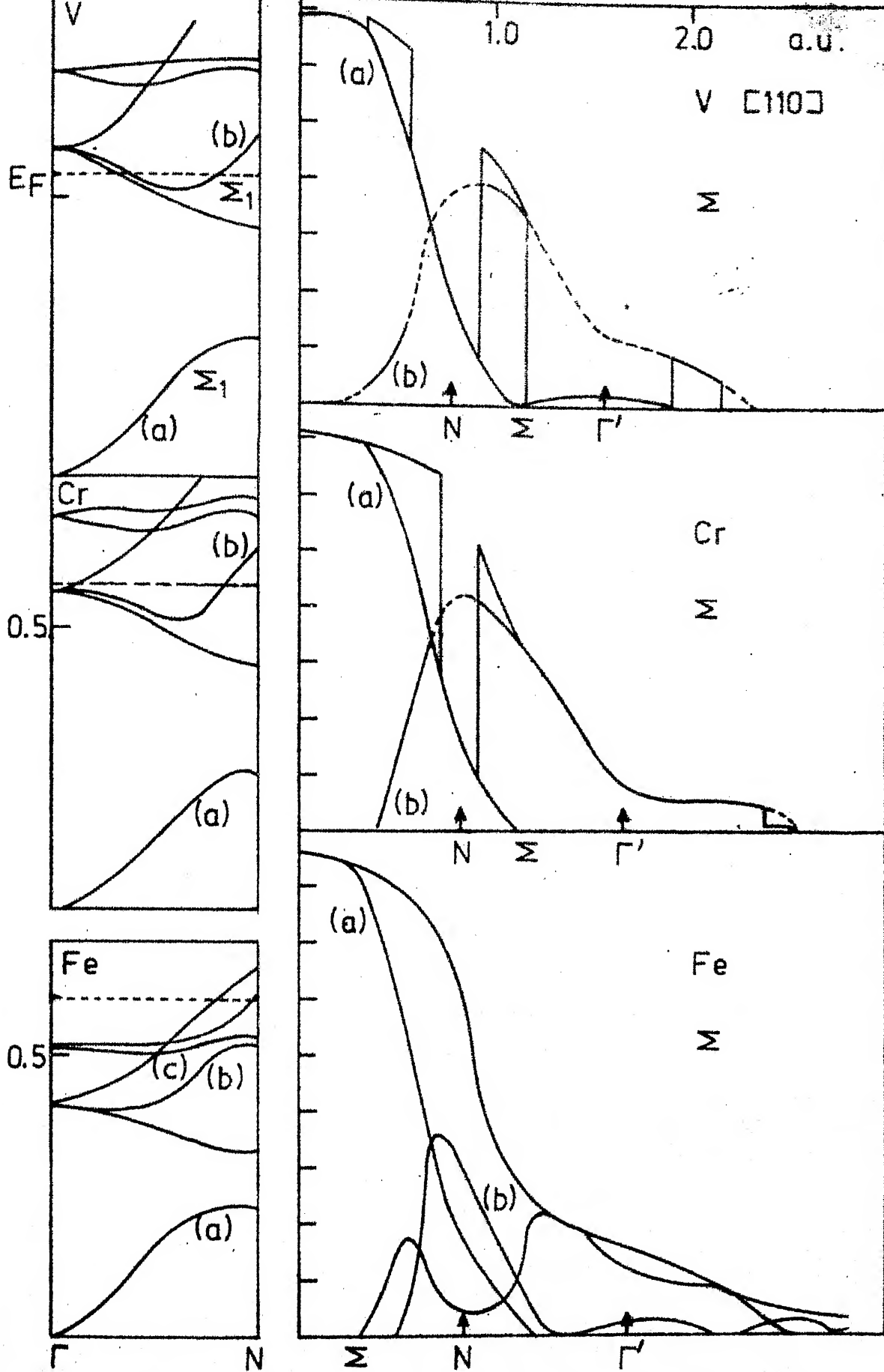


Fig. 5.3: Energy bands and $\rho(p)$ for V, Cr, Fe along [110] direction.

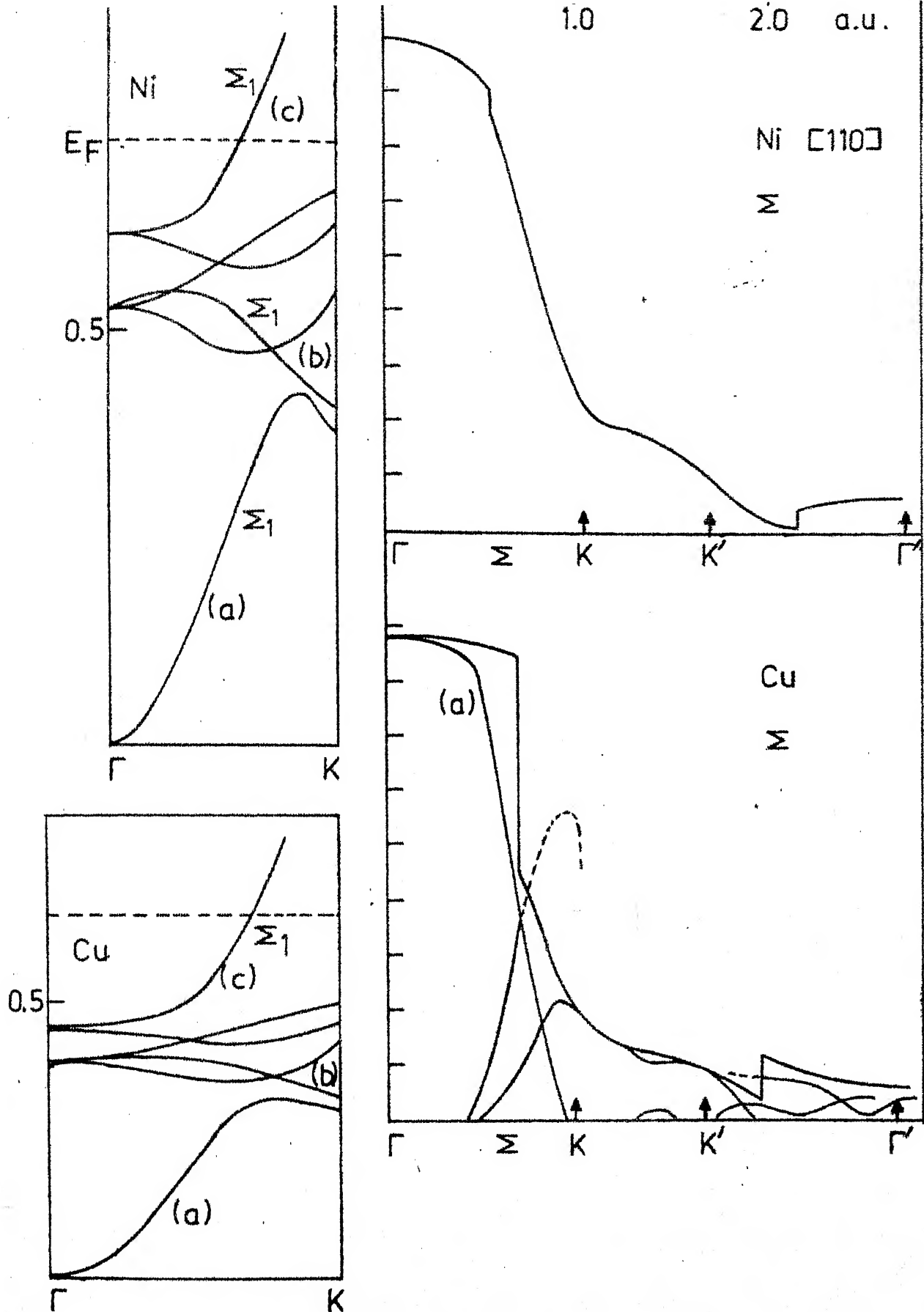
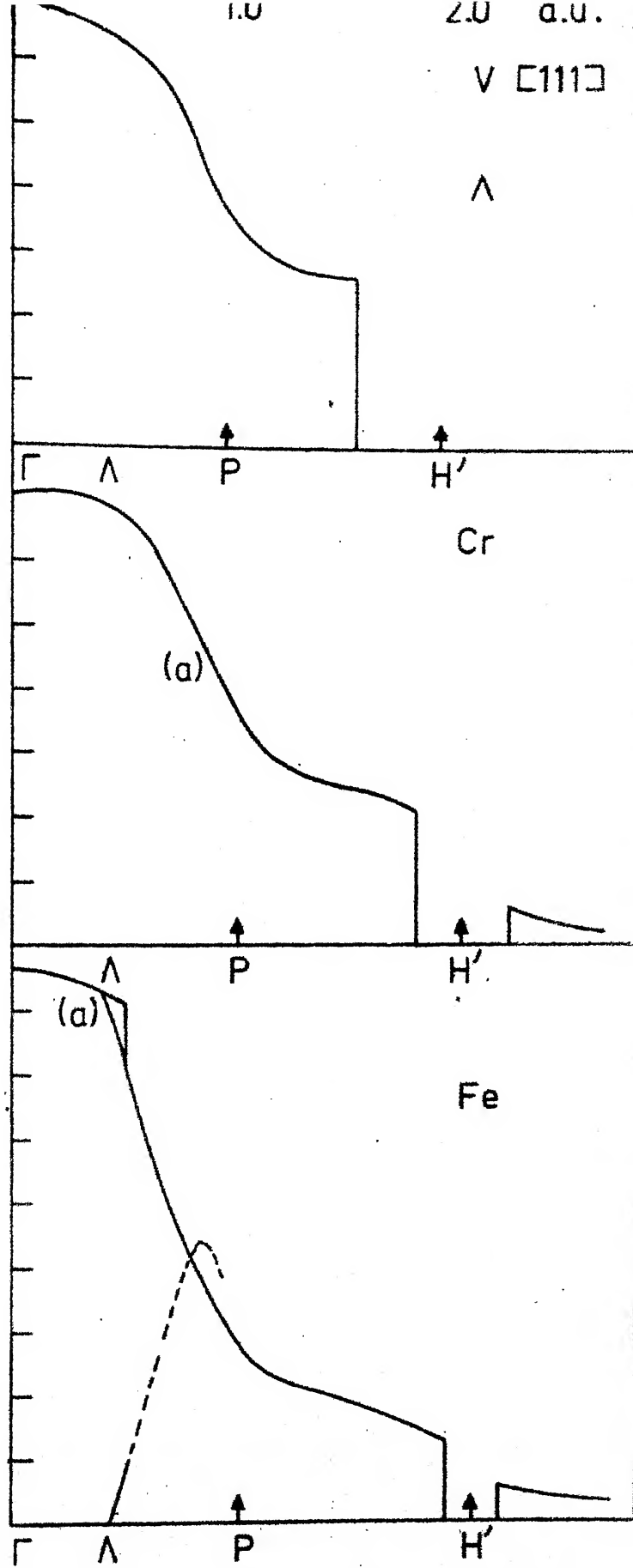
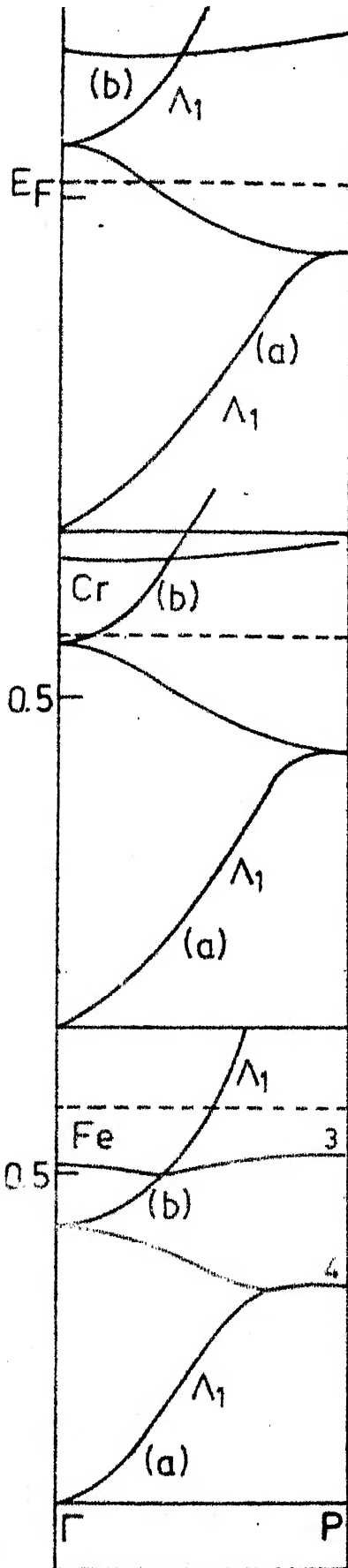


Fig. 5.4: Energy bands and $\rho(\vec{p})$ for Ni and Cu along



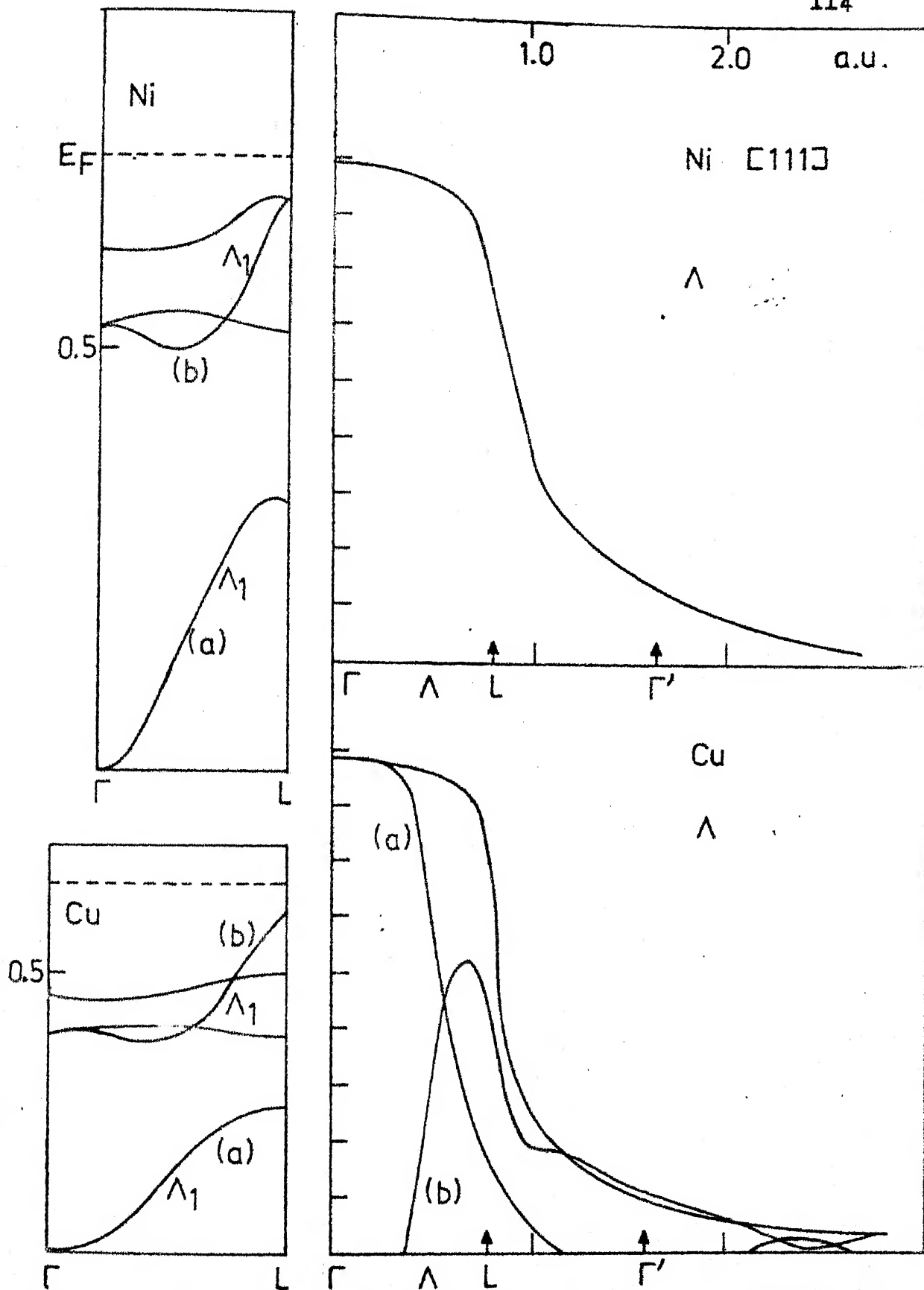


Fig. 5.6: Energy bands and $\rho(p)$ for Ni and Cu along [111] direction. The vertical

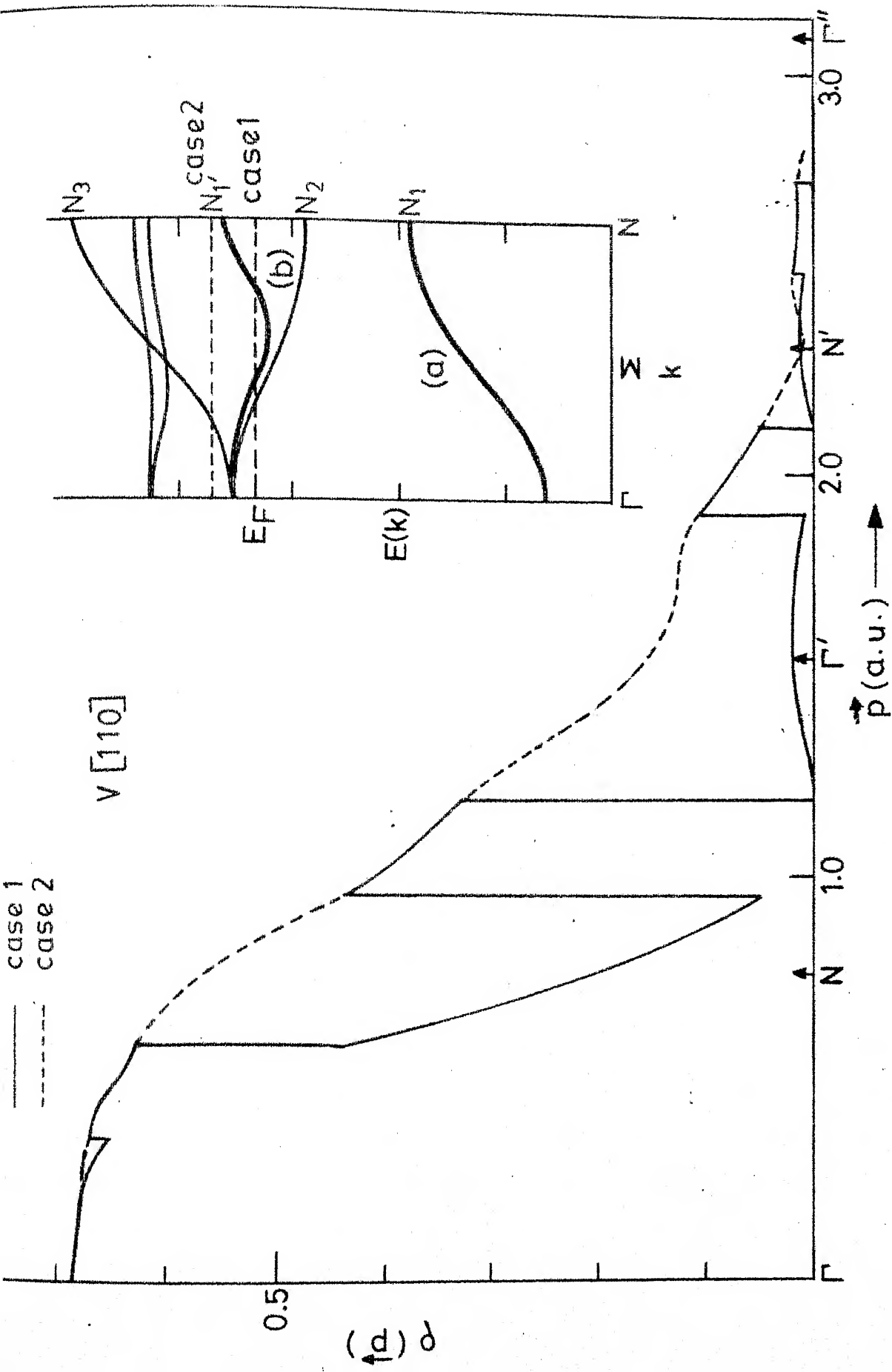


Fig. 5.7: $\rho(\vec{p})$ for V along $[110]$ direction for two locations of E_F as discussed in the text.

Along the Σ direction the HMC component is shown up even for V and Cr. The contributions to these HMC come mainly from the U-processes due to the 'd' like character in the Σ_1 bands.

c) Λ (111) Direction:

The Λ direction can be analysed in a similar fashion. A peculiar feature of the bcc metals is that, all of them show a sharp drop in the EMD in the 2nd zone due to U-process; even though the lowest Λ_1 band is completely occupied. This happens because the contribution to the EMD from P to H' in the second zone comes from the U-process with the \vec{k} lying on the PH line (or F bands), where F_1 is being partially filled. In Ni and Cu the EMD shows a smooth behaviour since both the bands are completely occupied, which is associated with the 'neck' of the FS.

It may be added that we have also calculated the EMD in Rh and it shows a trend similar to the 4d (fcc) metals Pd and Ag. A systematic study of the 4d metals cannot be made until the EMD in Nb; Mo .. is calculated. Work in this direction is now in progress.

To summarise, the analysis of this chapter indicates that the anisotropic contribution to the EMD, $\rho(\vec{p})$, comes from

- i) the Fermi surface, and
- ii) the d-electrons.

The effects of the FS are dominant in the first zone. For the high momentum region the anisotropies come mainly from the d electron wavefunctions, and their t_{2g} and e_g character.

REFERENCES

1. E.C. Snow and J.T. Waber, *Acta Metallurgica* 17, 623 (1969).
2. L.F. Mattheiss, *Phys. Rev.* 134, 192 (1964).
3. We are thankful to Dr. Sushma Tewari for making these computer programs available to us.
4. F. Herman and S. Skillman, *Atomic Structure Calculations*, (Prentice Hall, Inc., Englewood Cliffs, New Jersey, 1963).
5. P.E. Mijnenarends, Report RCN-76-010 (1976), Unpublished.
6. J.H. Wood, *Phys. Rev.* 126, 157 (1962).
7. S. Wakoh, *J. Phys. Soc. Jap.* 20, 1894 (1965).
8. The EMD for Ni was taken to be that for the majority bands from R.M. Singru and P.E. Mijnenarends, *Phys. Rev.* B9, 2372 (1974).
9. G.A. Burdick, *Phys. Rev.* 129, 163 (1963).
10. K.R.K. Gandhi, Private communication.
11. S. Wakoh, Y. Kubo, J. Yamashita, *J. Phys. Soc. Jap.* (to be published).

Chapter 6

DIRECTIONAL COMPTON PROFILES AND ANISOTROPIES OF Pd AND Ag

6.1 Introduction:

In the last two chapters a detailed study of the EMD in transition metals, particularly in Pd and Ag was presented in terms of their respective band structure. As shown by Eq. (1.7), the Compton profile (or the ACPAR) does not measure the EMD, $\rho(\vec{p})$, directly. It was noted in Chapter 1 that a comparison between theoretical and experimental results can be carried out in two ways: (i) reconstruct three-dimensional distribution $\rho(\vec{p})$ from measured profiles and compare it with theoretical $\rho(\vec{p})$ or (ii) construct directional profiles* $J_{hkl}(p_z)$ from theoretical $\rho(\vec{p})$ and compare these (or their differences) with experimental results.

The former method of reconstruction of EMD has been suggested by Mijnenreids [1] who expanded the EMD in a series of lattice (Kubic) harmonics. Employing this method, directional profiles from single crystal specimens of Cu [1], Fe [2], Li [3], diamond [4], Si [5], Fe_3O_4 [6], Zn [7], Mg [8], Cd [8] and Ni [9] have been analysed. Recently Mueller [10] has developed a Fourier method to reconstruct EMD and has applied it to Si.

* In the following we shall use the common term 'profile' for the directional Compton profile $J_{hkl}(p_z)$ or the ACPAR curve $N_{hkl}(p_z)$ and denote these by a common symbol J_{hkl} .

The above method of reconstruction of EMD is beset with some problems. Majumdar [11] has analyzed the method of Mijnders and has pointed out that truncation errors can be serious and that unique solutions of $\rho(\vec{p})$ cannot be obtained unless the truncation coincides with the correct number of terms in the expansion. For all the cases [1-9] analyzed, the reconstructed momentum density shows an oscillatory character at low momenta and only in some cases the theory and experiment are compared satisfactorily.

We feel that the other approach of constructing the directional profiles J_{hkl} from theoretical $\rho(\vec{p})$ is equally important as demonstrated for V [12], Cr [13,14], Fe [14], Ni [14] and Nb [15]. These authors have obtained J_{hkl} by integration of $\rho(\vec{p})$, as shown by Eq. (1.7) in the k-space. However, an integration in k-space demands a knowledge of the $\rho(\vec{p})$ at many p-points, thus involving considerable computational effort. Instead we have explored another approach, based on an expansion of $\rho(\vec{p})$ in terms of lattice harmonics. This method is discussed in the next section.

A comparison between CP theory and experiment can be done in a more sensitive manner if we compare the difference (or anisotropy) curves $J_{hkl} - J_{h'k'l'}$, rather than the directional profiles J_{hkl} . This can be seen by noting that most of the core contributions (about 50% in transition

The above method of reconstruction of EMD is beset with some problems. Majumdar [11] has analyzed the method of Mijnders and has pointed out that truncation errors can be serious and that unique solutions of $\rho(\vec{p})$ cannot be obtained unless the truncation coincides with the correct number of terms in the expansion. For all the cases [1-9] analyzed, the reconstructed momentum density shows an oscillatory character at low momenta and only in some cases the theory and experiment are compared satisfactorily.

We feel that the other approach of constructing the directional profiles J_{hkl} from theoretical $\rho(\vec{p})$ is equally important as demonstrated for V [12], Cr [13,14], Fe [14], Ni [14] and Nb [15]. These authors have obtained J_{hkl} by integration of $\rho(\vec{p})$, as shown by Eq. (1.7) in the k-space. However, an integration in k-space demands a knowledge of the $\rho(\vec{p})$ at many p-points, thus involving considerable computational effort. Instead we have explored another approach, based on an expansion of $\rho(\vec{p})$ in terms of lattice harmonics. This method is discussed in the next section.

A comparison between CP theory and experiment can be done in a more sensitive manner if we compare the difference (or anisotropy) curves $J_{hkl} - J_{h'k'l'}$, rather than the directional profiles J_{hkl} . This can be seen by noting that most of the core contributions (about 50% in transition

metals) as well as some of the experimental uncertainties are subtracted out in the difference curves, making them more sensitive to the band electron wavefunctions. Keeping this in mind we have presented only the difference or anisotropy curves for Pd and Ag in this Chapter.

6.2 Spherical Harmonic Expansion of EMD:

Following Mijnaresends [1] we expand $\rho(\vec{p})$ in a series of lattice harmonics $F_{\ell v}(\vec{\Omega}_{\vec{p}})$ of the appropriate symmetry

$$\rho(\vec{p}) = \sum_{\ell v} \rho_{\ell v}(\vec{p}) F_{\ell v}(\vec{\Omega}_{\vec{p}}) \quad (6.1)$$

where the $F_{\ell v}(\vec{\Omega}_{\vec{p}})$ are an orthonormal set of invariant linear combinations of spherical harmonics of order ℓ and $\vec{\Omega}_{\vec{p}}$ specifies the orientations of \vec{p} with respect to a suitably chosen orthogonal coordinate system. The index v distinguishes the various harmonic of the same order and symmetry type. For cubic lattices which we are considering, only harmonics with $\ell = 0, 4, 6, 8, 10, 12$ (2X), 14 --- will contribute [16], and $m = 0 \pmod{4}$ and positive.

It is now more convenient to define two orthogonal coordinate systems R_c and R_a . The first system $R_c \equiv (\xi, \eta, \zeta)$ is fixed to the crystal and provides the reference system for defining the lattice harmonics. The second coordinate system $R_a \equiv (x, y, z)$ is connected to the apparatus so that its z -axis is along the scattering vector. The two systems

R_c and R_a can be brought into coincidence by a rotation of R_c through the Euler angles [17] α, β, γ . The angles β and γ measure the polar and azimuthal angles of the z-axis (i.e. the scattering vector) respectively. The angle α measures the rotation of the specimen around the scattering vector.

The lattice harmonics $F_{\ell v}(\Omega_{\vec{p}})$ are a linear combination of spherical harmonics

$$F_{\ell v}(\Omega_{\vec{p}}) = \sum_m a_{\ell m v} Y_{\ell}^m(\Omega_{\vec{p}}) \quad (6.2)$$

and as shown by Mijnaerends [1], the directional profile is given by

$$J_{\beta \alpha}(p_z) = 2\pi \sum_{\ell v} F_{\ell v}(\beta, \alpha) g_{\ell v}(p_z) \quad (6.3)$$

where

$$g_{\ell v}(p_z) = \int_{|p_z|}^{\infty} \rho_{\ell v}(p) P_{\ell}(p_z/p) p \, dp \quad (6.4)$$

Equations (6.1) to (6.4) constitute our scheme for the calculation of the directional profiles $J_{\beta \alpha}(p_z)$ from $\rho(\vec{p})$. We proceed through the following steps [18] to achieve our objectives.

- i) Employing band structure method we calculate the energy bands and the wavefunctions.
- ii) We then calculate the EMD, $\rho(\vec{p})$, for several directions of \vec{p} .

- iii) Using the expansion (6.1) we express $\rho(\vec{p})$ in terms of $\rho_{\ell}(\vec{p})$ and $F_{\ell\nu}(\vec{n}_{\vec{p}})$ in a set of linear equations.
- iv) We then solve these sets of equations either by direct inversion or by using a least-square fit, taking care that the number of terms (l - values) retained should be sufficient to ensure convergence.
- v) Knowing $\rho_{\ell}(\vec{p})$ we obtain $g_{\ell}(p_z)$ by (6.4) and then proceed to obtain $J_{\beta\alpha}(p_z)$ by (6.3).

6.3 Application to Ni and Cu:

To test the above procedure we first applied it to the EMD of Ni and Cu for which experimental data about the anisotropies observed from CP and ACHAR measurements were available. Theoretical results of EMD, $\rho(\vec{p})$, used for this work were taken from Singru and Mijnaerends [19], Singru [20] and from our work. Theoretical EMD, $\rho(\vec{p})$, is usually calculated for a limited number (n_1) of directions $\vec{n}_{\vec{p}}$. Therefore, in practice, the expansion series (6.1) is truncated after a finite number (n_2 , where $n_2 \leq n_1$) of terms. Since the theoretical $\rho(\vec{p})$ for Ni and Cu were available only for the three symmetry directions [100], [110] and [111], we have used $n_1 = 3$ and $n_2 = 3$ for our analysis of Ni and Cu. In the next section, we shall discuss the effect of different values of n_1 and n_2 on our results.

Figs. 6.1 (a) and 6.2(a) show the anisotropies for the CP and ACPAR curves for Ni as calculated by us with the method outlined in the previous section. Experimental CP curves measured by Eisenberger and Reed [21] are shown in Fig. 6.1(b) while Fig. 6.2 (b) shows the ACPAR curves reported by Kontrym-Sznajd et al. [9]. Theoretical anisotropies for the CP and ACPAR curves are shown in Figs. 6.3(a) and 6.4 while the experimental CP curves by Eisenberger and Reed [21] and experimental ACPAR curves by Cushner et al. [23] are shown in Figs. 6.3 (b) and 6.5 respectively.

A visual comparison of the theoretical and experimental anisotropies* in Figs. 6.1 to 6.5 reveals that although the main qualitative features of the observed anisotropies are reproduced fairly well by our theoretical curves, there is poor agreement in some areas. These observations are summarised below.

a) In general all the curves show a poor agreement in the very low momentum region $p = 0 - 0.2$ a.u. Most satisfactory agreement is seen for the difference curves $J_{110} - J_{100}$. The agreement worsens as one goes from $J_{110} - J_{111}$ to

$$J_{100} - J_{111}.$$

b) Theoretical curves $J_{110} - J_{111}$ reproduce the observed maxima and minima with a reduced intensity of the lobes.

* The different momentum scales used should be noted while comparing theory and experiment.

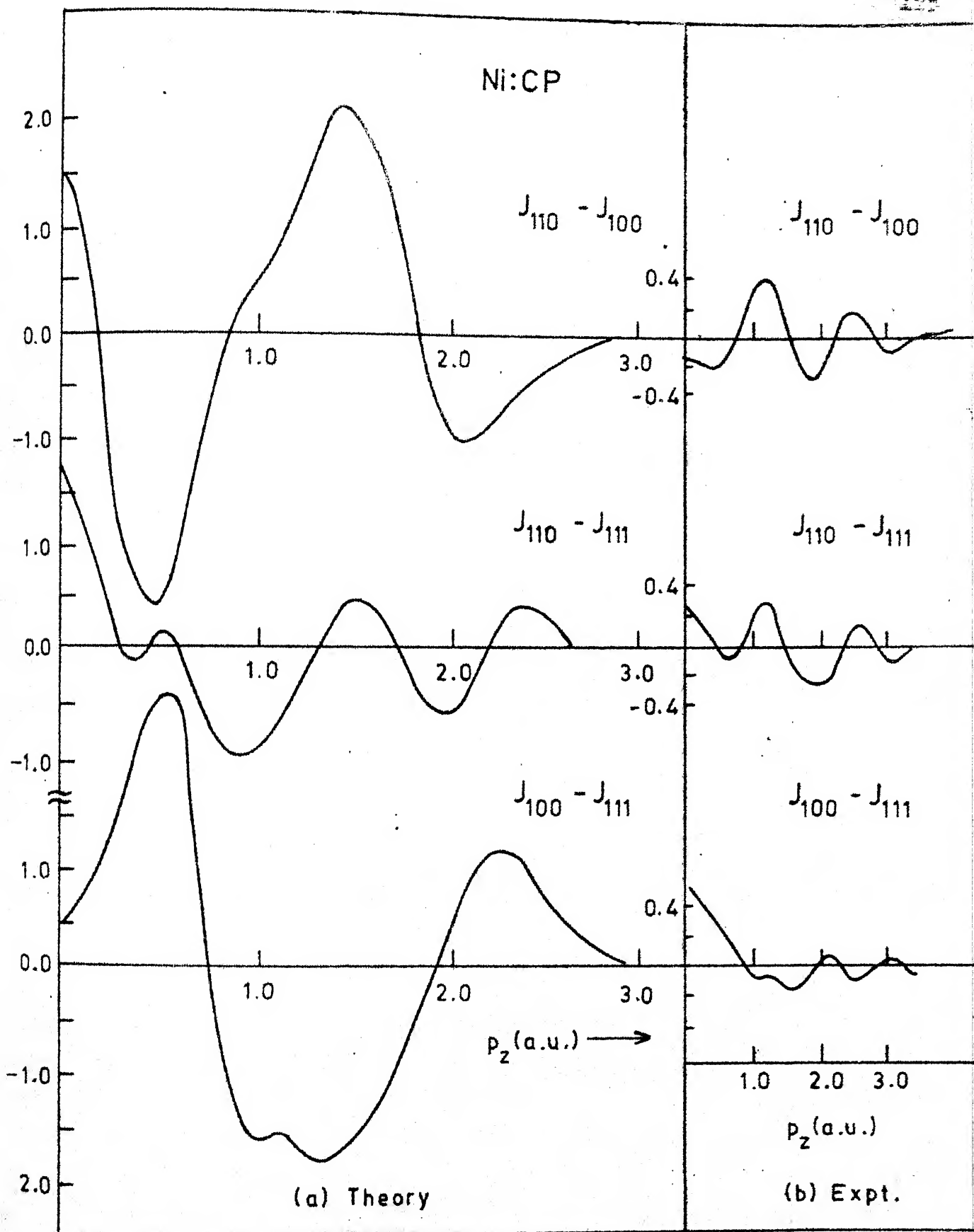


Fig. 6.1: Theoretical and experimental CP anisotropies for Ni. Note the difference in momentum scale.

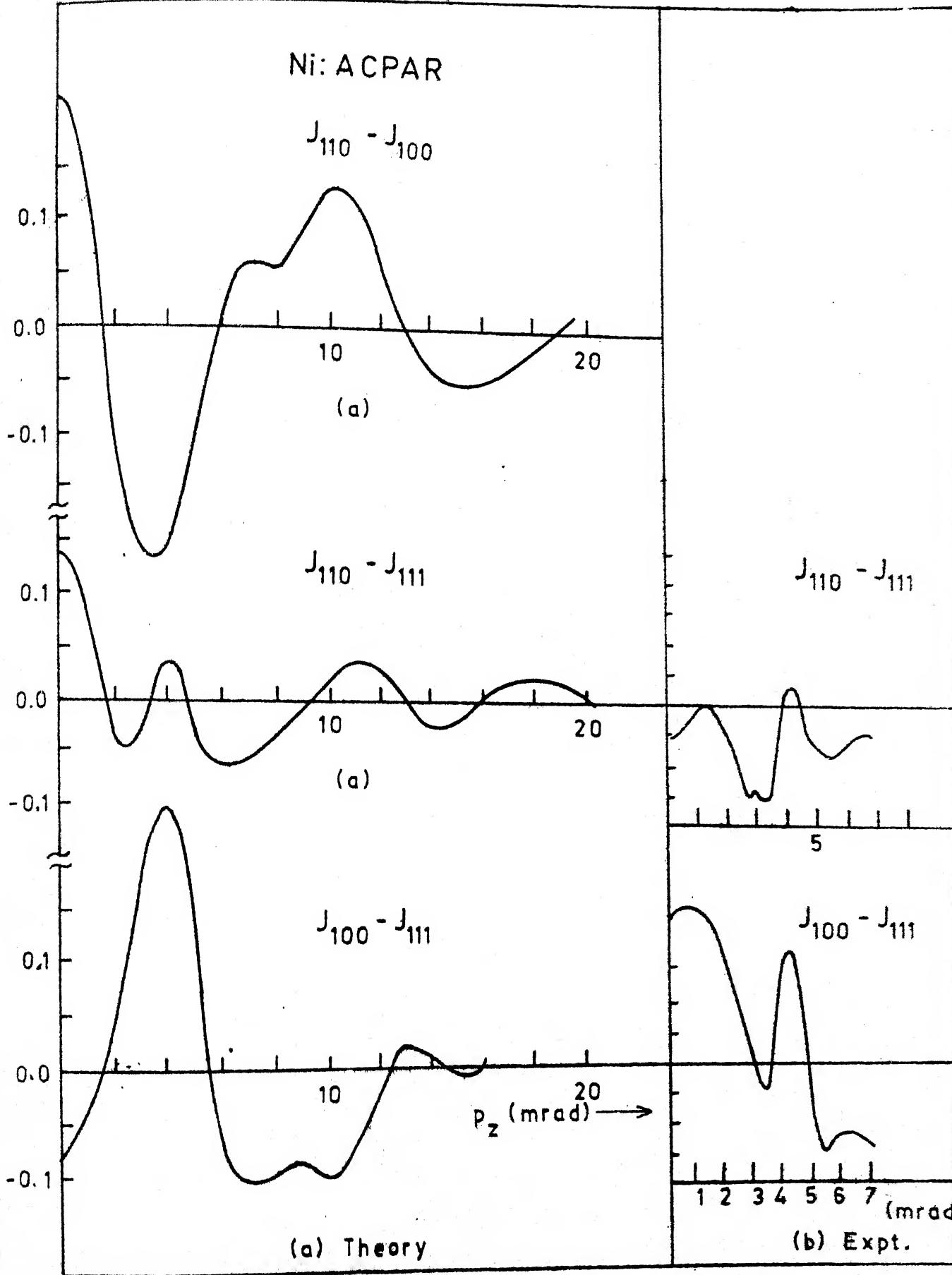


Fig. 6.2: Theoretical and experimental ACPAR anisotropies for Ni. Note the difference in momentum scale.

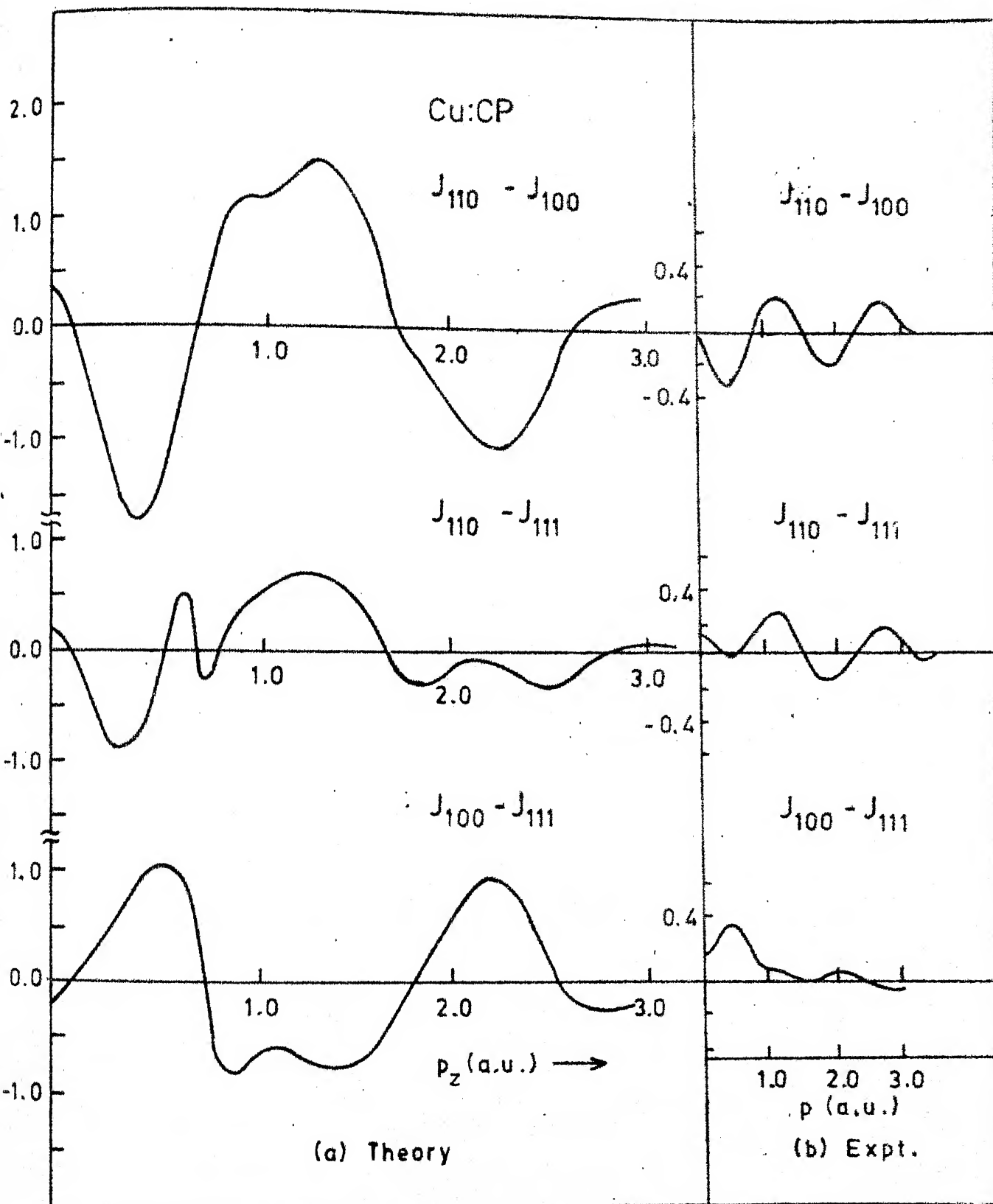


Fig. 6.3: Theoretical and experimental CP anisotropies for Cu. Note the difference in momentum scale.

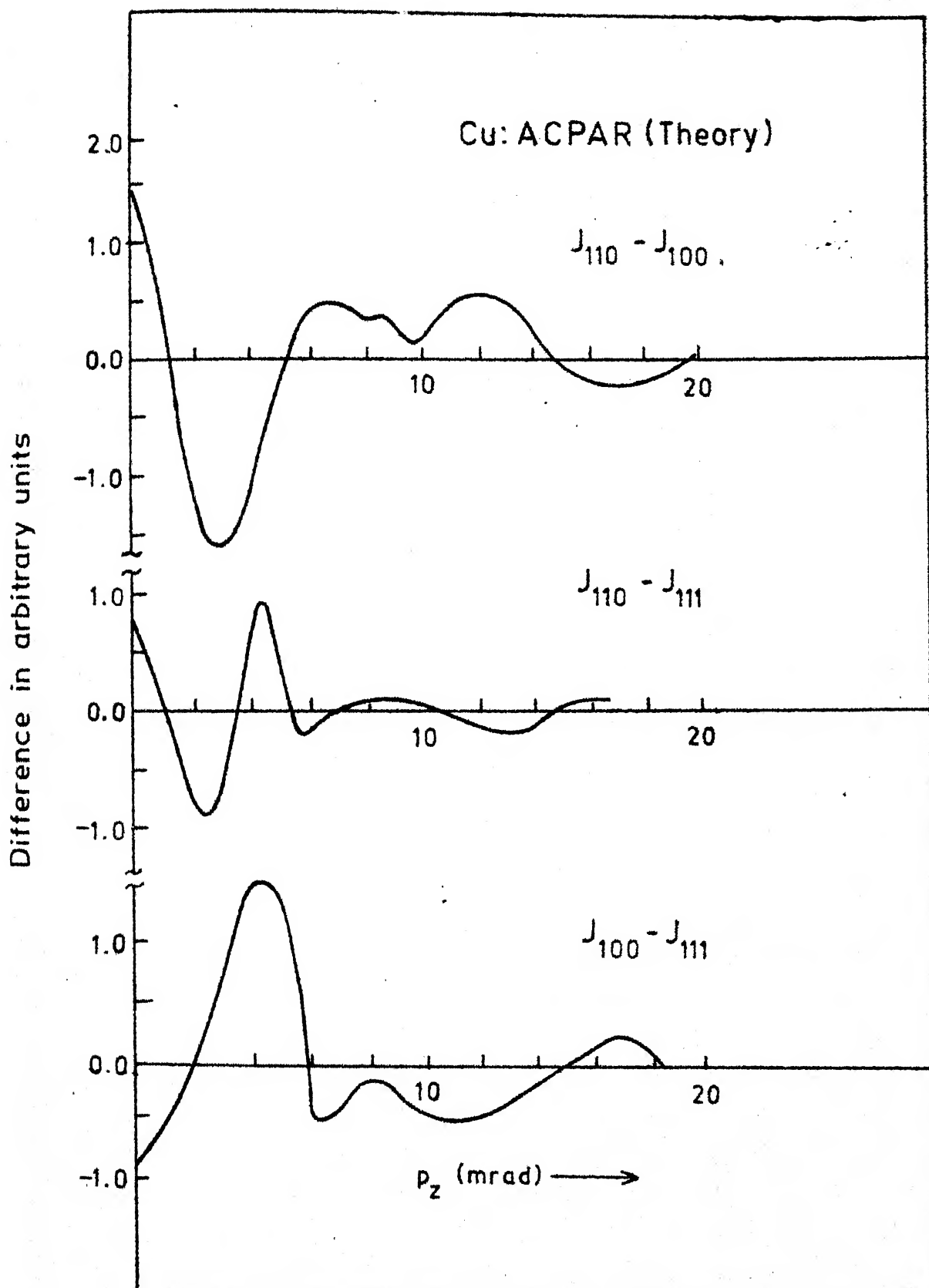


Fig. 6.4: Theoretical ACPAR anisotropies for Cu.

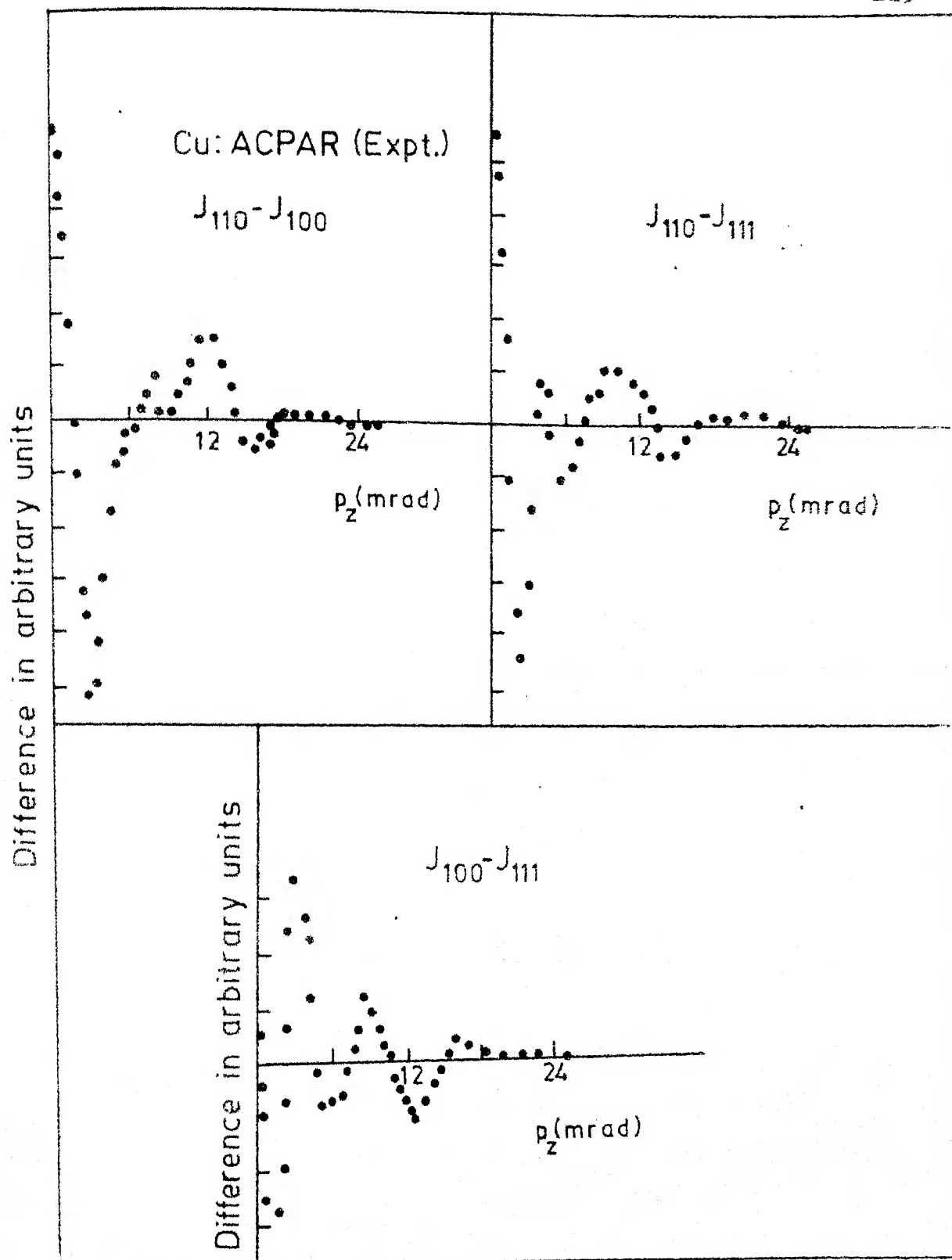


Fig. 6.5: Experimental ACPAR anisotropies for Cu.

c) The agreement for Cu (CP and ACPAR) is somewhat better than that for Ni.

d) Compared to the theoretical curves, experimental ACPAR curves show a structure at low momenta.

To understand some of these features we should note from Eqs. (6.3) and (6.4) that the behaviour of J_{hkl} particularly at low momenta, can be affected by the following two types of truncation errors.

i) Truncation errors in the harmonic expansion $\rho_{lv}(p)$:

Arbitrary truncation in Eq. (6.1) can lead to incorrect representation of $\rho(\vec{p})$ through $\rho_l(p)$. Again a choice of $n_1 = 3$, $n_2 = 3$ may allow us to fit the function $\rho_l(p)$ at specified momentum (p) values but it may not lead to correct $\rho_l(p)$ values at intermediate p -values. The step-function character in $\rho(\vec{p})$ due to Fermi surface can also lead to incorrect $\rho_l(p)$.

ii) Truncation errors in the integral for $g_{lv}(p_z)$:

The calculations for $\rho(\vec{p})$ were made only upto $P_{\max} = 3.5$ a.u. because of the limitations of the Hubbard-Mijnarends method and computational problems at high momentum values. This would introduce a truncation error in (6.4) because the upper limit of integration is brought down from infinity to P_{\max} .

The latter type of truncation error can be particularly more serious for CP which have significant high momentum components. On the other hand for ACPAR the former type of truncation error can cause more problems. We feel that the disagreement observed in Figs. 6.1 - 6.5 is due to the above truncation errors, although all the features may not be explained so easily. However the results for Ni and Cu have provided us with a valuable idea about the limitations of the above method.

Above analysis for Ni and Cu show that it is worthwhile to extend our above procedure to the theoretical $\rho(\vec{p})$ of Pd and Ag, if higher harmonics are included in Eq. (6.1). In the following section we present our results and discuss them.

6.4 Results for Pd and Ag and Discussion:

Our results for the CP anisotropy for Ag using the $\rho(\vec{p})$ results of Chapter 4 are shown in Figs. 6.6 and 6.7. We have tried to make systematic study of the truncation errors involving $\rho_{\ell}(p)$ by making calculations for different combinations of n_1 (number of directions of \vec{p} for which $\rho(\vec{p})$ is calculated) and n_2 (number of terms retained in harmonic expansion (6.1)). The values of n_1 and n_2 used in the analysis are marked on each figure. Similar plots of the CP anisotropy for Pd are shown in Figs. 6.8 and 6.9. It can be

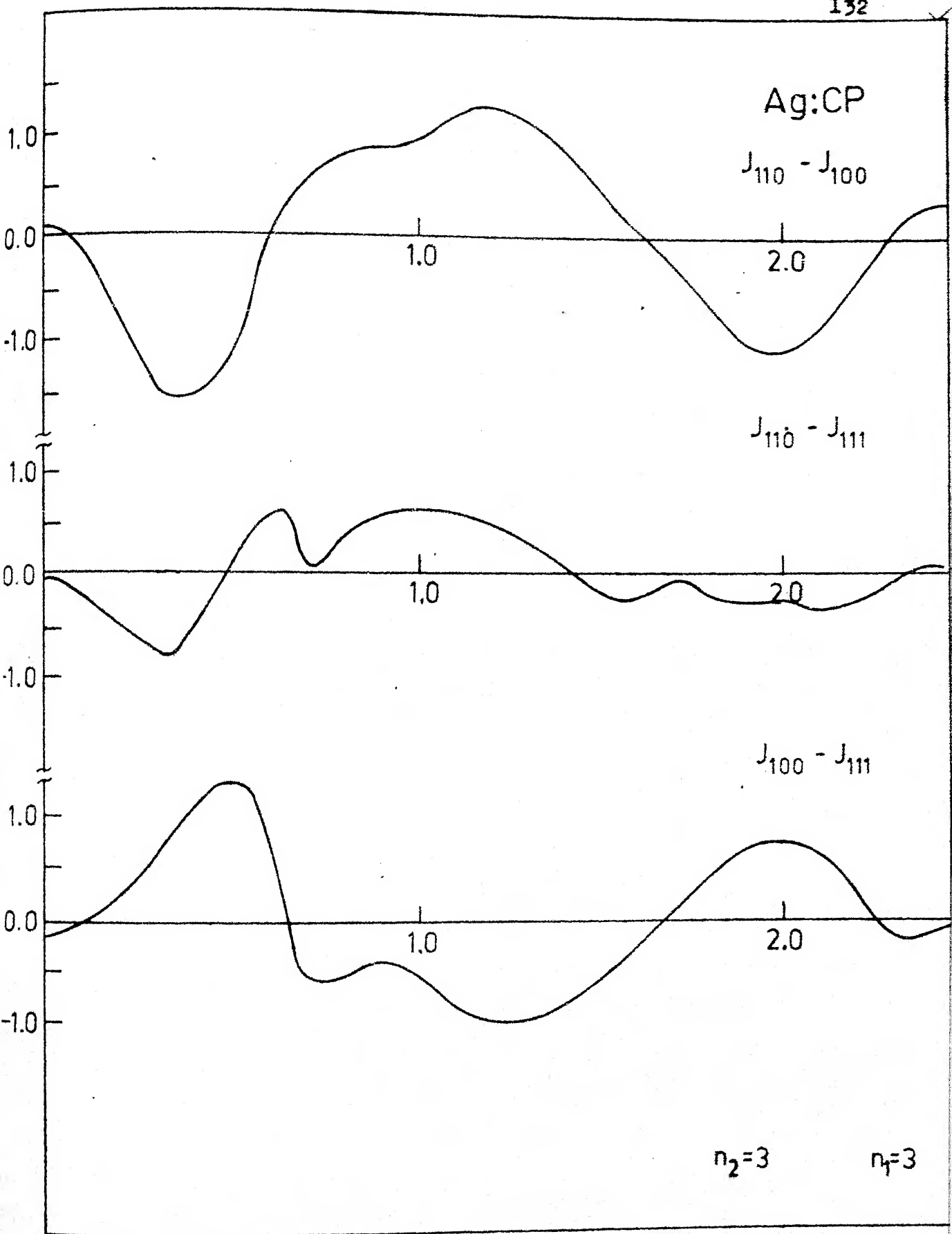


Fig. 6.6: Theoretical CP anisotropies for Ag.

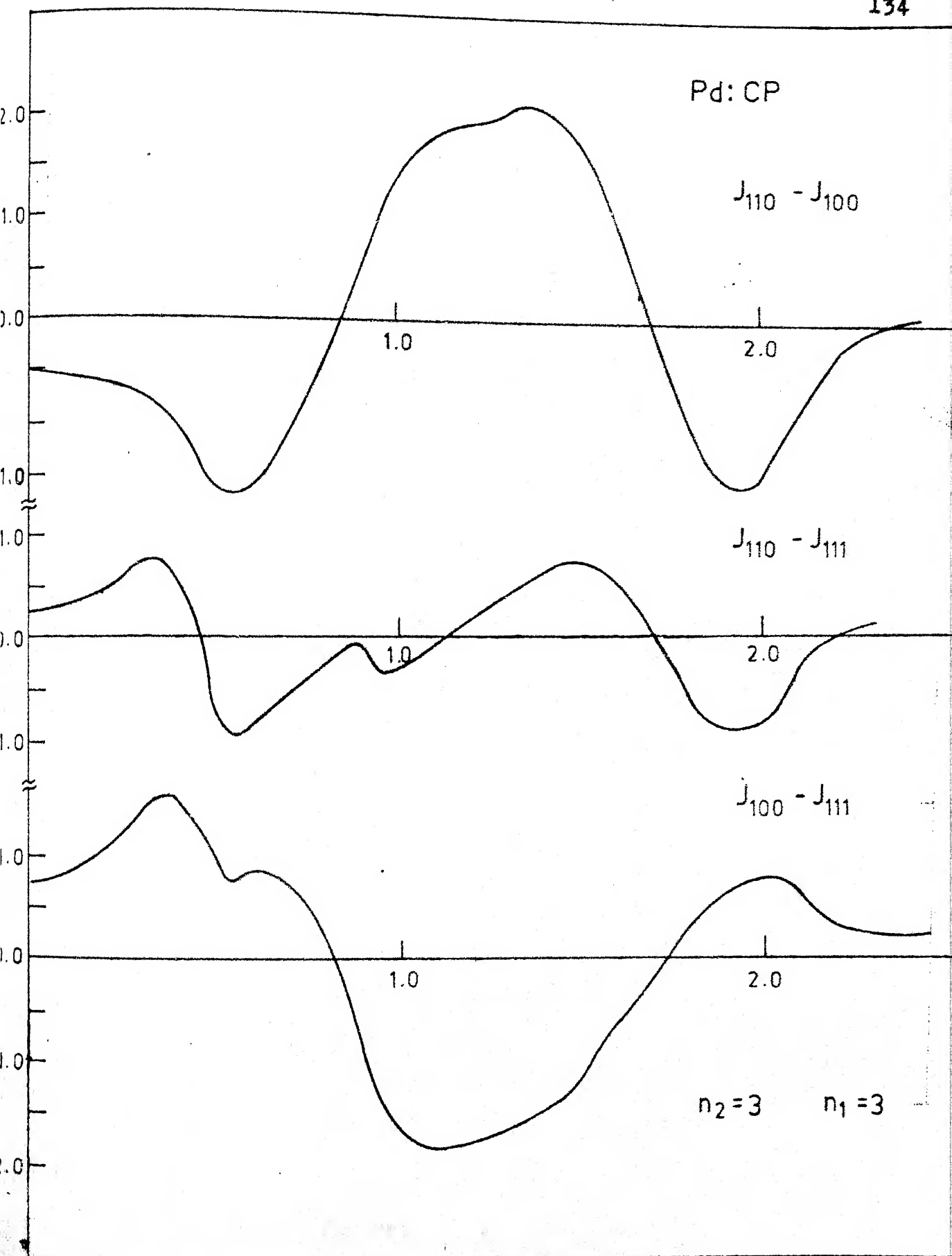


Fig. 6.8: Theoretical CP anisotropies for Pd.

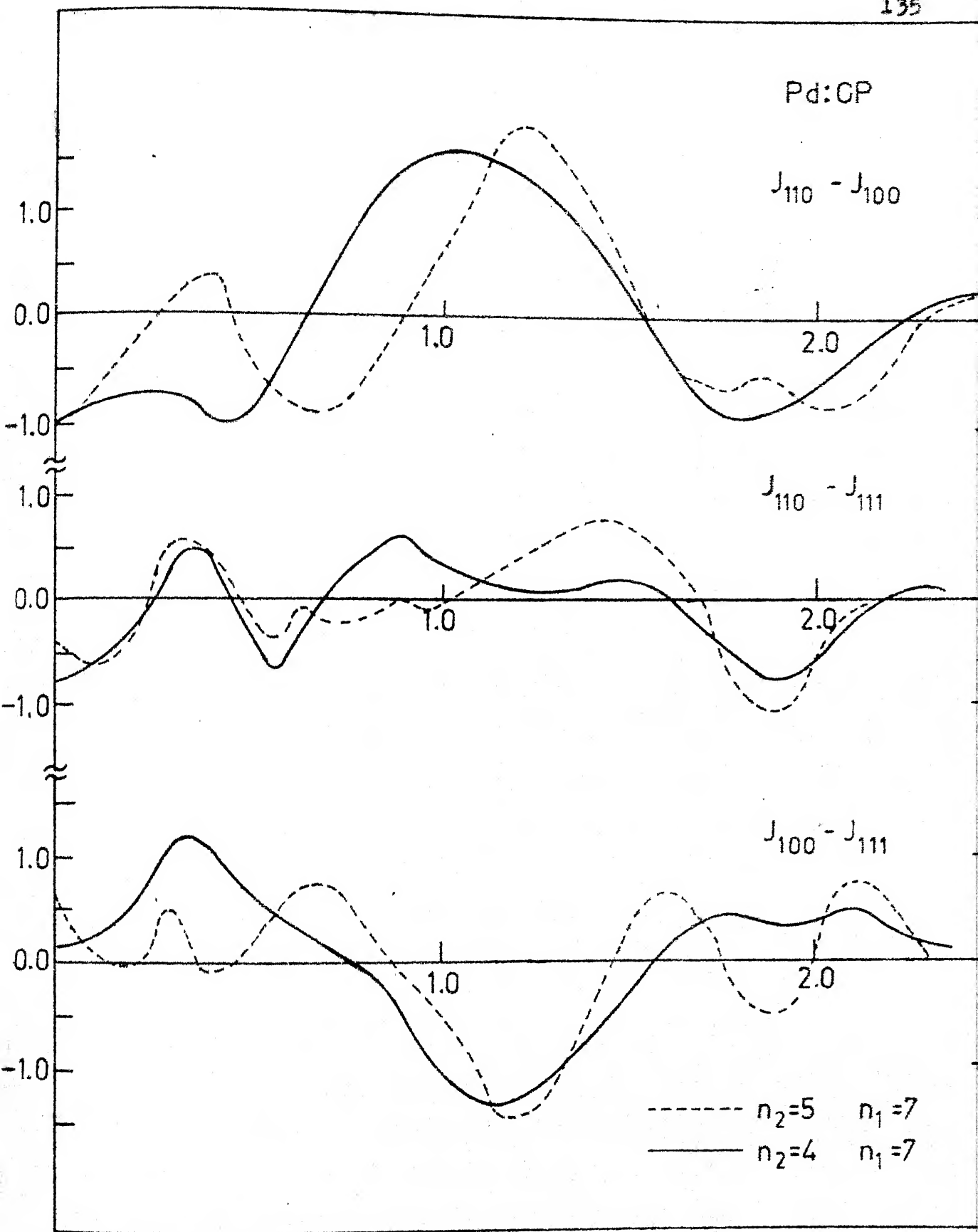


Fig. 6.9: Theoretical CP anisotropies for Pd.

observed that the anisotropies for Ag are very similar to those of Cu (cf. Fig. 6.3) as expected from the similarities in their EMD (Chapter 5). On the other hand, the anisotropies of Pd are not altogether similar to those of Ni, an observation already made about their EMD's in Chapter 5. Examination of Figs. 6.6 and 6.7 shows that for Ag anisotropy curves change as n_2 is changed from 3 to 6. The changes are most significant while going from $n_1 = 3, n_2 = 3$ to $n_1 = 12, n_2 = 5$. Changes in going from $n_2 = 5$ to $n_2 = 6$ (n_1 being 12) are minor indicating that inclusion of 6th term in the expansion has little effect on the anisotropy. Other observations can be summarised as follows.

a) The difference curves ($J_{110} - J_{100}$) change least as (n_1, n_2) changes from (3, 3) to (12, 6). It may be recalled that this difference curve showed the best agreement (among the curves discussed in Sec. 6.3) between theory and experiment for Ni and Cu.

b) The difference curve ($J_{110} - J_{111}$) seems to develop a well-defined minimum around $p = 2$ a.u. as (n_1, n_2) changes from (3, 3) to (12, 5) or (12, 6).

c) The difference curve ($J_{100} - J_{111}$) shows maximum changes as (n_1, n_2) is changed from (3, 3) to (12, 6). There seems to be a decrease in the intensity of the peaks and a development of oscillations. It may be pointed out that

for Ni and Cu, the difference curves ($J_{100} - J_{111}$) had shown least satisfactory agreement with the experiment.

d) The effect of including higher terms (n_2) in the expansion seems to broaden the peaks in the curves. Our calculations (not shown in Figs. 6.6 - 6.7) further indicate that the differences at low momentum region (around $p = 0$) fluctuate as n_2 goes from 7 to 11. In the absence of any experimental data to compare with our results, we feel that for $n_1 = 12$, a reasonable choice for n_2 is $n_2 = 5$ or 6.

A further discussion of our results for Ag would be made in terms of $\rho_{\mathbf{k}}$ and $g_{\mathbf{k}}$ functions later in this section.

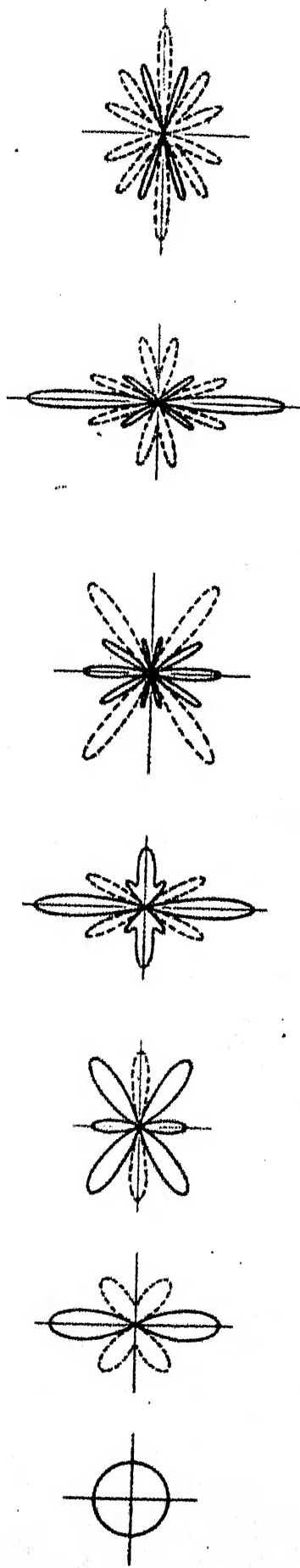
In the case of Pd we have calculated $\rho(\vec{p})$ along 7 ($n_1 = 7$) directions only. Our observations for Pd can be summarised as follows. A significant change in all the three difference curves is observed as (n_1, n_2) is changed from (7,4) to (7,5). Such a significant change was not observed by us for Ag. It is known that for a reliable least-square-fit as in the inversion of Eq. (6.1), we should have $n_2 \leq n_1/2$. This might explain the above behaviour. In any case the EMD in Pd is more sensitive to the truncation errors in the harmonic expansion (6.1). Other changes in Pd caused by (n_1, n_2) going from (3,3) to (7,4) are qualitatively similar to those observed in Ag.

A deeper insight into the above results can be obtained by studying the behaviour of the functions $\rho_l(p)$ and $g_l(p_z)$ in (6.1) and (6.3) respectively.

For this discussion it is helpful to know the angular dependence of the lattice (kubic) harmonics in the (110) and (100) planes as shown in Fig. 6.10. The ρ_l and g_l functions obtained by us for Pd and Ag are shown in Figs. 6.11 to 6.13, respectively. These functions reveal the following important features.

A) The ρ_l functions for Pd show more structure than those for Ag. Functions ρ_0 represent the spherically averaged part of the EMD, $\rho(\vec{p})$, while higher ρ_l are a measure of the anisotropic part of the EMD. In Chapter 4, it was already noted that the EMD in Pd is more anisotropic than that in Ag. This fact seems to be reflected in the behaviour of the respective ρ_l functions. The higher ($l \geq 4$) ρ_l terms in Ag show contributions around the Fermi momentum p_F and around $p_F + G$, but in Pd they have appreciable contributions at intermediate momentum values also. This indicates that the anisotropies in the EMD of Pd are built up not only from the Fermi surface anisotropy but also from a strong k -dependence of the d-electron momentum distribution. The curves also indicate that the EMD in Pd is more complicated than the EMD in Ag. Other features displayed in Figs. 6.11 to 6.13 can be understood from the results of the EMD of Pd and Ag taken together with Fig. 6.10.

(110) plane



(001) plane

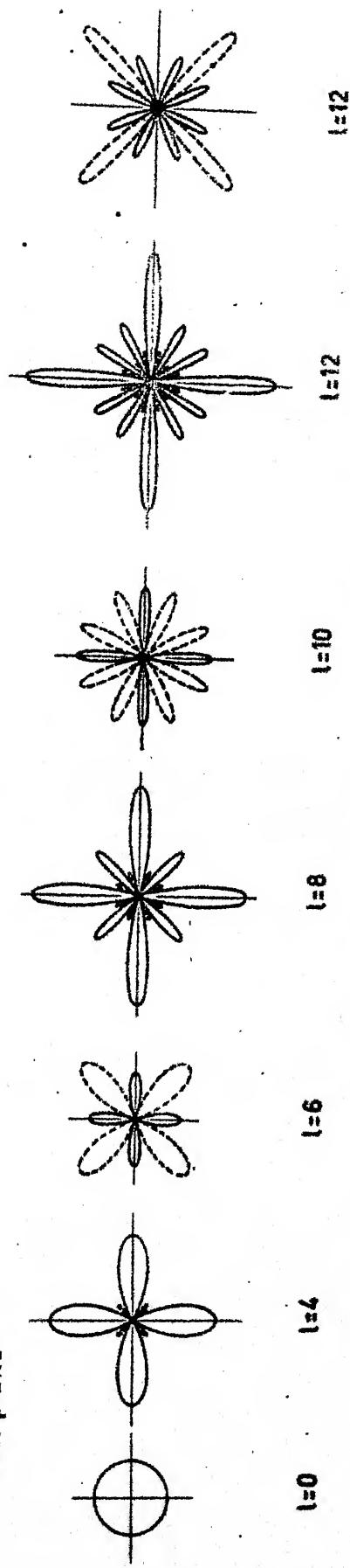


Fig. 6.10 Angular dependence of first seven cubic harmonics .

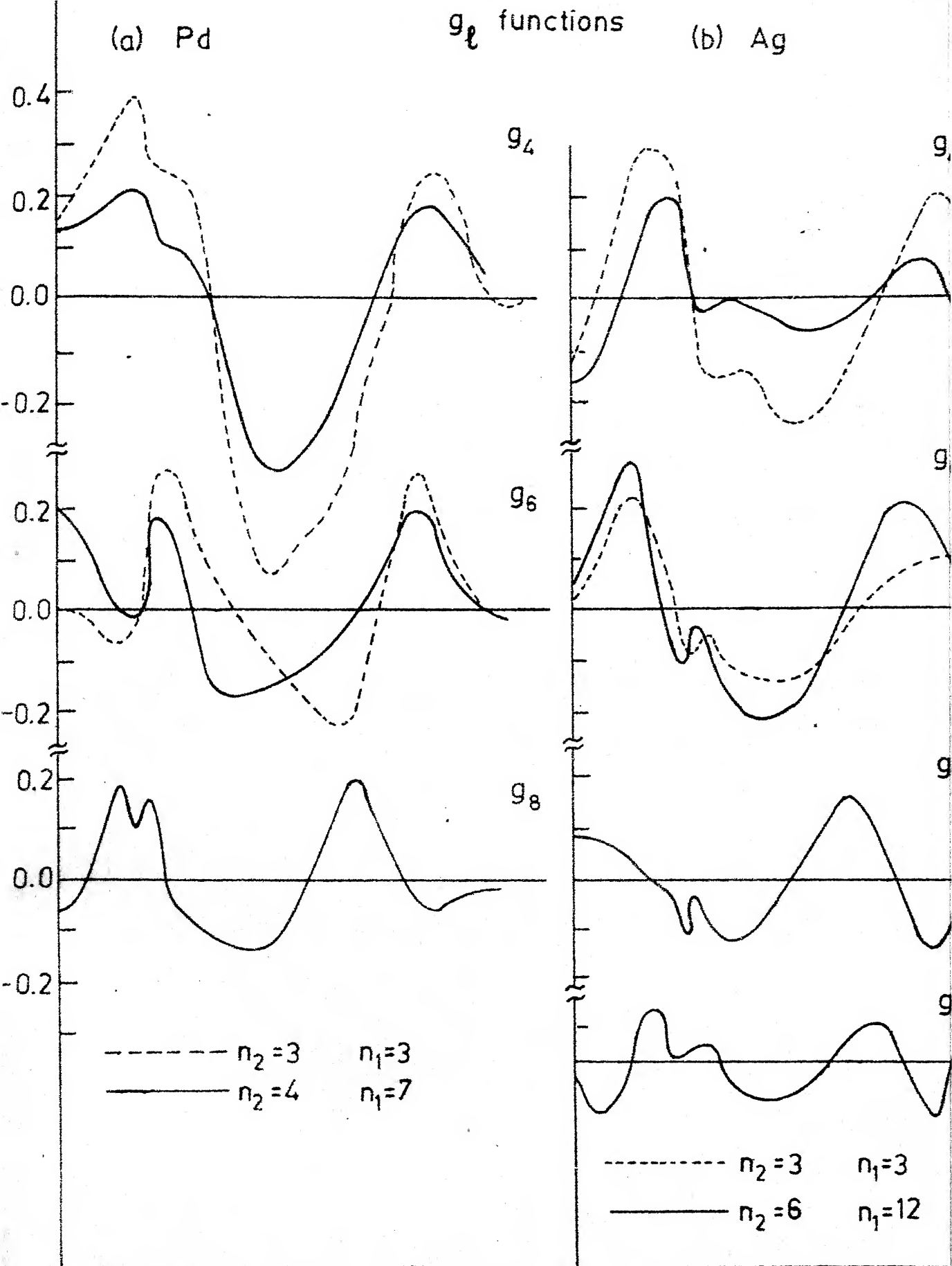


Fig. 6.12: g_l functions for Pd and Ag.

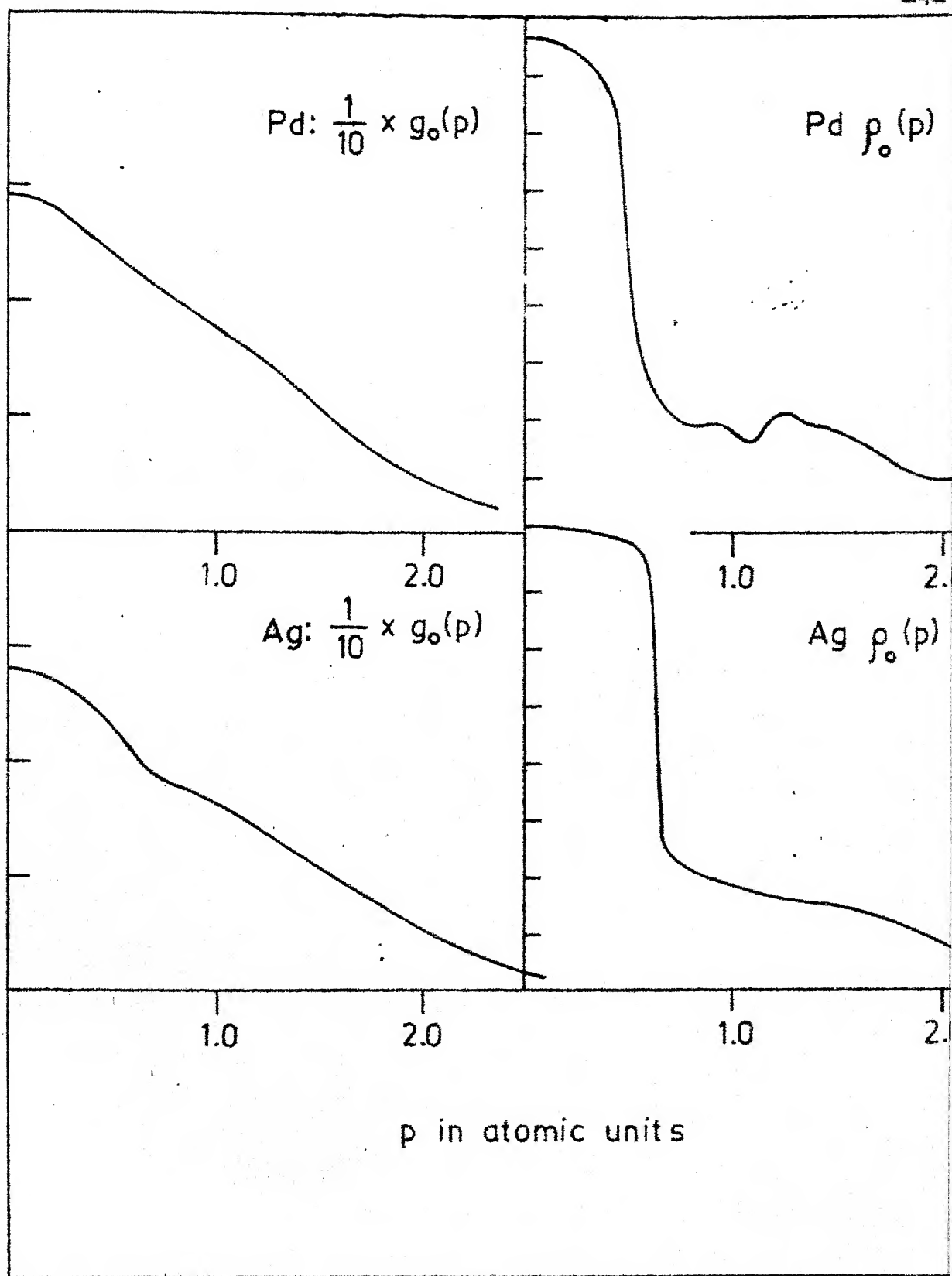
$g_o(p)$ in arbitrary units


Fig. 6.13

- a) Spherically averaged Compton profile, $g_o(p)$, for Pd and Ag. b) Spherically averaged EMD profile, $\rho_o(p)$, for Pd and Ag.

B) For Pd, ρ_8 shows an appreciable contribution underlining the need to consider higher harmonics ($l \geq 8$).

C) The function g_0 represents the spherically averaged part of the CP while higher ($l \geq 4$) g_l functions give the anisotropic part of the CP. The plots of $g_l(p_z)$ in Fig. 6.12 display a rather slow convergence.

To summarise, the analysis made in this Chapter has shown the following.

i) Starting from a theoretical EMD and employing the lattice harmonic expansion method outlined above, a fair idea about the anisotropies of the directional profiles can be obtained. This information can provide a preliminary guideline for experimentalists in selecting the particular single crystal directions (h,k,l) which could be most interesting. Of course the best way to compare theory with experiment is to carry out a two-dimensional integration of $\rho(\vec{p})$ in momentum space. However the lattice harmonic expansion method can offer a faster but approximate way to obtain a rough idea of the anisotropies expected or to compare theory with experiment.

ii). We feel that the main utility of the present method is that an examination of the ρ_l and g_l plots can be instructive for carrying out an 'unfolding' [1] of measured CP (or ACFAR) data for reconstruction of $\rho(\vec{p})$. Thus our

graphs (Figs. 6.11 to 6.13) suggest that for Ag and Pd one should measure CP along enough number of directions so that at least 6 terms (upto $l_{\max} = 12$) can be used in the harmonic expansion.

A better understanding of the usefulness and applications of the present method can be obtained once experimental CP data for Pd and Ag becomes available. We feel that a folding and unfolding analysis by the lattice harmonics expansion method on same single crystal metals should be carried out to gain a better insight into the method. It may be worthwhile to attempt a similar analysis employing the Fourier method [10] as well.

Our analysis has also brought out the limitations of the lattice harmonic expansion method. Firstly, the discontinuities in the $\rho(\vec{p})$ cannot be handled satisfactorily by this method. Secondly the choice of (n_1, n_2) to be used is not unique unless n_1 is quite large as compared to n_2 (e.g. $n_1 \approx 40, n_2 \approx 10$), thus necessitating large computational efforts. Thirdly the convergence of $g_{\vec{g}}$ function is slow and a certain amount of arbitrariness always remains about the truncation in (6.1).

REFERENCES

1. P.E. Mijnaarends, Phys. Rev. 160, 512 (1967). Also see P.E. Mijnaarends, 'Reconstruction of Three-Dimensional Distributions' in the book 'The Compton Effect', edited by B.G. Williams, to be published by McGraw-Hill.
2. P.E. Mijnaarends, Physica 63, 248 (1973).
3. H. Stachowiak, Phys. Status Solidi 41, 599 (1970).
4. P.E. Mijnaarends, Phys. Rev. B4, 2820 (1971).
5. W. Schulke, Phys. Status Solidi B 62, 453 (1974).
6. P.E. Mijnaarends and R.M. Singru, Appl. Phys. 4, 303 (1974).
7. G. Kontrym-Sznajd and H. Stachowiak, Appl. Phys. 5, 361 (1975).
8. H. Rozenfeld and S. Chabik, Abstract A-5, Third International Conference on Positron Annihilation, Helsinki, Finland (1973), Unpublished.
9. G. Kontrym-Sznajd, H. Stachowiak, W. Wierzchowski, K. Peterson, N. Thrane and G. Trumpy, Appl. Phys. 8, 151 (1975).
10. F.M. Mueller, Bull. Am. Phys. Soc. II 19, 200 (1974).
11. C.K. Majumdar, Phys. Rev. B4, 2111 (1971).
12. S. Wakoh and J. Yamashita, J. Phys. Soc. Jap. 35, 1406 (1973).
13. S. Wakoh, Y. Kubo and J. Yamashita, J. Phys. Soc. Jap. (To be published).
14. J. Rath, C.S. Wang, R.A. Tawil and J. Callaway, Phys. Rev. B8, 5139 (1973).
15. S. Wakoh, T. Fukamachi, S. Hosoya and J. Yamashita, J. Phys. Soc. Jap. (To be published).
16. F.C. Von der Lage and H.A. Bethe, Phys. Rev. 71, 612 (1947).

17. M.E. Rose, Elementary Theory of Angular Momentum, (John Wiley and Sons. Inc. New York, 1957), p. 50.
18. After we had started these calculations the following works employing similar method came to our notice. H. Bross and H. Stohr, Appl. Phys. 3, 307 (1974), and A. Seth and D.E. Ellis, Momentum Density and Compton Profile of TiCl_4 (To be published).
19. R.M. Singru and P.E. Mijnenreids, Phys. Rev. B9, 2372 (1974).
20. R.M. Singru, Pramana 2, 299 (1974).
21. P. Eisenberger and W.A. Reed, Phys. Rev. B9, 3242 (1974).
22. S. Cushner, J.C. Erskine and S. Berko, Phys. Rev. B1, 2852 (1970).

VITAE

The author was born in Poona on January 6, 1950. He graduated in 1969 and obtained his M.Sc. degree in Physics from Poona University in 1971. Thereafter he joined Department of Physics, Indian Institute of Technology Kanpur, Kanpur, as a research scholar. At present he is a research assistant in the Department of Physics, IIT Kanpur.

Publications:

- 1) Electron Momentum Distribution in Palladium, D.G. Kanhere and R.M. Singru, Phys. Letts., 53A, 67 (1974)
- 2) Electron Momentum Distribution in Nickel and Copper employing a Renormalized free atom model, D.G. Kanhere and R.M. Singru, J. Phys. F: Metal Phys., 5, 1146 (1975)
- 3) Pseudopotential Band Calculation of the Electron Momentum Distribution in Aluminium, V.V. Bhokare, D.G. Kanhere, R.M. Singru, Xth International Congress of Crystallography, Amsterdam, August 1975.
- 4) Electron Momentum Distribution in Ag and Pd, Presented at Nuclear Physics and Solid State Physics Symposium (DAE), Calcutta, December, 1975.

Under Preparation:

- 1) A Band Structure Calculation of Momentum Distribution in Palladium and Silver, D.G. Kanhere and R.M. Singru.
- 2) Anisotropies of Compton Profile in Palladium and Silver, D.G. Kanhere and R.M. Singru.
- 3) Electron Momentum Distribution in Transition Metals: A Systematic Study in 3d and 4d (fcc/bcc) metals, D.G. Kanhere and R.M. Singru.